SAND2012-6121C

PROGRESS-VARIABLE APPROACH FOR LARGE-EDDY SIMULATION OF TURBULENT COMBUSTION

A DISSERTATION

SUBMITTED TO THE DEPARTMENT OF MECHANICAL ENGINEERING

AND THE COMMITTEE ON GRADUATE STUDIES

OF STANFORD UNIVERSITY

IN PARTIAL FULFILLMENT OF THE REQUIREMENTS

FOR THE DEGREE OF

DOCTOR OF PHILOSOPHY

Charles David Pierce

June 2001

I certify that I have read this dissertation and that in my opinion it is fully adequate, in scope and in quality, as a dissertation for the degree of Doctor of Philosophy.

Parviz Moin (Principal Advisor)

I certify that I have read this dissertation and that in my opinion it is fully adequate, in scope and in quality, as a dissertation for the degree of Doctor of Philosophy.

Craig T. Bowman

I certify that I have read this dissertation and that in my opinion it is fully adequate, in scope and in quality, as a dissertation for the degree of Doctor of Philosophy.

Godfrey Mungal

Approved for the University Committee on Graduate Studies:

ABSTRACT

A new approach to chemistry modeling for large eddy simulation of turbulent reacting flows is developed. Instead of solving transport equations for all of the numerous species in a typical chemical mechanism and modeling the unclosed chemical source terms, the present study adopts an indirect mapping approach, whereby all of the detailed chemical processes are mapped to a reduced system of tracking scalars. Presently, only two such scalars are considered: a mixture fraction variable, which tracks the mixing of fuel and oxidizer, and a progress variable, which tracks the global extent-of-reaction of the local mixture. The mapping functions, which describe all of the detailed chemical processes with respect to the tracking variables, are determined by solving quasi-steady diffusion-reaction equations with complex chemical kinetics and multicomponent mass diffusion. The performance of the new model is compared to fast chemistry and steady flamelet models for predicting velocity, species concentration, and temperature fields in a methane-fueled coaxial jet combustor for which experimental data are available. The progress-variable approach is able to capture the unsteady, lifted flame dynamics observed in the experiment, and to obtain good agreement with the experimental data and significantly outperform the fast chemistry and steady flamelet models, which both predict an attached flame.

ACKNOWLEDGEMENTS

Financial support for this work was provided by the Air Force Office of Scientific Research under grant F49620-95-1-0185 and by the Franklin P. and Caroline M. Johnson Fellowship. Computer resources were provided by NASA-Ames Research Center through the Center for Turbulence Research and by the Department of Energy's ASCI program.

This work has benefited greatly from discussions with many graduate students, postdoctoral fellows, professors, and visitors at the Center for Turbulence Research, among them, Knut Akselvoll, Blair Perot, Tom Bewley, Artur Kravchenko, Robert Jacobs, Jason Rife, Cliff Wall, Tom Lund, Hans Kaltenbach, Ken Jansen, Massimiliano Fatica, Kendal Bushe, Franck Nicoud, Joe Oefelein, Heinz Pitsch, Bill Reynolds, Tom Bowman, Amable Liñán, Javier Jiménez, Luc Vervisch, Thierry Poinsot, Fokian Egolfopoulos, Bob Bilger, George Kosály, and Norbert Peters.

I would especially like to thank my advisor, Professor Parviz Moin, for indoctrinating me into the ways of science, turbulence, and computer simulations, for his steadfast support, limitless patience, and encouragement that he has given to me and his other students, and for his commitment to excellence in research. I would also like to thank my reading committee members, Professors Tom Bowman and Godfrey Mungal, for their helpful comments on a draft of this dissertation.

TABLE OF CONTENTS

LIST OF FIGURES

NOMENCLATURE

Roman Symbols

A_i	atomic mass of element i
c	convection velocity; dimensionless coefficient
c_p	mixture specific heat at constant pressure (per unit mass)
$c_{p,i}$	specific heat at constant pressure of species i (per unit mass)
C	model coefficient; generic progress variable
D_{ij}	binary mass diffusion coefficient matrix
$D_{T,i}$	thermal mass diffusion coefficient of species i
$\frac{D}{Dt}$	material derivative operator, $\frac{D}{Dt} = \frac{\partial}{\partial t} + \boldsymbol{u} \cdot \nabla$
e	2.71828... ; mixture internal energy per unit mass
e_i	internal energy of species i (per unit mass)
$f(\ldots)$	generic function
$\boldsymbol{f}_i$	body force per unit mass of species i
g	mass flux, $g = \rho u$
h	mixture enthaply per unit mass
h_i	enthaply of species i (per unit mass)
$\mathbf{I}$	indentity tensor, $I_{ij} = \delta_{ij}$
k	kinetic energy per unit mass, $k = \frac{1}{2}u^2$; wavenumber
L	flamelet domain length
M_i	molecular mass of species i
n	boundary-normal coordinate
N_E	number of chemical elements
N_S	number of chemical species
N_{ij}	number of j atoms in a molecule of species i
p	pressure
p_0	background pressure
$P(\ldots)$	probability density function

$\boldsymbol{q}$	heat flux vector
$\boldsymbol{q}_R$	radiative heat flux vector
q_D	Dufour heat flux
q_{ij}	residual scalar flux of species i
r	radial coordinate
$\hat{R}$	universal gas constant
R	normalizing length scale
s	mixture entropy per unit mass
$\mathbf{S}$	strain-rate tensor, $S_{ij} = \frac{1}{2}(u_{i,j} + u_{j,i})$
t	time
t_{ij}	residual stress tensor
T	temperature
u	velocity component or magnitude; generic variable
$\boldsymbol{u}$	velocity vector
U	normalizing velocity scale
$\boldsymbol{V}_i$	mass diffusion velocity of species i
w_i	chemical production rate of species i
x	spatial coordinate; generic variable
x_i	mole fraction of species i
y_i	mass fraction of species i
y_{P}	product mass fraction
Z	mixture fraction

Greek Symbols

α	generic diffusivity
α_m	molecular diffusivity
α_t	turbulent diffusivity
α_i	mass diffusivity of species i
α_T	thermal diffusivity
α_Z	mixture-fraction diffusivity

Γ	Gamma function, $\Gamma(n) = (n-1)!$
δ	Dirac delta function
δ_{ij}	Kronecker delta
$\delta_x(\cdot)$	finite-difference operator
Δ	filter width; grid spacing
η	generic conserved quantity
θ	azimuthal coordinate
Θ	velocity divergence
κ	thermal conductivity, $\kappa = \rho c_p \, \alpha_T$
λ	generic eigenvalue
μ	molecular viscosity, $\mu = \rho\nu$; distribution mean
μ_t	turbulent viscosity
μ_B	bulk viscosity
ν	kinematic viscosity
π	$3.14159\ldots$
ρ	mass density
ρ_0	flamelet reference mass density
σ^2	distribution variance
$\boldsymbol{\tau}$	viscous stress tensor
ϕ	generic scalar variable
χ	scalar dissipation rate
χ_0	flamelet average dissipation rate
ψ	flamelet mixture-fraction flux
ω	angular frequency

Other Symbols

$\phi_{,x}$	indicates differentiation of ϕ with respect to coordinate x
∇	gradient operator
$\cdot$	contraction (inner product) operator
:	double-contraction operator

Chapter 1

INTRODUCTION

1.1 Motivation and Objective

Large eddy simulation (LES) stands in the middle of the range of turbulent flow prediction tools, between direct numerical simulation (DNS), in which all scales of turbulence are numerically resolved, and Reynolds-averaged Navier-Stokes (RANS) calculations, in which all scales of turbulence are modeled. In LES, the large, energy-containing scales of motion are simulated numerically, while the small, unresolved subgrid scales and their interactions with the large scales are modeled. The large scales, which usually control the behavior and statistical properties of a turbulent flow, tend to be geometry and flow dependent, whereas the small scales tend to be more universal and consequently easier to model.

However, this fundamental advantage of LES has been called into question for reacting flows. It has been argued that since chemical reactions take place only after the reactants become mixed at the molecular level (so that reactions occur mostly in the subgrid scales), turbulent reacting flows cannot, in general, be universal at the smallest scales and therefore, subgrid models for chemical reactions cannot be any simpler than in Reynolds-averaged approaches.

The counterargument is that the presence of chemical reactions does not invalidate the hypothesis of universality of the small scales. Indeed, flamelet models of turbulent combustion presuppose that there exist universal flame structures at the smallest scales. One could also argue that it is because of the inaccurate modeling of the large scales, in particular large-scale mixing, that Reynolds-averaged approaches sometimes fail to predict turbulent reacting flows accurately, so that even with a fairly simple model for the chemistry, LES may be able to outperform Reynolds-averaged computations that employ more sophisticated chemistry models.

To put LES into perspective, it will be helpful to compare its costs and benefits to the alternative methods of DNS, RANS, and physical experiments. DNS is the method of choice for low Reynolds number flows in which the range of scales to be resolved is small, but it is not feasible for high Reynolds number flows of practical importance. RANS is used when computational cost (or turnaround time), rather than solution accuracy, is the deciding factor. In many ways, LES represents a logical compromise by providing accurate, high fidelity solutions at affordable cost. In general, the cost of an LES of a high Reynolds number flow is comparable to DNS of a similar low Reynolds flow. However, when LES and DNS are compared at the same Reynolds number, the cost difference is enormous. In this case, LES can provide nearly the same information and accuracy as DNS for quantities of engineering interest but at a fraction of the cost. When compared with RANS, LES is seen to provide much more accurate data and, perhaps equally important, more complete data, such as frequency spectra and pressure fluctuations, but at a cost that can be several orders of magnitude higher than RANS. However, relative to the remaining alternative of physical testing, the cost of LES appears quite reasonable, and as the cost of computing declines in the coming years, LES is expected to compete not only with RANS but also with laboratory experiments in providing accurate design data with fast turnaround time and low cost. This is especially true in applications of LES to gas turbine combustors and internal combustion engines, where the Reynolds numbers are low and flows are unsteady and separated. These conditions are suitable for economical LES, and they have posed difficulty for RANS computations.

The objective of this work is the development of a large eddy simulation based prediction methodology for turbulent reacting flows with principal application to gas turbine combustors. It is in the gas turbine industry where accurate, high fidelity prediction methods for turbulent combustion are desperately needed for the design of next generation, low emissions combustors. Current practice in the industry relies heavily on RANS calculations, backed up by expensive physical testing. The trend in the industry and in engineering in general, is towards shorter design

cycles through increased reliance on numerical prediction. RANS models for turbulent combustion do not appear capable of meeting the needs of industry in this regard, and the industry is beginning to look towards more sophisticated prediction tools that can take advantage of new computational capabilities. It is, in fact, the relentless advance of computer technology that is the driving force behind increasing expectations for computational fluid dynamics and the main motivation for this study.

1.2 Literature Survey

Large eddy simulation has been developed and studied as a turbulent flow prediction tool for engineering during the past three decades, with significant progress occurring more recently with advances in computer technology and the development of the dynamic subgrid-scale modeling procedure (Germano *et al.* 1991). With the dynamic procedure, model coefficients are automatically computed using information contained in the resolved turbulence scales, thereby eliminating the uncertainties associated with tunable model parameters. Moin *et al.* (1991) applied the dynamic procedure to scalar transport and subgrid kinetic energy models for compressible turbulent flows using Favre filtering. Reviews of LES are given by Lesieur and Métais (1996) and Moin (1997). The application of large eddy simulation to chemically reacting flows has been a subject of growing interest, but to date few simulations of realistic combustion systems have been undertaken.

The application of LES to gas turbine combustor configurations has been facilitated by the availability of comprehensive experimental data for both nonswirling and swirling confined coaxial jets with and without chemical reactions, due to the classic experiments that were conducted at United Technologies Research Center (Johnson and Bennett 1981, 1984; Roback and Johnson 1983; Owen *et al.* 1976; Spadaccini *et al.* 1976). Akselvoll and Moin (1996) simulated incompressible flow with a passive scalar in a nonswirling confined coaxial jet and obtained good agreement with the experiment of Johnson and Bennett (1984). Pierce and Moin (1998a) further extended that work to include the effects of swirl, which is commonly used

in gas-turbine combustors, and chemical heat release, which requires the use of variable-density transport equations. These studies were successful in predicting velocity and conserved scalar mixing fields in complex combustor flows, but they did not consider the effects of finite-rate chemistry or the general issue of chemistry modeling in LES.

Techniques for computational modeling of turbulent combustion have been the subject of numerous studies, with significant advances attributable to the development of flamelet models (Peters 1984, 1986), PDF methods (Pope 1985, 1990), conditional moment closure (Klimenko and Bilger 1999), and linear eddy modeling (Kerstein 1992a, 1992b; McMurtry *et al.* 1993; Calhoon and Menon 1996). A comprehensive review of turbulent combustion modeling has been written by Peters (2000). Many of these established modeling approaches have recently been extended for use in large eddy simulations.

The steady flamelet model was proposed for LES and tested in homogeneous turbulence by Cook *et al.* (1997). Unsteady flamelet modeling was used by Pitsch and Steiner (2000) in large eddy simulation of a piloted jet diffusion flame, where excellent agreement with the experimental data was obtained. Gao and O'Brien (1993), Réveillon and Vervisch (1998), among others, have proposed extensions of the PDF method to LES. In the latter study, the dynamic approach was used to close the turbulent micro-mixing term in the PDF transport equation. Monte Carlo simulation techniques, which are commonly used in the implementation of PDF methods, have been generalized to LES via the filtered density function (Colucci *et al.* 1998; Jaberi *et al.* 1999). A variant of the conditional moment closure technique, called conditional source estimation was proposed by Bushe and Steiner (1999), who also incorporated it into an LES of a piloted jet diffusion flame (Steiner and Bushe 2001). Jaberi and James (1998) propose modeling the filtered chemical source terms in LES using the scale-similarity approach and obtain the corresponding model coefficient using the dynamic procedure. However, scale similarity assumptions may be inappropriate for quantities that are dominated by small scales such as chemical reactions and scalar dissipation, and therefore, it is unlikely that extrapolation

from larger scales would yield accurate results in high Reynolds number applications. DesJardin and Frankel (1998) have performed extensive evaluation of several subgrid-scale combustion models. However, their conclusions may not be applicable to LES of high Reynolds number flows.

Assumed PDF methods offer a simple and inexpensive alternative to modeling approaches that solve PDF transport equations (Frankel *et al.* 1993). The most important application of assumed PDF's has been in the modeling of mixture fraction fluctuations. Cook and Riley (1994) proposed the assumed beta PDF as a subgrid-scale mixing model in LES and successfully tested it in homogeneous turbulence. Jiménez *et al.* (1997) tested the assumed beta PDF for LES in a turbulent mixing layer and demonstrated, in particular, the superior performance of the model in highly intermittent, forced mixing layers where the assumed PDF approach in the RANS context was found to be very inaccurate. Wall and Moin (2000) tested the model in the presence of chemical heat release and also demonstrated that good results can be obtained. Assumed PDF's require the variance of the subgrid scalar fluctuations as an input parameter. This quantity was modeled by Cook and Riley (1994) using a scale-similarity assumption. A theoretical estimate for the coefficient in this model was obtained by Cook (1997) and Jiménez *et al.* (1997). Pierce and Moin (1998c), using equilibrium assumptions for the subgrid scales, obtained an algebraic scaling law for the variance and computed its coefficient using the dynamic procedure.

One of the major challenges faced during the present study was to predict flame lift-off in non-premixed combustion. The flamelet/progress-variable approach (§3.3.4) was developed in part to address this problem, but it should be mentioned that an alternative solution may be to use the level-set or G-equation approach in combination with mixture fraction. This was used by Müller *et al.* (1994) in a RANS calculation of a lifted jet flame. Other approaches for modeling partially premixed combustion and lifted flames in LES have also been proposed (Vervisch and Trouvé 1998; Legier *et al.* 2000).

At present, most large eddy simulations of turbulent combustion in complex

geometries have not been subject to comprehensive validation against experimental data. Future developments in this field would benefit tremendously from new quantitative experimental data using modern non-intrusive diagnostic capabilities in complex configurations. The present study would not have been possible without the experimental data of Owen *et al.* (1976), which included detailed documentation of velocity, species concentrations, and temperature. A modern version of these experiments is currently underway at Stanford (Sipperley *et al.* 1999) to address the acute need for LES validation data.

1.3 Accomplishments

The following list summarizes the important contributions of this work:

- Development of a 20,000 line computer code, structured according to modern object-oriented progamming techniques, written in FORTRAN 90, and including distributed-memory parallelism using the MPI standard.

- Development of a body-force technique for generation of swirling inflow conditions (Pierce and Moin 1998b).

- Development of a dynamic subgrid-scale model for conserved scalar variance and dissipation rate (p. 23).

- Development of a novel flamelet/progress-variable chemistry model for LES of non-premixed combustion (p. 41).

- Development of a conservative space-time discretization for variable density flows (p. 54).

- Identification of spurious heat release as a mechanism for numerical instability in variable density flows (p. 58).

- Development of an iterative, semi-implicit time advancement scheme for the variable density equations (p. 59).

- Development of a novel technique for generating inflow turbulence from specified turbulence statistics (p. 72).

- First comprehensive validation of LES for complex reacting flows (p. 82).

- Demonstration of the importance of differential diffusion in flamelet modeling of subgrid-scale chemistry (p. 88).

Chapter 2

GOVERNING EQUATIONS

The starting point for a computational investigation is a statement of the governing equations for the phenomena under study. In this chapter, the complete, detailed governing equations for gaseous reacting flows are first presented and then simplified to a working set of equations suitable for the present study.

2.1 The Equations of Gaseous Combustion

The equations governing gaseous combustion are summarized below for reference (*e.g.* Williams 1985, p. 2). They are valid for a mixture of ideal gases in local thermodynamic equilibrium and chemical nonequilibrium.

Species:

$$\frac{\partial \rho y_i}{\partial t} + \nabla \cdot (\rho \boldsymbol{u} y_i) = -\nabla \cdot (\rho \boldsymbol{V}_i y_i) + \rho w_i \ , \quad i = 1, \ldots, N_S \tag{2.1}$$

Mass:

$$\frac{\partial \rho}{\partial t} + \nabla \cdot (\rho \boldsymbol{u}) = 0 \tag{2.2}$$

Momentum:

$$\frac{\partial \rho \boldsymbol{u}}{\partial t} + \nabla \cdot (\rho \boldsymbol{u}\boldsymbol{u}) = -\nabla p + \nabla \cdot \boldsymbol{\tau} + \rho \sum_i y_i \boldsymbol{f}_i \tag{2.3}$$

Energy:

$$\frac{\partial \rho (e+k)}{\partial t} + \nabla \cdot [\rho \boldsymbol{u}(e+k)] = -\nabla \cdot (p\boldsymbol{u}) + \nabla \cdot (\boldsymbol{\tau} \cdot \boldsymbol{u}) - \nabla \cdot \boldsymbol{q} + \rho \sum_i y_i \boldsymbol{f}_i \cdot (\boldsymbol{u} + \boldsymbol{V}_i) \tag{2.4}$$

Viscous Stress:

$$\boldsymbol{\tau} = 2\mu \left[\mathbf{S} - \tfrac{1}{3} (\nabla \cdot \boldsymbol{u}) \mathbf{I} \right] + \mu_B (\nabla \cdot \boldsymbol{u}) \mathbf{I} \tag{2.5}$$

Heat Flux:

$$\boldsymbol{q} = \underbrace{-\kappa \nabla T}_{\text{conduction}} + \underbrace{\sum_i \rho \boldsymbol{V}_i y_i h_i}_{\text{mass diffusion}} + \underbrace{\hat{R} T \sum_i \sum_j \frac{x_j D_{T,i}}{M_i D_{ij}} (\boldsymbol{V}_i - \boldsymbol{V}_j)}_{\text{Dufour effect}} + \underbrace{\boldsymbol{q}_R}_{\text{radiation}} \tag{2.6}$$

Mass Diffusion:

$$\begin{aligned}\nabla x_i = &\underbrace{\sum_j \frac{x_i x_j}{D_{ij}}(\boldsymbol{V}_j - \boldsymbol{V}_i)}_{\text{Stefan-Maxwell}} + \underbrace{(y_i - x_i)\frac{\nabla p}{p}}_{\text{pressure-gradient}} + \underbrace{\frac{\rho}{p}\sum_j y_i y_j(\boldsymbol{f}_i - \boldsymbol{f}_j)}_{\text{body-force}} \\ &\underbrace{+\sum_j \frac{x_i x_j}{\rho D_{ij}}\left(\frac{D_{T,j}}{y_j} - \frac{D_{T,i}}{y_i}\right)\frac{\nabla T}{T}}_{\text{Soret effect}}\end{aligned} \tag{2.7}$$

Thermodynamic State:

$$p = \rho \sum_i \frac{y_i}{M_i}\hat{R}T \tag{2.8}$$

Note that summation of all species conservation equations in (2.1) yields total mass conservation, (2.2), so that one of these $N_S + 1$ equations is redundant. To be consistent with mass conservation, the diffusion velocities and chemical sources must satisfy

$$\sum_i y_i \boldsymbol{V}_i = 0 \ , \qquad \sum_i w_i = 0 \ .$$

Equation (2.7) is an implicit vector equation for the species diffusion velocities. Temperature is implicitly related to internal energy or enthalpy through

$$e = \sum_i y_i e_i(T) \ , \qquad h = e + \frac{p}{\rho} = \sum_i y_i h_i(T) \ ,$$

where e_i and h_i are the species internal energies and enthalpies per unit mass, which for an ideal gas are functions of temperature only. Species mole and mass fractions are related by

$$x_i = \frac{y_i/M_i}{\sum_j (y_j/M_j)} \ , \qquad y_i = \frac{x_i M_i}{\sum_j x_j M_j} \ .$$

To complete the specification of the governing equations, molecular transport, thermochemical, and chemical kinetic property data are needed. Transport properties include μ, κ, D_{ij}, and $D_{T,i}$, while thermochemical data include h_i and M_i. Chemical kinetics will provide the chemical reaction sources, w_i, as functions of species concentrations, temperature, and pressure.

2.2 Simplifying Assumptions

For the large-scale simulations undertaken in this study, it is necessary to simplify the governing equations of §2.1, although when computations of flamelet solutions are considered in §3.3 it will be found that many of the simplifications are unnecessary. We adopt a standard set of assumptions that are well justified for many combustion systems and have been used in many previous studies. Accordingly, the following phenomena are neglected in this study:

- acoustic interactions and compressibility
- heating due to viscous dissipation
- bulk viscosity
- body forces
- diffusion due to pressure gradients
- thermal radiation

Furthermore, it will be convenient to express mass-diffusion processes in Fick's Law form by assigning a mixture diffusivity, α_i, to each species. The species diffusion velocities are then given by

$$\boldsymbol{V}_i = -\alpha_i \frac{\nabla y_i}{y_i} \ . \tag{2.9}$$

A simple formula for calculating approximate mixture diffusivities from the binary diffusivity matrix (Bird *et al.* 1960, p. 571) is,

$$\alpha_i = \frac{1 - x_i}{\sum\limits_{j \neq i} \frac{x_j}{D_{ij}}} \ . \tag{2.10}$$

A problem can arise when using (2.9) in that the resulting diffusion velocities do not necessarily satisfy $\sum_i y_i \boldsymbol{V}_i = 0$. A simple remedy is to subtract any residual "Stefan flow" from the bulk flow velocity in the species transport equations,

$$\nabla \cdot (\rho \boldsymbol{u} y_i) \ \longrightarrow \ \nabla \cdot [\rho(\boldsymbol{u} - \textstyle\sum_j y_j \boldsymbol{V}_j) y_i] \ ,$$

thereby cancelling any bulk flow arising from the diffusional mass fluxes.

The separate assumptions that acoustics and viscous heating are negligible are often lumped together into what is commonly called the "low Mach number approximation", though depending on the application, either of these phenomena could still be important even if the flow nominally has a very low Mach number. While these assumptions stipulate that the flow be low Mach number, the converse is not necessarily true.

In neglecting acoustic interactions and compressibility, it is assumed that thermodynamic variables such as density, temperature, enthalpy, and entropy are decoupled from variations in pressure, δp, about some specified background pressure field, p_0. This would mean, for example, that

$$\rho(p_0 + \delta p, s) \simeq \rho(p_0, s) \ , \quad \text{or} \quad \left(\frac{\partial \rho}{\partial p}\right)_s \simeq 0 \ ,$$

which, of course, implies that the speed of sound is nearly infinite. With this approximation, only p_0 is coupled to the thermodynamic variables and enters into the equation of state,

$$p_0 = \rho \sum_i \frac{y_i}{M_i} \hat{R} T \ . \tag{2.11}$$

For the open systems considered in this study it is also assumed that p_0 is uniform and constant so that the material derivative of pressure in the enthalpy equation reduces to

$$\frac{Dp}{Dt} \simeq \frac{Dp_0}{Dt} = 0 \ .$$

In addition to the above approximations, the "unity Lewis numbers" assumption (equal diffusivities for all species and temperature) is used for large-scale transport, where turbulent advection dominates. However, differential diffusion effects can still be important at the small scales, and in such cases, differential diffusion can be included in subgrid-scale models for turbulent combustion but can generally be ignored when solving the transport equations for the large scales.

The above assumptions are now used to derive simplified forms of the energy equation for reacting flows, starting with the internal energy equation (obtained by

subtracting kinetic energy from total energy) in enthalpy form:

$$\frac{\partial \rho h}{\partial t} + \nabla \cdot (\rho \boldsymbol{u} h) = \frac{Dp}{Dt} + \boldsymbol{\tau} : \nabla \boldsymbol{u} - \nabla \cdot \boldsymbol{q} + \rho \sum_i y_i \boldsymbol{f}_i \cdot \boldsymbol{V}_i \ . \tag{2.12}$$

After neglecting acoustic interactions, viscous dissipation, and body forces, this simplifies to:

$$\frac{\partial \rho h}{\partial t} + \nabla \cdot (\rho \boldsymbol{u} h) = \frac{Dp_0}{Dt} - \nabla \cdot \boldsymbol{q} \ . \tag{2.13}$$

Then, assuming constant p_0, rewriting the left-hand side in advective form, and substituting for the heat flux vector while neglecting radiation and the Dufour effect, one obtains:

$$\rho \frac{Dh}{Dt} = \nabla \cdot (\kappa \nabla T - \sum_i \rho \boldsymbol{V}_i y_i h_i) \ . \tag{2.14}$$

To generate more useful forms, the following identity is helpful:

$$\begin{aligned} \nabla h = \nabla \sum_i y_i h_i &= \sum_i y_i \nabla h_i + \sum_i h_i \nabla y_i \\ &= \sum_i y_i c_{p,i} \nabla T + \sum_i h_i \nabla y_i \\ &= c_p \nabla T + \sum_i h_i \nabla y_i \ . \end{aligned} \tag{2.15}$$

Using this relation and the species conservation equations, the left-hand-size of (2.14) may be expressed as:

$$\rho \frac{Dh}{Dt} = \rho c_p \frac{DT}{Dt} + \sum_i h_i \, \rho \frac{Dy_i}{Dt} = \rho c_p \frac{DT}{Dt} + \sum_i h_i \left[-\nabla \cdot (\rho \boldsymbol{V}_i y_i) + \rho w_i \right] \ .$$

Substituting this into (2.14) and rearranging yields:

$$\rho c_p \frac{DT}{Dt} = \nabla \cdot (\kappa \nabla T) - \sum_i \rho c_{p,i} \, y_i \boldsymbol{V}_i \cdot \nabla T - \sum_i \rho h_i w_i \ . \tag{2.16}$$

This is the standard form of the energy equation for reacting flows when temperature is used as a primitive variable. It should be noted that under assumption of equal specific heats for all species, the mass diffusion term in (2.16) is zero.

To avoid the reaction source term in (2.16), it is often desirable to work with total enthalpy. Returning to (2.14) and substituting Fick's Law for the diffusion velocities, we have,

$$\rho \frac{Dh}{Dt} = \nabla \cdot (\kappa \nabla T + \sum_i \rho \alpha_i h_i \nabla y_i) \ . \tag{2.17}$$

Using the identity (2.15) to eliminate ∇T, the following form can be derived:

$$\rho \frac{Dh}{Dt} = \nabla \cdot (\rho \alpha_T \nabla h) + \nabla \cdot [\sum_i \rho(\alpha_i - \alpha_T) h_i \nabla y_i] \ . \tag{2.18}$$

Under the assumption of unity Lewis numbers, $\alpha_i = \alpha_T$, this reduces to

$$\rho \frac{Dh}{Dt} = \nabla \cdot (\rho \alpha_T \nabla h) \ . \tag{2.19}$$

With this last step, the energy equation has been written as a simple advection-diffusion equation for a conserved scalar. If, in addition, adiabatic walls are assumed, then enthalpy and mixture fraction (§3.3.1) have the same boundary conditions and are linearly dependent.

2.3 Working Equation Set

With the assumptions and simplifications of §2.2, the governing equations used for this study may be written as follows:

Continuity:

$$\frac{\partial \rho}{\partial t} + \nabla \cdot (\rho \boldsymbol{u}) = 0 \tag{2.20}$$

Momentum:

$$\frac{\partial \rho \boldsymbol{u}}{\partial t} + \nabla \cdot (\rho \boldsymbol{u}\boldsymbol{u}) = -\nabla p + \nabla \cdot \left[2\mu (\mathbf{S} - \tfrac{1}{3}\mathbf{I}\, \nabla \cdot \boldsymbol{u}) \right] \tag{2.21}$$

Scalar Transport:

$$\frac{\partial \rho \phi_k}{\partial t} + \nabla \cdot (\rho \boldsymbol{u} \phi_k) = \nabla \cdot (\rho \alpha_k \nabla \phi_k) + \rho w_k \ , \quad k = 1, 2, \ldots \tag{2.22}$$

State Relation:

$$\rho = f(\phi_1, \, \phi_2, \, \ldots) \tag{2.23}$$

Note that the equation of state (2.23) has been reduced from (2.11) to an expression for density in terms of the transported scalars. In general, the set of transported scalars carried in a simulation, ϕ_k, could include mixture fraction, total enthalpy, a particular chemical species, or some more complicated composite quantity. In this

work, however, the only scalar equations considered are for mixture fraction and a progress variable.

Chemical property data, which are needed to determine ρ, μ, α_k, and w_k in terms of the ϕ_k, are provided by the chemistry models discussed in §3.3. The chemistry model will also provide complete chemical state information — data for all chemical species and temperature — in terms of the ϕ_k, even though only a small number of scalars are carried in (2.22).

Chapter 3

TURBULENCE AND CHEMISTRY MODELS

In this work, solutions to the reacting flow equations are obtained using the technique of large eddy simulation. The large, energy-containing scales of motion are simulated numerically while the small, unresolved scales and their interactions with the large scales are modeled. In this chapter, large eddy simulation principles are first reviewed; then standard dynamic models for subgrid stress, scalar flux, and scalar variance are given, and the assumed beta PDF for subgrid fluctuations of a conserved scalar is discussed. The chemistry models used in this work are all based on mixture fraction, which plays a fundamental role in non-premixed combustion. Traditional mixture-fraction based modeling approaches are discussed, and a new flamelet approach incorporating a progress variable is presented.

3.1 Filtering and the LES Equations

In large eddy simulation (LES), all of the field variables are decomposed into resolved and subgrid-scale parts. The resolved, large-scale fields are related to the instantaneous full-scale fields through a grid-filtering operation (indicated by an overbar symbol) that removes scales too small to be resolved by the simulation. Note that in the present study, filtering is implicitly defined by the computational grid used for the large-scale equations and that explicit filtering (Ghosal and Moin 1995; Vasilyev *et al.* 1998) is not used. Quantities per unit volume are treated using a Reynolds decomposition,

$$\rho = \overline{\rho} + \rho' \ ,$$

while quantities per unit mass are best described by a Favre (density-weighted) decomposition,

$$u = \widetilde{u} + u'' \ ,$$

where

$$\widetilde{u} = \overline{\rho u} \,/\, \overline{\rho} \ .$$

Note that with the Favre decomposition, filtered variables represent "mixed-mean" averages over subgrid volumes. This ensures that the filtering process does not alter the form of the conservation laws.

The LES equations for the resolved fields are formally derived by substituting the above decompositions into the governing equations, and then subjecting the equations to the grid filter. The instantaneous small-scale fluctuations are removed by the filter, but their statistical effects remain in unclosed residual terms representing the influence of the subgrid scales on the resolved scales. Applying this procedure to the working equations of §2.3, the LES equations are written (now using subscript notation) as:

Continuity:

$$\overline{\rho}_{,t} + (\overline{\rho}\widetilde{u}_j)_{,j} = 0 \tag{3.1}$$

Momentum:

$$(\overline{\rho}\widetilde{u}_i)_{,t} + (\overline{\rho}\widetilde{u}_i\widetilde{u}_j)_{,j} = -\overline{p}_{,i} + (2\overline{\mu}\widetilde{S}_{ij})_{,j} + t_{ij,j} \tag{3.2}$$

$$\widetilde{S}_{ij} = \tfrac{1}{2}(\widetilde{u}_{i,j} + \widetilde{u}_{j,i}) - \tfrac{1}{3}\delta_{ij}\widetilde{u}_{k,k}$$

Scalar Transport:

$$(\overline{\rho}\widetilde{\phi}_i)_{,t} + (\overline{\rho}\widetilde{u}_j\widetilde{\phi}_i)_{,j} = (\overline{\rho}\widetilde{\alpha}_i\widetilde{\phi}_{i,k})_{,k} + \overline{\rho}\widetilde{w}_i + q_{ik,k} \tag{3.3}$$

State Relation:

$$\overline{\rho} = \overline{f(\phi_1,\, \phi_2,\, \ldots)} \tag{3.4}$$

All unclosed transport terms in the momentum and scalar equations are grouped into the residual stress, t_{ij}, and residual scalar flux, q_{ik}. These terms as well as the filtered chemical source terms, $\widetilde{w}_i$, and the state relation require closure modeling.

3.2 Subgrid-Scale Models

Subgrid closure models for (3.1–3.4) are presented below. The dynamic procedure is first summarized in §3.2.1 because it is used whenever applicable to evaluate model coefficients. Closures for the filtered chemical source terms and the state relation, which are related to the chemical model, are discussed in §3.3.

3.2.1 The Dynamic Procedure

Since many of the subgrid closures considered utilize the dynamic modeling concept (Germano *et al.* 1991), it is briefly reviewed here in general form. The dynamic procedure is a method for calculating dimensionless scaling coefficients in subgrid-scale models for filtered nonlinear terms.

Consider an arbitrary nonlinear term, $t(u)$, which is a known function of the field variables, u, and suppose that we wish to determine its filtered value by modeling the subgrid residual with an algebraic model, $m(u)$, which depends on the field variables but in general can also depend explicitly on space and time and on other parameters such as the grid filter width, Δ. The value of the filtered term is then the sum of resolved and modeled parts:

$$\overline{t(u)} = t(\overline{u}) + m(\overline{u}) \ . \tag{3.5}$$

The basic idea behind the dynamic procedure is to consider how $t(u)$ and $m(u)$ vary with the filter width. In particular, an expression similar to (3.5) for the value of the filtered term at a larger filter width, referred to as the test filter, can be written:

$$\widehat{\overline{t(u)}} = t(\widehat{\overline{u}}) + m(\widehat{\overline{u}}) \ . \tag{3.6}$$

In dynamic modeling, filtering to the test level is indicated by a hat symbol. The test filter width is denoted by $\widehat{\Delta}$ and is usually taken to be twice the width of the grid filter, $\widehat{\Delta} = 2\Delta$.

If (3.5) is test filtered and subtracted from (3.6), an interesting identity results:

$$\widehat{t(\overline{u})} - t(\widehat{\overline{u}}) = m(\widehat{\overline{u}}) - \widehat{m(\overline{u})} \ . \tag{3.7}$$

Remarkably, all terms in this equation are computable from the known resolved field. It represents the "band-pass filtered" contribution to the nonlinear term in the scale range between the grid and test filter levels. A consistent subgrid model should contribute the same amount as the resolved field in this band. The key to the dynamic procedure is to use this identity as a constraint for calibration of subgrid-scale models.

Note that while (3.7) is an exact identity when $m(u)$ is the exact subgrid residual, it should only be expected to hold in a statistical sense (and should not be applied locally and instantaneously) when $m(u)$ is modeled. The reason for this is the following: In filtering the governing equations, we have replaced the instantaneous variations that occur within each subgrid volume with a statistical description of the subgrid state. However, the band-pass filtered fields in (3.7) are based on instantaneous data, and the test filtering process itself does not provide sufficient averaging to produce converged statistics in the band-pass filtered scale range. Furthermore, subgrid models are generally valid for predicting statistical properties of the subgrid scales but usually cannot account for instantaneous subgrid fluctuations. Requiring (3.7) to be satisfied locally forces the model to operate beyond its range of validity, resulting in unphysical fluctuations in model behavior. This may explain why LES practitioners have found that some form of averaging is required in order to compute stable model coefficients with the dynamic procedure. Related discussions are given by Ghosal *et al.* (1995) and Carati and Eijnden (1997).

For the dynamic procedure to be applicable, the quantity to be modeled must vary substantially between the grid and test filter scales; otherwise, the difference in (3.7) will not be significant and cannot be used for modeling subgrid-scale quantities. Examples of quantities that cannot be modeled dynamically are dissipation and chemical reaction rates, because these phenomena occur almost exclusively at the smallest scales, which are always unresolved in LES.

The dynamic procedure is usually applied to situations in which the subgrid model can be written as,

$$m(\overline{u}) = c\ s(\overline{u}, \Delta)\ , \tag{3.8}$$

where $s(\overline{u}, \Delta)$ is a dimensionally consistent algebraic scaling law and c is an unknown dimensionless coefficient, which in the dynamic procedure is allowed to vary in space and time. Substituting this form into (3.7) we obtain,

$$\widehat{t(\overline{u})} - t(\widehat{\overline{u}}) = c^* s(\widehat{\overline{u}}, \widehat{\Delta}) - \widehat{c\ s(\overline{u}, \Delta)}\ , \tag{3.9}$$

where c^* is the model coefficient at the test filter level. Note that c has been left

inside the test filtering operator in the right most term.

At this point, the various forms of the dynamic procedure differ as to how to use this equation to calculate the model coefficient, c. In the present study, it is assumed that c is a statistical quantity that varies slowly in space and time and is both scale invariant and independent of the directions in which the flow is statistically homogeneous. We therefore set $c^* = c$ and allow c to pass through the test filtering operator. To simplify notation the following substitutions are made:

$$\mathcal{L} = \widehat{t(\overline{u})} - t(\widehat{\overline{u}}) \ , \qquad \mathcal{M} = s(\widehat{\overline{u}}, \widehat{\Delta}) - \widehat{s(\overline{u}, \Delta)} \ ,$$

where, $\mathcal{L}$ is called the Leonard term and $\mathcal{M}$ is the model term. The equation for c can then be written as,

$$\mathcal{L} = c \, \mathcal{M} \ . \tag{3.10}$$

To obtain a single value for c in each homogeneous region of the flow, and to determine c in cases where $\mathcal{L}$ and $\mathcal{M}$ are nonparallel vectors or tensors, (3.10) is solved by least-squares (Lilly 1992). The final expression is:

$$c = \frac{\langle \mathcal{L} \cdot \mathcal{M} \rangle}{\langle \mathcal{M} \cdot \mathcal{M} \rangle} \ , \tag{3.11}$$

where the angle brackets indicate averaging over directions of flow homogeneity.

3.2.2 Turbulent Stress and Scalar Flux

Subgrid momentum and scalar transport terms that appear in (3.2) and (3.3) are modeled using the dynamic approach of Moin *et al.* (1991). The present formulation differs from Moin *et al.* in the use of the deviatoric strain rate for the definition of $|\widetilde{S}|$ and in the use of least-squares averaging.

The residual stresses are modeled as subgrid turbulent stresses with an eddy viscosity assumption,

$$t_{ij} = -\overline{\rho}\widetilde{u_i u_j} + \overline{\rho}\,\widetilde{u}_i\widetilde{u}_j = 2\mu_t \widetilde{S}_{ij} - \tfrac{1}{3}\overline{\rho} q^2 \delta_{ij} \ , \tag{3.12}$$

where $\frac{1}{2}\overline{\rho} q^2$ is the subgrid kinetic energy and,

$$\widetilde{S}_{ij} = \tfrac{1}{2}(\widetilde{u}_{i,j} + \widetilde{u}_{j,i}) - \tfrac{1}{3}\delta_{ij}\widetilde{u}_{k,k} \ .$$

The eddy viscosity is given by the Smagorinsky model,

$$\mu_t = C_\mu \overline{\rho} \Delta^2 |\widetilde{S}| \ , \quad \text{where} \quad |\widetilde{S}| = \sqrt{\widetilde{S}_{ij} \widetilde{S}_{ij}} \ , \tag{3.13}$$

and the subgrid kinetic energy is modeled using,

$$\overline{\rho} q^2 = C_k \overline{\rho} \Delta^2 |\widetilde{S}|^2 \ . \tag{3.14}$$

Note, however, that the isotropic part of the residual stress does not need to be modeled separately when pressure is decoupled from thermodynamic variables, because it may then be lumped together with the pressure. In the present study, acoustic interactions and compressibility are neglected, so in the interest of computational efficiency, this term is not actually computed.

The residual scalar fluxes are modeled as subgrid turbulent scalar fluxes with a gradient-diffusion assumption,

$$q_{ik} = -\overline{\rho} \widetilde{u_k \phi_i} + \overline{\rho}\, \widetilde{u}_k \widetilde{\phi}_i = \overline{\rho} \alpha_t \widetilde{\phi}_{i,k} \ , \tag{3.15}$$

where the eddy diffusivity is given by,

$$\overline{\rho} \alpha_t = C_\alpha \overline{\rho} \Delta^2 |\widetilde{S}| \ . \tag{3.16}$$

Note that the eddy diffusivity model has the same algebraic form as the eddy viscosity model, but the model coefficient is different. The ratio of the two coefficients gives the subgrid turbulent Prandtl number, $Pr_t = C_\mu / C_\alpha$.

The coefficients in all of these models, C_μ, C_k, and C_α, are evaluated using the dynamic procedure. To simplify the expressions for the coefficients, the following notation for density-weighted test filtering is introduced:

$$\check{\widetilde{u}} = \widehat{\overline{\rho}\, \widetilde{u}} \, / \, \widehat{\overline{\rho}} \ .$$

For the subgrid turbulent stress model (3.12) the dynamic procedure gives,

$$C_\mu = \frac{\langle \mathcal{L}_{ij} \mathcal{M}_{ij} \rangle}{2 \langle \mathcal{M}_{kl} \mathcal{M}_{kl} \rangle} \ , \quad \mathcal{L}_{ij} = -\widehat{\overline{\rho}\, \widetilde{u}_i \widetilde{u}_j} + \widehat{\overline{\rho}}\, \check{\widetilde{u}}_i \check{\widetilde{u}}_j \ , \quad \mathcal{M}_{ij} = \widehat{\overline{\rho}} \widehat{\Delta}^2 |\check{\widetilde{S}}| \check{\widetilde{S}}_{ij} - \widehat{\overline{\rho} \Delta^2 |\widetilde{S}| \widetilde{S}_{ij}} \ .$$

For the subgrid turbulent scalar flux model (3.15) the coefficient is calculated from,

$$C_\alpha = \frac{\langle \mathcal{L}_i \mathcal{M}_i \rangle}{\langle \mathcal{M}_j \mathcal{M}_j \rangle} \ , \quad \mathcal{L}_i = -\widehat{\overline{\rho}\widetilde{u}_i\widetilde{\phi}} + \widehat{\overline{\rho}}\check{\widetilde{u}}_i\check{\widetilde{\phi}} \ , \quad \mathcal{M}_i = \widehat{\overline{\rho}}\widehat{\Delta}^2|\check{\widetilde{S}}|\check{\widetilde{\phi}}_{,i} - \widehat{\overline{\rho}\Delta^2|\widetilde{S}|\widetilde{\phi}_{,i}} \ .$$

Although it is not actually used in the present study, the expression for the subgrid kinetic energy coefficient is the following:

$$C_k = \frac{\langle \mathcal{L}\mathcal{M} \rangle}{\langle \mathcal{M}^2 \rangle} \ , \quad \mathcal{L} = \widehat{\overline{\rho}\,\widetilde{u}_k\widetilde{u}_k} - \widehat{\overline{\rho}}\,\check{\widetilde{u}}_k\check{\widetilde{u}}_k \ , \quad \mathcal{M} = \widehat{\overline{\rho}}\widehat{\Delta}^2|\check{\widetilde{S}}|^2 - \widehat{\overline{\rho}\Delta^2|\widetilde{S}|^2} \ .$$

There is a minor defect in the dynamic procedure when applied to scalar transport: In a region where the flow is turbulent but the scalar is uniform or fully mixed, the dynamic procedure does not define an eddy diffusivity. When this situation arises in practice, the eddy diffusivity is set to zero. This normally does not pose a problem in regions of uniform scalar because the scalar gradient, which multiplies the eddy diffusivity, is also zero. However, since scalar transport is linear in the scalar, the eddy diffusivity should in principle depend only on the velocity field, should be the same for all scalars, and should be nonzero where the velocity is turbulent. When multiple scalar transport equations are solved simultaneously, one could compute a different eddy diffusivity for each scalar, or compute a least-squares average diffusivity using all the scalars, or base the eddy diffusivity calculation on a single, chosen scalar. In the present study, eddy diffusivity is computed using the mixture fraction and then applied to all scalars.

3.2.3 Variance and Dissipation Rate of a Conserved Scalar

Subgrid scalar variance is an input parameter to the assumed PDF model of §3.2.4, while scalar dissipation rate is a parameter in flamelet models of turbulent combustion (§3.3.3). Starting from assumptions of local homogeneity and local equilibrium for the subgrid scales, Pierce and Moin (1998c) derived algebraic models for subgrid variance and dissipation rate. The subgrid variance is modeled using,

$$\overline{\rho}\,\widetilde{\phi''^2} = C_\phi\,\overline{\rho}\,\Delta^2|\nabla\widetilde{\phi}|^2 \ , \tag{3.17}$$

and the filtered dissipation rate, $\overline{\rho}\,\widetilde{\chi} = \overline{\rho\alpha_m|\nabla\phi|^2}$, is modeled by,

$$\overline{\rho}\,\widetilde{\chi} = \overline{\rho}(\alpha_m + \alpha_t)|\nabla\widetilde{\phi}|^2 \ , \tag{3.18}$$

where α_m is the molecular diffusivity and α_t is the turbulent diffusivity of §3.2.2. Dynamic evaluation of C_ϕ is summarized by the following:

$$C_\phi = \frac{\langle \mathcal{L}\mathcal{M}\rangle}{\langle \mathcal{M}^2\rangle} \ , \quad \mathcal{L} = \widehat{\overline{\rho}\,\widetilde{\phi}\widetilde{\phi}} - \widehat{\overline{\rho}}\,\breve{\widetilde{\phi}}\breve{\widetilde{\phi}} \ , \quad \mathcal{M} = \widehat{\overline{\rho}}\widehat{\Delta}^2|\nabla\breve{\widetilde{\phi}}|^2 - \widehat{\overline{\rho}\Delta^2|\nabla\widetilde{\phi}|^2} \ .$$

Pierce and Moin presented (3.17) as an alternative to the scale-similarity model of Cook and Riley (1994). An alternative derivation for (3.18) to that of Girimaji and Zhou (1996) was presented to emphasize the local equilibrium and dynamic modeling ideas. Note that when (3.17) is applied to mixture fraction, the dynamic procedure does not guarantee that the predicted variance is physically realizable. In practice, variance predictions lying outside the physically allowed range, $0 \le \widetilde{Z''^2} \le \widetilde{Z}(1-\widetilde{Z})$, are clipped.

3.2.4 Assumed Beta PDF for a Conserved Scalar

While algebraic scaling laws and scale-similarity concepts can be expected to work for quadratic nonlinearities, the only acceptable closure for arbitrary nonlinearities appears to be the probability density function (PDF) approach. For example, the state relation for density (3.4) can in general be an arbitrary nonlinear function of the scalar variables. If the joint PDF of the subgrid scalar fluctuations, $P(\phi_1,\, \phi_2,\, \ldots)$, were known, the filtered density could be evaluated using,

$$\overline{\rho} = \overline{f(\phi_1,\, \phi_2,\, \ldots)} = \int f(\phi_1,\, \phi_2,\, \ldots)P(\phi_1,\, \phi_2,\, \ldots)\, d\phi_1\, d\phi_2\, \ldots \ . \tag{3.19}$$

When Favre filtering is used for the scalar variables, it is more appropriate to evaluate filtered quantities using the joint Favre PDF of the subgrid scalar fluctuations. Analogous to (3.19), Favre-filtered quantities would be evaluated using,

$$\widetilde{y} = \int y(\phi_1,\, \phi_2,\, \ldots)\widetilde{P}(\phi_1,\, \phi_2,\, \ldots)\, d\phi_1\, d\phi_2\, \ldots \ , \tag{3.20}$$

where the density-weighted Favre PDF is related to the standard PDF by,

$$\widetilde{P}(\phi_1,\, \phi_2,\, \ldots) = \frac{\rho(\phi_1,\, \phi_2,\, \ldots) P(\phi_1,\, \phi_2,\, \ldots)}{\overline{\rho}} \ . \tag{3.21}$$

The Reynolds-filtered density can be obtained using $\widetilde{P}$ by dividing (3.21) by ρ and integrating, with the result that,

$$\overline{\rho} = \left[\int \frac{\widetilde{P}(\phi_1,\, \phi_2,\, \ldots)}{\rho(\phi_1,\, \phi_2,\, \ldots)}\, d\phi_1\, d\phi_2\, \ldots \right]^{-1} \ . \tag{3.22}$$

In the assumed PDF method, the probability density function is modeled directly using simple analytical forms, such as the beta distribution. However, because source terms can directly modify the PDF of a scalar, the beta distribution can be expected to be valid only for conserved scalars. For this reason, it is applied only to mixture fraction in this work. Assumed-PDF modeling of reacting scalars is a topic for further research.

The two-parameter family of beta distributions on the interval, $0 \leq x \leq 1$, is given by,

$$P(x;\, a, b) = x^{a-1}(1-x)^{b-1}\, \frac{\Gamma(a+b)}{\Gamma(a)\, \Gamma(b)} \ , \tag{3.23}$$

where the parameters a and b are related to the distribution mean and variance $(\mu,\, \sigma^2)$ by

$$a = \frac{\mu(\mu - \mu^2 - \sigma^2)}{\sigma^2} \ , \qquad b = \frac{(1-\mu)(\mu - \mu^2 - \sigma^2)}{\sigma^2} \ .$$

When applied to mixture fraction, $x \to Z$, $\mu \to \widetilde{Z}$, and $\sigma^2 \to \widetilde{Z''^2}$.

The beta PDF has been evaluated as a model for subgrid mixture fraction fluctuations in large eddy simulations in several studies using *a priori* tests on direct numerical simulation data. Cook and Riley (1994) tested the beta PDF in the context of the fast chemistry model (§3.3.2) in homogeneous turbulence. Jiménez *et al.* (1997) demonstrated the good performance of the beta PDF model using data from a highly intermittent, incompressible, turbulent mixing layer. Wall and Moin (2000) tested the beta PDF in the presence of heat release. It has also been shown (Wall *et al.* 2000; Cook and Riley 1994) that accurate prediction of the subgrid variance is the most important factor in obtaining good results with the beta PDF.

The state relation and other nonlinear functions are often known prior to conducting a simulation, in which case the PDF integrals can be calculated and stored into lookup tables before the simulation begins. The filtered density and other filtered quantities can then be efficiently retrieved during the simulation as functions of the known filtered scalars and variances:

$$\overline{\rho} = F(\widetilde{\phi}_1, \widetilde{\phi}_2, \ldots, \widetilde{\phi_1''^2}, \widetilde{\phi_2''^2}, \widetilde{\phi_1'' \phi_2''}, \ldots) \; . \tag{3.24}$$

3.3 Chemistry Models

Developing effective strategies for incorporating chemistry into large eddy simulations was one of the main objectives of this work. The straightforward, brute-force approach would be to find a suitable chemical kinetic mechanism for the system under investigation, solve scalar transport equations for all the species in the mechanism, and attempt to model the filtered source term in each equation.

A serious problem with this direct approach is that realistic kinetic mechanisms can involve tens of species and hundreds of reaction steps, even for "simple" fuels such as methane. Unless mechanism reduction methodologies can drastically reduce the dimensionality of the chemical system, one is faced with having to solve a large number of stiffly coupled scalar transport equations.

Another problem is that each species transport equation contains a filtered chemical source term that must be modeled. Like the state relation (3.4), each chemical source term is, in principle, an arbitrary nonlinear function of the scalar variables. As discussed in §3.2.4, PDF methods are the most attractive approach for evaluating such nonlinearities; however, when the number of independent variables becomes large (say, more than three) joint PDF's can become unwieldy.

Thus, the key to combustion modeling in LES appears to be minimizing the number of transported scalar variables required. For non-premixed combustion, mixture-fraction based models appear to offer the most effective description of the chemistry. By mapping the details of the multicomponent diffusion-reaction processes to a small number of "tracking" scalars, complete chemical state information can be obtained at greatly reduced computational expense.

3.3.1 The Role of Mixture Fraction

All of the chemistry models considered in this work are based on the concept of mixture fraction. The role of mixture fraction in non-premixed combustion is best described as a tracking scalar because it tracks the mixing of inflow streams, the transport of conserved scalars, and the advection of reactive scalars.

A Mixture Tracking Scalar

At its most basic level, mixture fraction (denoted by Z in this work) is a generic mixing variable that represents the relative amount that each inflow stream contributes to the local mixture. When the the inflow streams are fuel and oxidizer, mixture fraction can be thought of as specifying the fuel-air ratio or stoichiometry of the local mixture.

Mixture fraction is also a conserved scalar that is representative of other conserved scalars in the flow. Equations for conserved scalars can be formally derived by taking linear combinations of species transport equations in such a way that reaction source terms cancel. The resulting equation will describe a physical quantity that is conserved during chemical reaction, such as total enthalpy or the mass fraction of a particular chemical element. Except for differences due to effects of differential diffusion and boundary conditions, every conserved scalar satisfies the advection-diffusion equation, here written for mixture fraction:

$$\frac{\partial \rho Z}{\partial t} + \nabla \cdot (\rho \boldsymbol{u} Z) = \nabla \cdot (\rho \alpha_Z \nabla Z) \ . \tag{3.25}$$

Because conserved scalar transport is linear, a small number of conserved scalars forming a complete basis is sufficient to construct all other conserved scalars by superposition. A flow system containing n inflow ports would in general require n mixture fraction variables to form a complete basis, but because all the normalized mixture fractions must sum to unity, only $n - 1$ mixture fraction variables are needed. By convention, a mixture fraction variable is assigned the value 1 in the flow port from which it emanates and zero in all others. Values of mixture fraction between 0 and 1 indicate the mass fraction that a particular stream contributes to the local mixture.

The standard mixture fraction used in non-premixed combustion, Z, is the fuel-stream mixture fraction and is therefore unity in the fuel stream and zero in the oxidizer stream. The mixture fraction for the oxidizer stream is then given by $1-Z$. When there are more than two inflow ports supplying independent species compositions and/or enthalpy content, an additional mixture fraction variable can be added for each additional port. When thermal radiation or heat transfer to boundaries is important, total enthalpy should be treated as an independent conserved scalar, but otherwise it can be directly related to mixture fraction.

Utility with Differential Diffusion

In the absence of differential diffusion, the diffusivity in (3.25) is the same for all scalars and mixture fraction tracks other conserved scalars exactly. However, when differential diffusion effects are present, mixture fraction tracks other conserved scalars only approximately. As noted in §2.2, differential diffusion can generally be neglected in the large scale transport resolved by LES, and therefore, considerations of differential diffusion will be limited mainly to the subgrid-scale model.

With differential diffusion, the mixture fraction concept is still very useful, but the definition of mixture fraction is not as straightforward. Pitsch and Peters (1998) suggest that (3.25), with α_Z prescribed, be taken as the definition of Z. But in the present work, an average mixture fraction is defined by combining the conserved elemental (atomic) mass fractions. The elemental mass fractions, a_j, are given in terms of the species mass fractions by,

$$a_j = \sum_i y_i N_{ij} A_j / M_i \ , \qquad j = 1, \ldots, N_E \ , \tag{3.26}$$

where N_{ij} is the number of j atoms in each molecule of species i, A_j are atomic weights, and N_E is the total number of distinct chemical elements present in the system. The average mixture fraction for a two-feed system is then given by summing the elemental mass fractions and normalizing the result,

$$Z = \frac{\sum_i |a_i - a_i^0|}{\sum_j |a_j^1 - a_j^0|} \ , \tag{3.27}$$

where a_i^0 and a_i^1 are elemental mass fractions in the oxidizer and fuel streams, respectively. Also, an average mixture-fraction diffusivity can be defined in a similar manner by combining the elemental diffusive fluxes,

$$\boldsymbol{a}_j = \sum_i \rho y_i \boldsymbol{V}_i N_{ij} A_j / M_i \ , \qquad j = 1, \ldots, N_E \ , \tag{3.28}$$

and equating the mixture fraction flux to the normalized result,

$$\rho \alpha_Z |\nabla Z| = \frac{\sum_i |\boldsymbol{a}_i|}{\sum_j |a_j^1 - a_j^0|} \ . \tag{3.29}$$

Note that (3.27) and (3.29) are consistent with each other such that solving (3.25) with α_Z given by (3.29) is equivalent to using (3.27). The above definitions are used in the present work to define mixture fraction and its diffusivity when computing flamelet solutions in physical space (§3.3.3).

Utility in Flamelet Models

Another important property of the mixture fraction is its ability to account for turbulent advection in diffusion flames. Because the velocity field transports all scalars equally, changes in species mass fractions *with respect to mixture fraction* are due only to diffusion and reaction. (In the absence of diffusion and reaction, relationships between mixture fraction and other scalars would be exactly preserved.) The implication is that turbulent combustion, when viewed relative to mixture fraction, is simply laminar diffusion-reaction in an unsteady straining environment created by turbulent advection. This principle is the basis of *flamelet models*, in which explicit velocity dependence is removed from the scalar transport equations by relating the scalars to the mixture fraction, which itself does depend on the velocity field.

By itself, mixture fraction does not contain any information about chemical reactions in the mixture. Assumptions such as fast chemistry or steady flamelet state relationships are needed to associate a chemical state with the mixture fraction. Also, mixture fraction cannot account for chemical variations in directions perpendicular to its gradient. To address these and other problems, an additional tracking scalar in the form of a progress variable is introduced in §3.3.4.

3.3.2 Fast Chemistry Assumption

One of the simplest approaches for relating chemical states to mixture fraction is to assume *equilibrium chemistry*, the condition that chemical kinetics are infinitely fast relative to other processes in the flow (high Damköhler number limit), so that the mixture is always completely reacted, or in a state of chemical equilibrium. A similar assumption, called *fast chemistry* (also known as the Burke-Schumann limit), is equilibrium chemistry combined with a one-step, global reaction or "major products" assumption. The opposite extreme of fast chemistry is the case of *pure mixing* (or frozen chemistry), the limit in which chemical reactions are negligible.

With each of these assumptions the chemical composition is a unique function of mixture stoichiometry, total enthalpy, and pressure. For constant background pressure, unity Lewis numbers, negligible thermal radiation, and adiabatic walls, all chemical variables become functions of mixture fraction alone:

$$y_i = y_i(Z) \ , \qquad T = T(Z) \ , \qquad \rho = \rho(Z) \ . \tag{3.30}$$

These functions constitute what may be called "chemical state relationships", and can be computed using an equilibrium chemistry code such as STANJAN (Reynolds 1986). When combined with the assumed PDF of §3.2.4 for mixture fraction, this provides complete closure for the problem, and all of the filtered combustion variables can be expressed as functions of filtered mixture fraction and mixture fraction variance:

$$\widetilde{y}_i = \widetilde{y}_i(\widetilde{Z}, \widetilde{Z''^2}) \ , \quad \widetilde{T} = \widetilde{T}(\widetilde{Z}, \widetilde{Z''^2}) \ , \quad \overline{\rho} = \overline{\rho}(\widetilde{Z}, \widetilde{Z''^2}) \ , \quad \textit{etc.} \tag{3.31}$$

Note that (3.31) includes similar expressions for filtered transport properties such as $\overline{\mu}$ and $\widetilde{\alpha}_Z$, which are used when solving the large-scale momentum and scalar transport equations. The computational cost of the fast chemistry model is negligible, because the functions in (3.31) can be precomputed and tabulated prior to running a simulation.

Example state relationships for temperature, $T(Z)$, are plotted in Fig. 3.1 for equilibrium chemistry, fast chemistry, and pure mixing assumptions. Note that

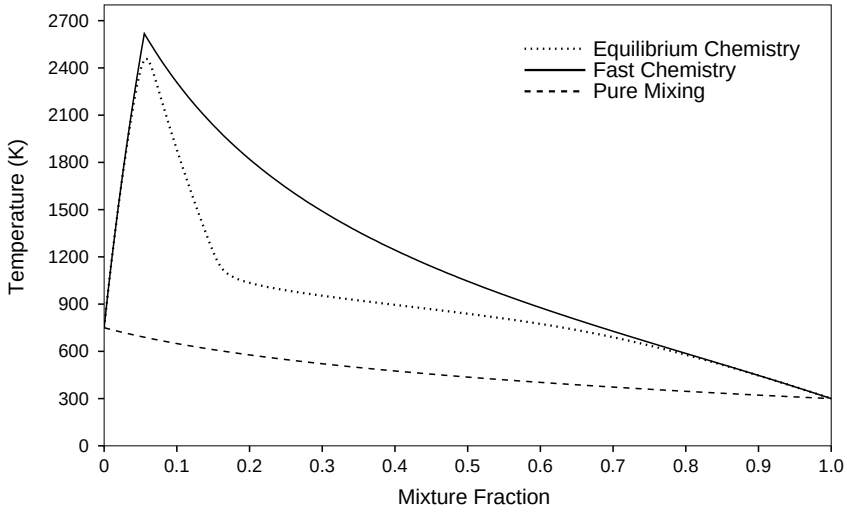

Fig. 3.1 Temperature as a function of mixture fraction from equilibrium and fast chemistry state relationships. Methane-air combustion at the conditions of the experiment in §5.1 (750K air, 300K fuel, 3.8 atm).

equilibrium chemistry predicts much lower temperatures than fast chemistry in the fuel-rich region. This is caused by the endothermic breakdown of hydrocarbon fuel into CO and H_2; but in reality, chemical kinetic mechanisms to achieve this conversion are very slow or nonexistent. Because of this defect in equilibrium chemistry, the fast chemistry assumption may be preferable for hydrocarbon fuels.

Since the fast chemistry model does not incorporate any chemical kinetic information, it is limited to situations in which kinetics do not play a role. Accordingly, the model cannot account for any effect of turbulence on the chemistry, and cannot account for ignition and extinction phenomena as occur, for example, in the region upstream of a lifted flame. Nevertheless, it is a convenient starting point for the development of more capable models.

3.3.3 Classical Steady Flamelets

Although the steady flamelet model is sometimes introduced in a conceptually different framework than the fast chemistry model above, the two models are actually very similar. They both rely on a single scalar transport equation for the mixture fraction and employ "chemical state relationships" to relate all chemical variables to

the mixture fraction. The only difference is that the steady flamelet model replaces equilibrium chemical states (obtained from thermochemistry alone) with solutions to one-dimensional, steady, diffusion-reaction equations. The chemical reactions, although finite-rate, are assumed to be at all times in balance with the rate at which reactants diffuse into the flame, so that flame properties are directly related to the scalar dissipation (or mixing) rate. The result is a modest improvement over fast chemistry, allowing for more realistic chemical state relationships. Like the fast chemistry model, steady flamelets cannot account for extinction (when reaction rate is lower than mixing rate), ignition (when reaction rate is higher than mixing rate), or the effects of unsteady mixing (when reaction rate lags behind changes in mixing rate). The flamelet/progress-variable approach discussed in §3.3.4 overcomes all of these limitations by using a (dynamic) chemical variable instead of the (kinematic) dissipation rate to parameterize flamelet evolution.

One approach to deriving the steady flamelet model is to start with the assumption that in each region of the flow, all chemical species are given by unique functions of the mixture fraction,

$$y_i = f_i(Z) \ . \tag{3.32}$$

Derivatives of chemical species can then be related to derivatives of mixture fraction:

$$y_{i,t} = f_i' Z_{,t} \ , \qquad y_{i,j} = f_i' Z_{,j} \ . \tag{3.33}$$

For (3.32) to be valid locally, species mass fractions must vary slowly in directions perpendicular to the mixture-fraction gradient and chemical reactions must be in balance with species diffusion along the mixture-fraction gradient, so that the flame is locally one-dimensional and steady.

Using (3.33), the species conservation equations can be "transformed" from physical space to mixture-fraction space. For the moment, assume unity Lewis numbers so that all species, enthalpy, and mixture fraction have a common diffusivity, α. Substituting (3.33) into the species transport equations (2.1) and rearranging while noting that $f_{i,k}' = f_i'' Z_{,k}$, one obtains,

$$f_i' \left[\rho(Z_{,t} + u_j \, Z_{,j}) - (\rho\alpha Z_{,k})_{,k}\right] = \rho\alpha Z_{,k} Z_{,k} f_i'' + \rho w_i \ .$$

The quantity in brackets on the left-hand side of this equation is identically zero, leaving us with the steady flamelet equations,

$$\rho\chi\frac{d^2y_i}{dZ^2} = -\rho w_i \ , \tag{3.34}$$

where $\chi = \alpha Z_{,k}Z_{,k}$ is the mixture-fraction dissipation rate. In order to solve (3.34), an additional assumption is needed to prescribe the dissipation rate as a function of mixture fraction, $\chi = \chi(Z)$.

Physical-Space Formulation

In the present study, the flamelet equations are formulated and solved in *physical space* rather than in mixture-fraction space, and the physical-space solutions are later remapped to mixture fraction. In physical space, it is more natural to consider the full combustion equations of §2.1 and reduce them to the case of one-dimensional, steady combustion. Most of the assumptions of §2.2 are maintained, except that the full multicomponent diffusion mechanisms (including Soret and Dufour effects) may be used. Continuity and momentum equations are not solved because the velocity is to be imposed. The physical space (x-coordinate) flamelet equations can then be written as:

$$\begin{aligned}
\rho u y_{i,x} &= -(\rho y_i V_i)_{,x} + \rho w_i \ , \\
\rho u h_{,x} &= (\kappa T_{,x} - \textstyle\sum_i \rho V_i y_i h_i - q_D)_{,x} \ , \\
h &= \textstyle\sum_i y_i h_i(T) \ , \\
\rho &= p_0 / \textstyle\sum_i \dfrac{y_i}{M_i}\hat{R}T \ ,
\end{aligned} \tag{3.35}$$

where q_D is the Dufour heat flux. Mixture fraction is defined in terms of the species mass fractions by (3.27), but one could instead include an equation for mixture fraction,

$$\rho u Z_{,x} = (\rho\alpha_Z Z_{,x})_{,x} \ , \tag{3.36}$$

in which α_Z would be prescribed. Note that solving (3.36) with α_Z given by (3.29) is equivalent to using (3.27).

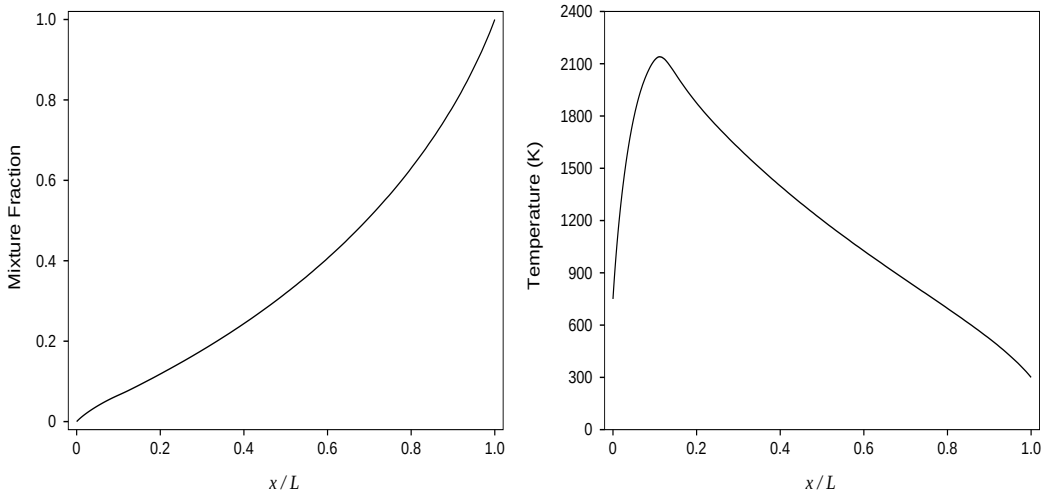

Fig. 3.2 Mixture fraction and temperature from a steady flamelet solution in physical space. Methane-air combustion at the conditions of the experiment in §5.1 (750K air, 300K fuel, 3.8 atm). $L = 0.2$ cm.

Like the dissipation rate in (3.34), the velocity in the physical-space equations, $u(x)$, needs to be prescribed. In fact, the solution of (3.36) with an assumed form for $u(x)$ yields a corresponding $\chi(Z)$. The standard flamelet approach (Peters 1984; Cook *et al.* 1997) usually assumes a counterflow configuration with $u(x) = -Sx$, where S is the strain rate. While this assumption may be supported by limited empirical evidence, it cannot be justified physically, as it violates the continuity equation to suppose that the entire flame surface could be subjected to local counterflow; there must be a proportionate amount of flame surface experiencing local reverse-counterflow. The counterflow configuration has also been proposed to account for self-similar thickening of the flame over time with $Z_{,t} = -(Sx)Z_{,x}$, where in this case S is the thickening rate. However, there is little reason to expect this to be valid in a turbulent flow, where mixing layers are constantly subjected to varying strain rates at various Z locations. The counterflow assumption places an undue bias on the flamelet solutions by imposing very specific $u(x)$ and corresponding $\chi(Z)$ profiles. In a turbulent flow, where both the velocity field and dissipation rate fluctuate strongly, the dissipation rate is usually not correlated with mixture fraction. In the absence of a stochastic description of $u(x)$ or $\chi(Z)$, the most unbiased assumption is, $u(x) = 0$ or $\chi(Z) \simeq$ constant.

With the assumption $u(x) = 0$, the flamelet equations can be regarded as pure diffusion-reaction equations. The length scale of the flame is set by imposing Dirichlet boundary conditions on species and enthalpy at the ends of a finite domain of length L. The point $x = 0$ corresponds to oxidizer stream conditions, while fuel stream conditions are enforced at $x = L$. The effect of strain on the flame is introduced through contraction and expansion of the domain length. Each flamelet solution is associated with a single, constant value of mixture-fraction diffusive flux, which shall be denoted by $\psi = \rho\alpha_Z|\nabla Z|$. Solution of (3.36) yields $Z_{,x} = \psi/\rho\alpha_Z$ and $\rho\chi = \psi^2/\rho\alpha_Z$. An average dissipation rate for the flamelet solution can be defined by $\chi_0 = \psi/\rho_0 L$, where ρ_0 is a constant reference density for the flamelet. The parameter χ_0 will later be made to correspond with the actual dissipation rate in the flow. This configuration does give rise to an inconsistency at the endpoints, $x = 0$ and $x = L$, where physically, the fluxes must go to zero as they are absorbed by unsteady growth of the mixing layer. But in practice, this is not expected to cause any problems because in the endpoint fringe regions, the chemical state must approach the fixed inflow stream conditions regardless. A typical flamelet solution in physical space is shown in Fig. 3.2. Provided that the mixture fraction solution, $Z(x)$, is a monotonic function of the spatial coordinate, the inverse function $x(Z)$ can be obtained and used to remap all of the combustion variables to mixture fraction.

By varying the domain length, L, a one-parameter family of steady flamelet solutions is obtained. The entire family of solutions is compiled into a *flamelet library*, to yield chemical state relationships of the form,

$$y_i = y_i(Z, \chi_0) \ , \qquad T = T(Z, \chi_0) \ , \qquad \rho = \rho(Z, \chi_0) \ , \tag{3.37}$$

where the solution dependence on L has been remapped to the dissipation rate parameter, χ_0, which varies monotonically with L. An example of a flamelet library is depicted in Fig. 3.3, where $T(Z, \chi_0)$ is plotted for several values of χ_0. Also shown is the equilibrium temperature curve from Fig. 3.1. It is apparent from the figure that equilibrium chemistry can be obtained as a special case of the steady flamelet

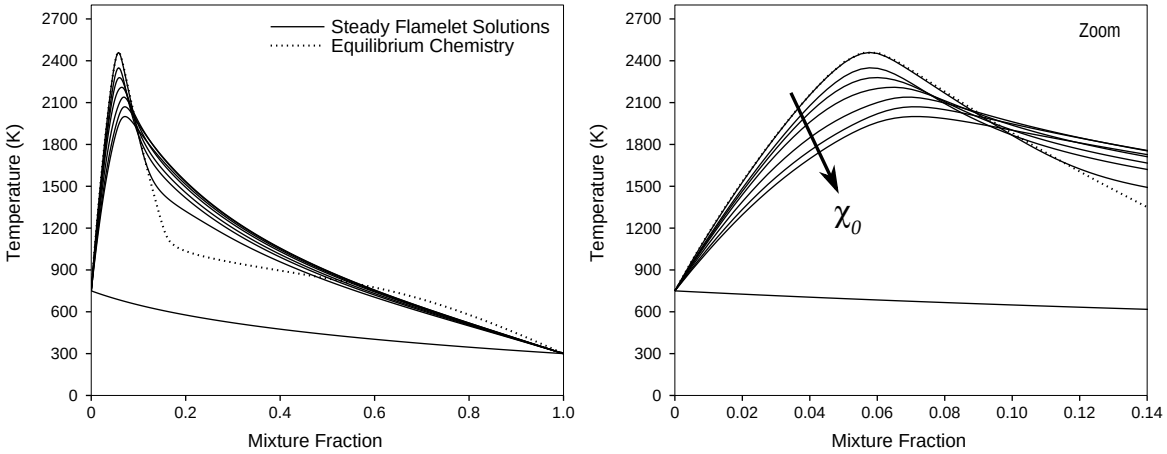

Fig. 3.3 A family of solutions for the steady, one-dimensional, diffusion-reaction equations, mapped to mixture fraction. Methane-air combustion at the conditions of the experiment in §5.1 (750K air, 300K fuel, 3.8 atm).

model in the limit $\chi_0 \to 0$.

Equilibrium Limit

The limiting behavior of the flamelet solutions as $\chi_0 \to 0$ ($L \to \infty$) is an important issue. As the domain length is increased, mixing and reaction rates become slower, and the chemical state moves closer to equilibrium. At some point, however, the length of the flamelet domain will become greater than the physical dimension of the combustor, and the flamelet time scale will become greater than the flow residence time in the combustor. It would seem that the $\chi_0 \to 0$ limit has little physical relevance, yet the flamelet model must provide chemical state information when the dissipation rate is zero, either instantaneously or in a well-mixed reactant or product region. This problem is a symptom of the limitations of the steady flamelet approximation and can become serious if one attempts to use the steady flamelet model to calculate pollutant concentrations in the well-mixed exhaust gases exiting the combustor, where equilibrium chemistry can give notoriously inaccurate predictions. In many practical problems, slow chemical processes, such as pollutant formation and thermal radiation, prevent equilibrium states from being reached by the time mixing is complete. This is an example of where the flamelet/progress-variable approach of §3.3.4 offers improvement. By using a chemical progress variable instead

of dissipation rate to parameterize the flamelets, the chemical state in a well-mixed region need not be at equilibrium but may continue to evolve slowly according to the chemical kinetics.

Differential Diffusion

Another issue related to the $\chi_0 \to 0$ limit is the treatment of differential diffusion. As noted in §2.2, differential diffusion effects are generally negligible at the larger scales because of turbulent transport. Thus, as the flamelet domain becomes longer, turbulence contributes increasingly to species transport inside the flamelet and the effects of differential diffusion diminish. Furthermore, the correct limiting behavior to equilibrium chemistry will only be obtained when differential diffusion is absent. To account for the effects of turbulent transport in the flamelet solutions, an eddy diffusivity, α_t, is introduced directly into the flamelet equations. The species, enthalpy, and mixture fraction equations then become,

$$\begin{aligned} \rho u y_{i,x} &= (\rho \alpha_t \, y_{i,x})_{,x} - (\rho y_i V_i)_{,x} + \rho w_i \ , \\ \rho u h_{,x} &= (\rho \alpha_t \, h_{,x})_{,x} + (\kappa T_{,x} - \textstyle\sum_i \rho V_i y_i h_i - q_D)_{,x} \ , \\ \rho u Z_{,x} &= (\rho \alpha_t Z_{,x})_{,x} + (\rho \alpha_Z Z_{,x})_{,x} \ . \end{aligned} \tag{3.38}$$

These equations would then replace (3.35). The value of the eddy diffusivity need not be specified precisely, because the flamelet solutions are parameterized by the total dissipation rate, $\chi_0 = \rho(\alpha_t + \alpha_Z)|\nabla Z|/\rho_0 L$, which will eventually be related to the actual dissipation rate in the flow. Note that this use of eddy diffusivity can be thought of as "overlapping" with the eddy diffusivity used in the LES transport equations. The overall effect of the eddy diffusivity is to provide a smooth transition between strong differential diffusion effects when L is small (compared to the turbulence scales) and negligible differential diffusion as L becomes large.

Although a precise determination of the eddy diffusivity is not necessary, some reasonable method is needed to estimate the relative importance of differential diffusion in a given situation. One approach is to express the eddy diffusivity in terms of a mixing length model, $\rho\alpha_t \propto \rho q L$, where q is a turbulent velocity scale and L is the flamelet domain length, and to further assume that as the domain length

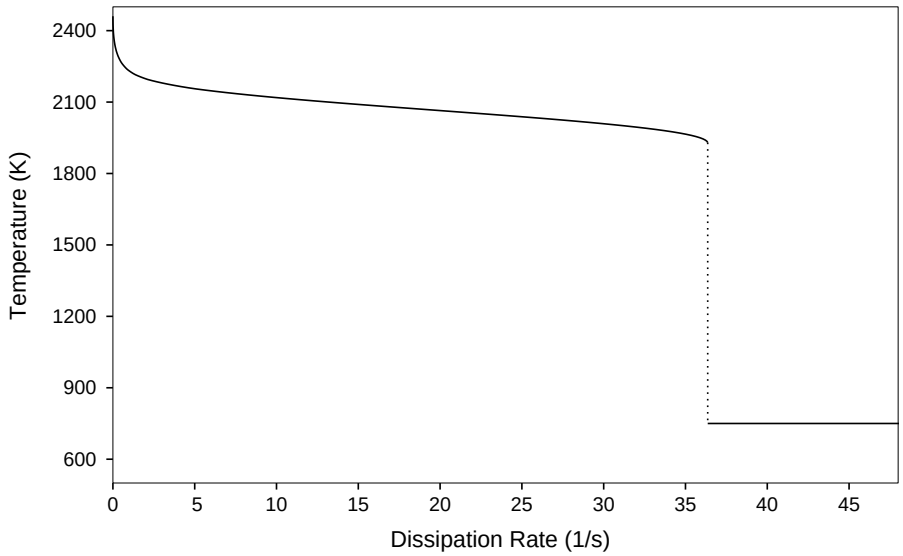

Fig. 3.4 Locus of maximum flame temperatures in the steady flamelet library. Note the discontinuous jump between burning and extinguished solutions at the critical point. Methane-air combustion at the conditions of the experiment in §5.1 (750K air, 300K fuel, 3.8 atm).

changes, ρq remains more or less constant, so that $\rho\alpha_t \propto L$. This may be expressed in a normalized form by,

$$\frac{\rho\alpha_t}{\rho\alpha_m} = \frac{L}{L_0} \ . \tag{3.39}$$

Here, $\rho\alpha_m = \int_0^L \rho\alpha_Z Z_{,x}\, dx$ represents an average molecular diffusivity for the flamelet, and L_0 is a turbulence length scale that must be chosen by the user, based on an estimate of the turbulence length scales in the flow, such that when $L = L_0$, turbulent and molecular diffusion are equally important.

Extinction Limit

Another limiting case to consider is the behavior of the flamelet solutions as $\chi_0 \to \infty$ ($L \to 0$). As the dissipation rate is increased, both the mixing and reaction rates increase, while the maximum flame temperature gradually decreases, until the flame temperature becomes so low that chemical reaction rates cannot increase any further due to the effects of Arrhenius kinetics. Once this critical turning point is reached ($\chi_0 = \chi_{\rm crit}$), further increase in χ_0 will cause the flame to extinguish. Although the behavior of diffusion flames close to extinction is inherently unsteady because

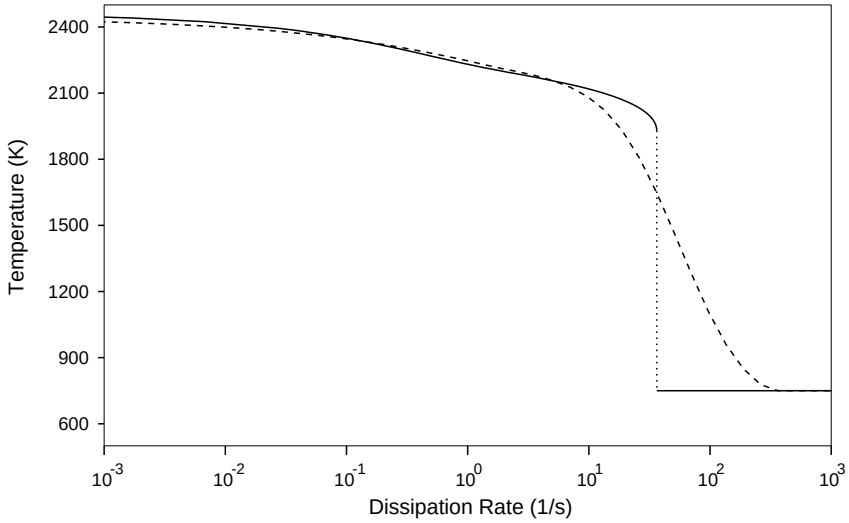

Fig. 3.5 Effect of the log-normal distribution on the flamelet library. ——: maximum temperature locus of the original steady flamelet solutions; – – –: after integration with the log-normal distribution. Methane-air combustion at the conditions of the experiment in §5.1 (750K air, 300K fuel, 3.8 atm).

of the enormous sensitivity of the steady solutions to small changes in mixing rate near the critical point, extinction can be represented with steady flamelets by introducing a discontinuous switch between steady burning solutions when $\chi_0 < \chi_{\text{crit}}$ and the steady extinguished solution for $\chi_0 > \chi_{\text{crit}}$ (Fig. 3.4). However, this description of extinction is rather crude, as exposure of a combustion simulation to the "naked" discontinuity in Fig. 3.4 can lead to unphysical results and numerical instability. Only when the flamelet library is filtered with the log-normal distribution (Fig. 3.5, discussed below) can reasonable behavior be obtained near extinction with the steady flamelet model. As alluded to at the beginning of this section, the flamelet/progress-variable approach overcomes this limitation by reparameterizing the flamelet library in terms of a chemical progress variable, which provides an unsteady, dynamic response to changes in dissipation rate.

Steady Flamelets in LES

The final step in the steady flamelet model for LES is to develop expressions for the filtered chemical variables. The steady flamelet solutions are regarded as providing a map of instantaneous chemical variables to instantaneous mixture fraction. To

account for subgrid fluctuations in mixture fraction and dissipation rate, filtered combustion variables are obtained by integrating (3.37) over the joint PDF of subgrid Z and χ_0 fluctuations. For example,

$$\widetilde{y}_i = \int y_i(Z,\chi_0)\widetilde{P}(Z,\chi_0)\,dZ\,d\chi_0 \ . \tag{3.40}$$

The joint PDF is modeled by first assuming that Z and χ_0 are independent,

$$\widetilde{P}(Z,\chi_0) = \widetilde{P}(Z)\widetilde{P}(\chi_0) \ . \tag{3.41}$$

Then, $\widetilde{P}(Z)$ is modeled using the assumed beta PDF of §3.2.4, while $\widetilde{P}(\chi_0)$ is modeled by another type of assumed PDF, the one-parameter log-normal distribution,

$$\widetilde{P}(\chi_0) = \text{LogNormal}(\chi_0;\, \widetilde{\chi},\ 1) \ , \tag{3.42}$$

where,

$$\text{LogNormal}(x;\,\mu,\sigma) = \frac{1}{x\sigma\sqrt{2\pi}}\,\exp\frac{-[\ln(x)-\mu]^2}{2\sigma^2} \ . \tag{3.43}$$

The distribution mean and variance are related to the parameters μ and σ by,

$$\overline{x} = e^{\mu+\frac{1}{2}\sigma^2} \ , \qquad \overline{x'^2} = \overline{x}^2(e^{\sigma^2}-1) \ .$$

The log-normal distribution has been found in numerical experiments to provide an accurate description of gradient magnitude and dissipation rate fluctuations of conserved scalars in fully developed turbulence (Jiménez *et al.* 1997), although the most appropriate value for σ is still an open question. For the present study a value of $\sigma = 1$ was chosen. Figure 3.5 shows the filtering effect of the log-normal distribution on the flamelet library.

Once the flamelet library is computed and assumed PDF integrals are evaluated, lookup tables can be generated to provide the filtered chemical variables as functions of the quantities readily available from LES (namely, $\widetilde{Z}$, $\widetilde{Z''^2}$, and $\widetilde{\chi}$):

$$\widetilde{y}_i = \widetilde{y}_i(\widetilde{Z},\widetilde{Z''^2},\widetilde{\chi}) \ , \quad \widetilde{T} = \widetilde{T}(\widetilde{Z},\widetilde{Z''^2},\widetilde{\chi}) \ , \quad \overline{\rho} = \overline{\rho}(\widetilde{Z},\widetilde{Z''^2},\widetilde{\chi}) \ , \quad \textit{etc.} \tag{3.44}$$

Note that (3.44) includes similar expressions for filtered transport properties such as $\overline{\mu}$ and $\widetilde{\alpha}_Z$, which are used in solving the large-scale momentum and scalar transport equations. The computational cost of the steady flamelet model is very modest, because the functions in (3.44) can be precomputed and tabulated prior to running a simulation.

3.3.4 The Flamelet/Progress-Variable Approach

The philosophy underlying the chemical models developed in this work is that the most effective description of turbulent combustion will map the details of the multi-component diffusion-reaction processes to a minimum set of transported "tracking" scalars. Extensive discussion of the mixture fraction's role as a tracking scalar was given in §3.3.1. There it was also pointed out that a model based on mixture fraction alone is incomplete, because mixture fraction does not contain any intrinsic information about chemical reactions and cannot account for chemical variations in directions perpendicular to its gradient. At least one additional scalar is needed, and since mixture fraction accounts for transport of conserved scalars, additional tracking scalars must be *nonconserved* in order to be independent from mixture fraction. A nonconserved tracking scalar is best characterized as a reaction progress variable.

Model Derivation

In the present work, addition of a single progress variable, generically denoted by C, is considered. The set of scalar transport equations carried in a simulation is then given by,

$$\begin{cases} \dfrac{\partial \rho Z}{\partial t} + \nabla \cdot (\rho \boldsymbol{u} Z) = \nabla \cdot (\rho \alpha_Z \nabla Z) \ , \\ \\ \dfrac{\partial \rho C}{\partial t} + \nabla \cdot (\rho \boldsymbol{u} C) = \nabla \cdot (\rho \alpha_C \nabla C) + \rho w_C \ . \end{cases} \tag{3.45}$$

Complete chemical state information is to be derived from Z and C through chemical state relationships of the form,

$$y_i = y_i(Z, C) \ , \qquad T = T(Z, C) \ , \qquad \rho = \rho(Z, C) \ . \tag{3.46}$$

In particular, the chemical source for the progress variable, which is a function of the chemical state, will be given by $w_C = w_C(Z, C)$. The remaining question is how to determine the best chemical state relationships for a given case. A very simple approach, developed for the present study and discussed below, is to use the steady flamelet state relationships (3.37) of §3.3.3.

Consider a computational experiment, in which a reacting flow is simulated using the steady flamelet model of §3.3.3. However, suppose that in addition to mixture fraction, a transport equation is solved for one of the chemical species, with the reaction source term for the species calculated from the chemical states predicted by the steady flamelet model. This situation leads naturally to the following questions: Would the species concentrations obtained by solving the additional transport equation be any different from those predicted by the steady flamelet model alone? And if the transport equation solution were more accurate than the steady flamelet prediction, could it not be used to constrain or parameterize the steady flamelet model? To be more specific, suppose that the transported species in question is actually the previously introduced progress variable. Then, the set of transport equations being solved is given in (3.45), while the steady flamelet model (3.37) predicts,

$$C = C(Z, \chi_0) \ , \tag{3.47}$$

giving us two independent equations for the progress variable. If (3.47) is to be consistent with (3.45), χ_0 can no longer be coupled directly to the local dissipation rate in the flow, but instead must be constrained by (3.47). Provided that the progress variable varies monotonically with χ_0, (3.47) can be inverted to obtain,

$$\chi_0 = \chi_0(Z, C) \ . \tag{3.48}$$

Substituting this into (3.37) yields (3.46).

Unsteady Flamelet Interpretation

The flamelet/progress-variable approach can alternatively be derived by interpreting it as a type of *unsteady* flamelet model. Since the dissipation rate parameter, χ_0, is determined in (3.48) by the value of the progress variable and does not have any direct relationship to the actual dissipation rate in the flow, it should not be regarded as representing a real dissipation rate but rather a ficticious one, which we denote by χ'. Thus, the flamelet equations used in the flamelet/progress-variable approach are given by

$$\rho\chi' \frac{d^2 y_i}{dZ^2} = -\rho w_i \ , \tag{3.49}$$

where $\chi' = \chi'(Z, C)$ and in general, $\chi' \neq \chi$. If we now add and subtract the term $\chi(d^2y_i/dZ^2)$ in (3.49), it can be written in the form,

$$\rho(\chi - \chi')\frac{d^2y_i}{dZ^2} = \rho\chi\frac{d^2y_i}{dZ^2} + \rho w_i \ . \tag{3.50}$$

Meanwhile, the unsteady flamelet equations (Peters 1984) are given by:

$$\rho\frac{\partial y_i}{\partial t} = \rho\chi\frac{\partial^2 y_i}{\partial Z^2} + \rho w_i \ . \tag{3.51}$$

Comparing (3.50) with (3.51), it is apparent that the left-hand side of (3.50) can be interpreted as a type of unsteady term in the flamelet equations:

$$\rho\frac{\partial y_i}{\partial t} \approx \rho(\chi - \chi')\frac{d^2y_i}{dZ^2} \ , \tag{3.52}$$

where the difference between the actual and ficticious dissipation rates indicates the degree of unsteadiness. This form for the unsteady term appears as a relaxation mechanism, evolving the flamelet solution ever closer to the steady flamelet solution for the given dissipation rate, χ. In this sense, χ' can be thought of as a lagging dissipation rate containing the memory of the flame structure from an earlier time when χ and χ' were equal. This concept, of a ficticious dissipation rate that represents the history of the evolution of the flamelet, is similar to the "equivalent" strain rate of Cuenot *et al.* (2000). It should be noted that the unsteady evolution suggested by (3.52) is actually embedded in the progress-variable transport equation, where the reaction and dissipation rates directly affect the evolution of the progress variable in a manner similar to (3.51).

Application to LES

So far, the derivation of the flamelet/progress-variable approach has been in terms of fully resolved, instantaneous quantities without consideration of subgrid turbulence modeling. This is to separate the assumptions involved in the chemistry model from those used in the turbulence model. When written in terms of filtered LES quantities, (3.45) becomes,

$$\begin{cases} \dfrac{\partial\overline{\rho}\widetilde{Z}}{\partial t} + \nabla\cdot(\overline{\rho}\widetilde{\boldsymbol{u}}\widetilde{Z}) = \nabla\cdot[\overline{\rho}(\widetilde{\alpha}_Z + \alpha_t)\nabla\widetilde{Z}] \ , \\ \\ \dfrac{\partial\overline{\rho}\widetilde{C}}{\partial t} + \nabla\cdot(\overline{\rho}\widetilde{\boldsymbol{u}}\widetilde{C}) = \nabla\cdot[\overline{\rho}(\widetilde{\alpha}_C + \alpha_t)\nabla\widetilde{C}] + \overline{\rho}\widetilde{w}_C \ , \end{cases} \tag{3.53}$$

where α_t is the turbulent diffusivity of §3.2.2. To account for subgrid fluctuations in the mixture fraction and progress variable, filtered combustion variables are obtained by integrating (3.46) over the joint PDF of Z and C. For example,

$$\widetilde{y}_i = \int y_i(Z,C)\widetilde{P}(Z,C)\,dZ\,dC \ , \tag{3.54}$$

and,

$$\widetilde{w}_C = \int w_C(Z,C)\widetilde{P}(Z,C)\,dZ\,dC \ . \tag{3.55}$$

The joint PDF is modeled by first writing,

$$\widetilde{P}(Z,C) = \widetilde{P}(C|Z)\widetilde{P}(Z) \ , \tag{3.56}$$

where $\widetilde{P}(Z)$ is given by the assumed beta PDF of §3.2.4. The conditional PDF, $\widetilde{P}(C|Z)$, is modeled by assuming that each subgrid chemical state is represented by a single flamelet solution. Mathematically this is described by a delta function,

$$\widetilde{P}(C|Z) = \delta(C - \widetilde{C|Z}) \ , \tag{3.57}$$

where the conditional mean, $\widetilde{C|Z}$, is given by one of the steady flamelet solutions in (3.37),

$$\widetilde{C|Z} = C(Z,\chi_0) \ , \tag{3.58}$$

and χ_0 is chosen such that the constraint,

$$\widetilde{C} = \int C(Z,\chi_0)\widetilde{P}(Z)\,dZ \ , \tag{3.59}$$

analogous to (3.47), is satisfied. The flamelet/progress-variable approach could benefit from a more sophisticated model for $\widetilde{P}(C|Z)$, but as noted in §3.2.4, assumed PDF modeling of reacting scalars needs to be further researched.

The implementation of the flamelet/progress-variable approach is similar to the steady flamelet model in that it employs chemical state relationships determined by a flamelet library and uses assumed PDF's to represent subgrid fluctuations. The major difference, of course, is the parameterization by a progress variable instead

of dissipation rate. Once the flamelet library is computed and assumed PDF integrals are evaluated, lookup tables can be generated to provide the filtered chemical variables as functions of the quantities readily available from LES (namely, $\widetilde{Z}$, $\widetilde{Z''^2}$, and $\widetilde{C}$):

$$\widetilde{y}_i = \widetilde{y}_i(\widetilde{Z}, \widetilde{Z''^2}, \widetilde{C}) \ , \quad \widetilde{T} = \widetilde{T}(\widetilde{Z}, \widetilde{Z''^2}, \widetilde{C}) \ , \quad \overline{\rho} = \overline{\rho}(\widetilde{Z}, \widetilde{Z''^2}, \widetilde{C}) \ , \quad etc. \tag{3.60}$$

Note that (3.60) includes similar expressions for $\overline{\mu}$, $\widetilde{\alpha}_Z$, $\widetilde{\alpha}_C$, and $\widetilde{w}_C$, which are used in solving the large-scale momentum and scalar transport equations. The computational cost of the flamelet/progress-variable approach is only marginally greater than the steady flamelet model, because the functions in (3.60) can be precomputed and tabulated prior to running a simulation. The major additional cost comes from solving the transport equation for the progress variable.

Further Discussion

One of the more conspicuous limitations of the steady flamelet model (§3.3.3) is its inability to properly account for ignition and extinction phenomena. This is exemplified most clearly by the discontinuous jump in flame states in Fig. 3.4, which indicates that the steady flamelet library is somehow incomplete because it cannot represent any of the "partially extinguished" intermediate states that should fill the gap between the critical point and complete extinction. In fact, the steady flamelet equations do provide a complete and continuous set of solutions ranging from chemical equilibrium to complete extinction, but they are not in general uniquely parameterized by the dissipation rate.

The complete locus of solutions to the steady flamelet equations is shown in Fig. 3.6. The shape of this curve, sometimes called the "S-shaped curve" in diffusion flame theory, is determined primarily by the chemical kinetics. With Arrhenius kinetics, there are typically three solution branches: (1) the steady burning branch, (2) the unstable branch of partially extinguished states, and (3) the complete extinction line. On the stable burning branch, maximum flame temperature decreases with increasing dissipation rate as more rapid mixing increases reactant concentrations while diluting product concentrations. When the critical point is reached,

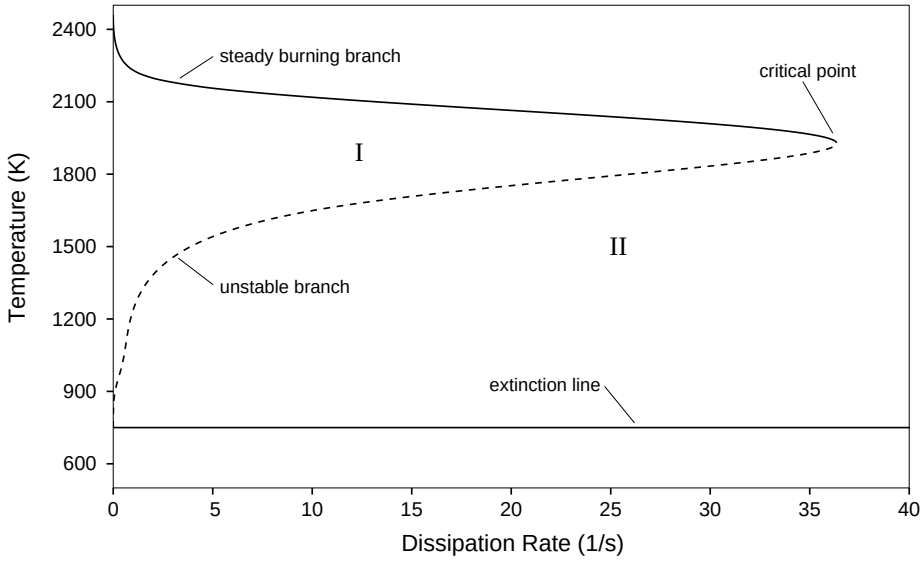

Fig. 3.6 Locus of maximum flame temperatures from a complete set of steady flamelet solutions including the unstable branch. This should be compared with Fig. 3.4.

the flame temperature becomes so low that Arrhenius rate factors in the chemical kinetics begin to limit reaction rates, even as reactant concentrations continue to increase. Below the critical point on the unstable branch, dissipation rate must decrease with decreasing flame temperature in order to keep mixing in balance with lower reaction rates at colder temperatures. On the complete extinction line, the effect of chemical kinetics is negligible so that the chemical state is independent of dissipation rate.

Because the defining characteristic of steady flamelet solutions is that chemical reaction rates are in balance with molecular diffusion rates, dissipation rate can be thought of as synonymous with an overall reaction rate when considering the structure of the locus of steady flamelet solutions. In this case, the significance of the curve is more easily seen with dissipation rate plotted on the vertical axis as the dependent variable. This view is depicted in Fig. 3.7, where dissipation rate is plotted versus maximum flame temperature. At the coldest temperatures on the left side of the figure, reaction rates are negligible. As the flame temperature rises, reaction rates steadily increase, until reactants become scarce enough that they

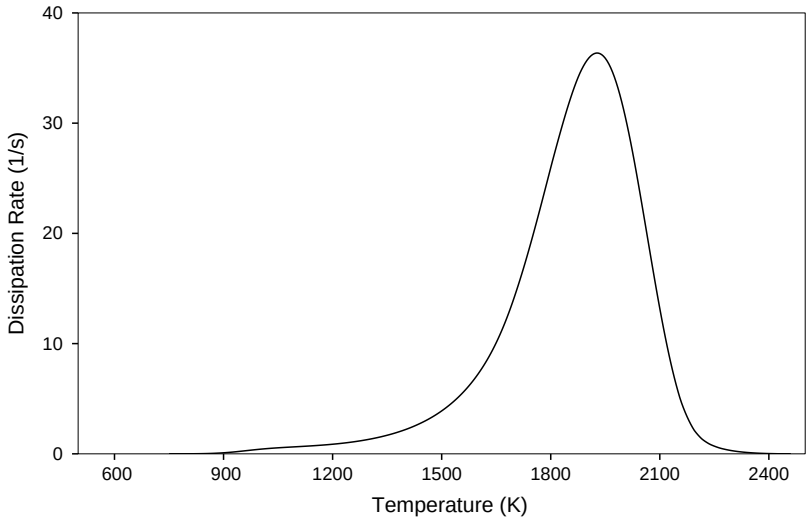

Fig. 3.7 Locus of maximum flame temperatures viewed as reaction rate versus temperature.

begin to limit reaction rates. Beyond this point, reaction rates steadily decrease as the chemical state approaches equilibrium on the right side of the figure.

The use of the unstable branch of steady flamelet solutions in the progress variable approach has been criticized as unphysical, but as we now demonstrate, the behavior of the model in this region is very similar to that of an unsteady flamelet solution. For a given maximum flame temperature on the vertical axis of Fig. 3.6, the ficticious dissipation rate, χ', corresponds to a point on the curve, while the actual dissipation rate, χ, will correspond to a location either in region I or in region II, depending on whether $\chi < \chi'$ or $\chi > \chi'$, respectively. Referring to (3.52) and noting that d^2T/dZ^2 is negative in the region where temperature is maximum, we see that in region I, the unsteady term is positive,

$$\frac{\partial T}{\partial t} \approx (\chi - \chi')\frac{d^2T}{dZ^2} > 0 \quad \text{in region I} ,$$

so that the flame state moves up to the steady burning solution branch, while in region II, the unsteady term is negative,

$$\frac{\partial T}{\partial t} \approx (\chi - \chi')\frac{d^2T}{dZ^2} < 0 \quad \text{in region II} ,$$

so that the flame state moves down to the steady extinguished solution branch (or down to the steady burning branch if it is initially above it). Thus, the unstable

solution branch is important both physically and in the progress-variable approach because it delineates the border between regions I and II, between ignition and extinction of the flame.

The last issue we consider is the definition of the progress variable. For a one-step chemical mechanism, there is only a single degree of freedom remaining after mixture fraction is known, so that any species, be it fuel, oxidizer, or product, uniquely determines the others and can be chosen to serve as the progress variable. In fact, the progress-variable approach provides an exact description of one-step chemical systems. But for a large, multistep chemical system, the selection of the progress variable should be guided by the two following criteria: (1) the progress variable should be an important, controlling quantity that contains the essential features of the process it is supposed to represent, and (2) it should provide a unique mapping of all of the chemical states in the flamelet library. The dissipation rate is an example of a quantity that clearly does not uniquely determine chemical states (Fig. 3.6). Similarly, intermediate species that are produced and later consumed are not expected to be useful indicators of reaction progress. Since the final result of chemical reactions is to transform reactants into products, a good measure of how far the transformation has progressed is the product mass fraction. In the present study, the progress variable defined by $C = y_{\mathrm{P}} = y_{\mathrm{CO_2}} + y_{\mathrm{H_2O}}$ is used for the case of methane-air combustion. However, product mass fraction does not necessarily satisfy the second criterion of providing a unique mapping of all the states. For methane-air combustion, there is a significant region of nonuniqueness in fuel-rich mixtures close to equilibrium, similar to what is seen in the temperature in Fig. 3.3. In practice, the solution to this problem is to use a "truncated" flamelet library, in which the nonunique, near-equilibrium states are removed. Unfortunately, this approximation may break down in regions where hot products mix with unburned fuel and may explain the discrepancy in the carbon monoxide prediction in Fig. 5.9. In general, the only chemical property that is guaranteed to vary monotonically during chemical reactions is the entropy, and so this would be a logical choice for the progress variable. However, entropy is governed by a significantly more

complicated equation than (3.45) and includes source terms for both mixing and chemical reaction. Nevertheless, future studies using a progress-variable approach should consider using entropy as the progress variable.

Chapter 4

NUMERICAL METHODS

One of the main objectives of this work was the development of special numerics for large eddy simulation of variable-density flows with heat release. Typical numerical methods used in computational fluid dynamics are usually not suitable for LES because they do not consider the important issue of nonlinear stability. This chapter discusses a staggered space-time, conservative discretization for the variable-density transport equations, as well as an efficient, semi-implicit iterative technique for integrating those equations. Details of the implementation in cylindrical coordinates and the specification of boundary conditions are also considered.

4.1 Conservative Space-Time Discretization

Large eddy simulations are more vulnerable to numerical errors than most other types of numerical computation (such as direct numerical simulations) because practical calculations are always under-resolved. While subgrid-scale models may account for the effects of unresolved physical scales, they should not be expected to compensate for numerical errors. Consequently, practical large eddy simulations can "blow up" when aliasing or other errors contaminate the solution. The typical remedy is to incorporate some form of artificial dissipation (such as upwind biased schemes or explicit filtering techniques) to damp instabilities and other numerical errors. Unfortunately, this approach usually leads to the unwanted damping of physical processes as well as numerical errors, especially when a broadband range of nonlinearly interacting scales is simulated. Even if artificial dissipation is carefully confined to the smallest scales, larger scales will still be indirectly affected through nonlinear interactions. Fortunately, stability can be achieved without artificial damping by designing numerical schemes to satisfy certain conservation requirements.

4.1.1 The Role of Conservation

Consider the Eulerian transport equation for a conserved quantity η,

$$\frac{\partial \rho\eta}{\partial t} + \nabla \cdot (\rho \boldsymbol{u}\eta) = 0 \ , \tag{4.1}$$

and the continutity equation (obtained with $\eta = 1$),

$$\frac{\partial \rho}{\partial t} + \nabla \cdot (\rho \boldsymbol{u}) = 0 \ . \tag{4.2}$$

These equations directly express the (primary) conservation of η and of mass, but together, they also imply conservation of any function, $f(\eta)$:

$$\frac{\partial \rho f(\eta)}{\partial t} + \nabla \cdot [\rho \boldsymbol{u} f(\eta)] = 0 \ . \tag{4.3}$$

In particular, the function $f(\eta) = \frac{1}{2}\eta^2$ or "η-energy" is also conserved. This is refered to as *secondary* conservation. From the point of view of numerical methods, secondary conservation is what guarantees nonlinear stability.

Because the continuity equation for variable-density flows contains a time derivative term, one needs to consider both temporal and spatial discretizations when developing conservative schemes. That is, the temporal and spatial derivatives in the material convection terms must be discretized in a specific relation to each other and to the time-dependent continuity equation. This is clear from the steps required to derive (4.3) from (4.1) and (4.2). In the following sections, discrete analogs of the product rule of differentiation in calculus will be used to show how both primary and secondary conservation can be achieved in the discrete equations.

4.1.2 Index-Free Notation

Before presenting the discrete equations, we introduce a compact and convenient notation for writing discretized equations in a form similar to the original partial differential equations (Piacsek and Williams 1970; Morinishi *et al.* 1998). This notation is also very useful for performing algebraic manipulations on the equations.

Second-order discretizations usually involve the primitive operations of interpolation and differencing in a particular coordinate direction. For any pair of coordinate directions x and y having uniform grids with respective spacings Δx and Δy and respective grid indices i and j, we define the interpolation operators,

$$\overline{u}^x\Big|_{i,j} = \frac{u_{i+1/2,j} + u_{i-1/2,j}}{2} \ , \qquad \overline{u}^y\Big|_{i,j} = \frac{u_{i,j+1/2} + u_{i,j-1/2}}{2} \ , \tag{4.4}$$

and the differencing operators,

$$\delta_x(u)\Big|_{i,j} = \frac{u_{i+1/2,j} - u_{i-1/2,j}}{\Delta x} \ , \qquad \delta_y(u)\Big|_{i,j} = \frac{u_{i,j+1/2} - u_{i,j-1/2}}{\Delta y} \ . \tag{4.5}$$

Note that each of the operators in (4.4) and (4.5) produces a result that is staggered with respect to the operand in the coordinate direction indicated. For example, $\overline{u}^x$ is shifted $\frac{1}{2}\Delta x$ with respect to u in the x direction. We also define the following nonlinear interpolation operator:

$$\widetilde{uv}^x = 2\overline{u}^x\overline{v}^x - \overline{uv}^x \ , \tag{4.6}$$

which will be used in the expressions of secondary conservation.

There are a number of discrete identities, easily proved by substitution of the above definitions, which will be useful later:

$$\delta_x(a\overline{b}^x) = \overline{a\delta_x(b)}^x + b\,\delta_x(a) \ , \tag{4.7}$$

$$\delta_x(ab) = \overline{a}^x\delta_x(b) + \overline{b}^x\delta_x(a) \ , \tag{4.8}$$

$$\delta_x(\overline{a}^y) = \overline{\delta_x(a)}^y \ , \tag{4.9}$$

$$\overline{\overline{a}^x}^y = \overline{\overline{a}^y}^x \ . \tag{4.10}$$

Here, a and b are any two compatible quantities and x and y are any two coordinate directions. Two quantities are compatible if the locations at which they are defined have the proper relationship for the expression to make sense. All terms that multiply or add in a given expression must be defined on the same set of grid points (not staggered with respect to one another). For example, the product

$u\overline{v}^x$ can only make sense if v is staggered with respect to u in the x direction so that $\overline{v}^x$ is collocated with u. The first two identities (4.7) and (4.8) are in the form of the product rule in calculus, creating a discrete calculus that enables manipulations to be performed on the discrete equations in analogy with the original partial differential equations.

4.1.3 Fully Discrete Equations

In the present work, velocity components are *staggered* with respect to density and other scalars in both space and time (Harlow and Welch 1965). The space-time mesh is composed of continuity "cells" around which the density and velocity are placed in their natural positions based on their respective roles in the continuity equation (Fig. 4.1). All other scalar variables, such as pressure and mixture fraction, are collocated with the density. By convention, variables defined on cell faces oriented in a positive coordinate direction are assigned the same indices as the cell. Time advancing from u^n and ρ^n to u^{n+1} and ρ^{n+1} completes the continuity cells in the upper row in the figure.

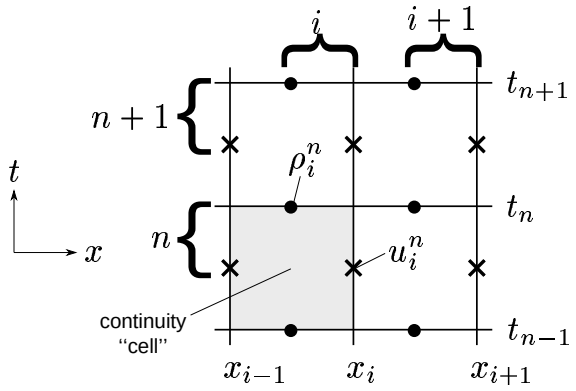

Fig. 4.1 A staggered space-time grid.

The mass flux (or momentum per unit volume), which plays an important role in the descretization of the continuity equation and convective derivatives, is given the symbol g_i. The conversion between u_i and g_i is accomplished using the following relations:

$$g_i = \overline{\overline{\rho}^{x_i}}^t u_i \ , \qquad u_i = g_i \big/ \overline{\overline{\rho}^{x_i}}^t \ . \tag{4.11}$$

In direct analogy with (2.20–2.22), we now present the fully discrete equations. Note that interpolation operators (overbars with superscripts) do not follow the summation convention.

Continuity:

$$\delta_t(\rho) + \delta_{x_j}(g_j) = 0 \tag{4.12}$$

Momentum:

$$\delta_t(g_i) + \delta_{x_j}(\overline{\overline{g_j}^{x_i}}^t \overline{\overline{u_i}^{x_j}}^t) = -\delta_{x_i}(p) + \delta_{x_j}(\tau_{ij}) \tag{4.13}$$

$$\tau_{ij} = \begin{cases} \overline{\overline{\mu}^{x_i}}^{x_j} \left[\delta_{x_j}(\overline{u_i}^t) + \delta_{x_i}(\overline{u_j}^t)\right] & i \neq j \\ 2\mu[\delta_{x_j}(\overline{u_i}^t) - \frac{1}{3}\delta_{x_k}(\overline{u_k}^t)\delta_{ij}] & i = j \end{cases}$$

Scalar Transport:

$$\delta_t(\rho\phi) + \delta_{x_j}(g_j \overline{\overline{\phi}^{x_j}}^t) = \delta_{x_j}\left[\overline{\overline{\rho\alpha}^{x_j}}^t \delta_{x_j}(\overline{\phi}^t)\right] + \overline{\rho}^t w(\overline{\phi}^t) \ . \tag{4.14}$$

For clarity we have dropped the scalar index k from the scalar transport equation. The above compact notation can be expanded into more conventional form. For example, the continuity equation in two dimensions for the cell above the shaded one in Fig. 4.1 would be expanded as,

$$\begin{aligned} \frac{\rho_{i,j}^{n+1} - \rho_{i,j}^n}{\Delta t} + \frac{1}{4\Delta x}\Big[&(\rho_{i+1,j}^{n+1} + \rho_{i,j}^{n+1} + \rho_{i+1,j}^n + \rho_{i,j}^n)u_{i,j}^{n+1} \\ &- (\rho_{i,j}^{n+1} + \rho_{i-1,j}^{n+1} + \rho_{i,j}^n + \rho_{i-1,j}^n)u_{i-1,j}^{n+1}\Big] \\ + \frac{1}{4\Delta y}\Big[&(\rho_{i,j+1}^{n+1} + \rho_{i,j}^{n+1} + \rho_{i,j+1}^n + \rho_{i,j}^n)v_{i,j}^{n+1} \\ &- (\rho_{i,j}^{n+1} + \rho_{i,j-1}^{n+1} + \rho_{i,j}^n + \rho_{i,j-1}^n)v_{i,j-1}^{n+1}\Big] = 0 \ . \end{aligned}$$

When the above equations are generalized for nonuniform (stretched) grids, the interpolation and differencing operators are defined as,

$$\overline{u}^x\Big|_{i+1/2} = c_i u_{i+1} + (1 - c_i)u_i \ , \qquad \delta_x(u)\Big|_{i+1/2} = \frac{u_{i+1} - u_i}{x_{i+1} - x_i} \ , \tag{4.15}$$

where c_i are linear interpolation weights. These definitions maintain formal second-order accuracy of the interpolation operator, but they do not satisfy the discrete product rules exactly so that secondary conservation is only approximately satisfied. In practice, the simulations are found to be stable on sufficiently smooth grids. A more robust, but possibly less accurate, approach would be to continue using equal weighted interpolations.

4.1.4 Benefits of Staggering

The major benefit of staggering the velocity in space and time is the improved accuracy and stability of the continuity equation that results from using central differences based on a stencil width of only Δ (instead of the usual 2Δ) for the time-derivative of density and the spatial derivatives of velocity in (4.12). The modified wavenumber diagrams (*cf.* Moin 2001, p. 16) for the staggered and non-staggered cases are compared in Fig. 4.2. The pressure gradient in the momentum equation is likewise improved because the velocity components are collocated with the corresponding pressure derivatives.

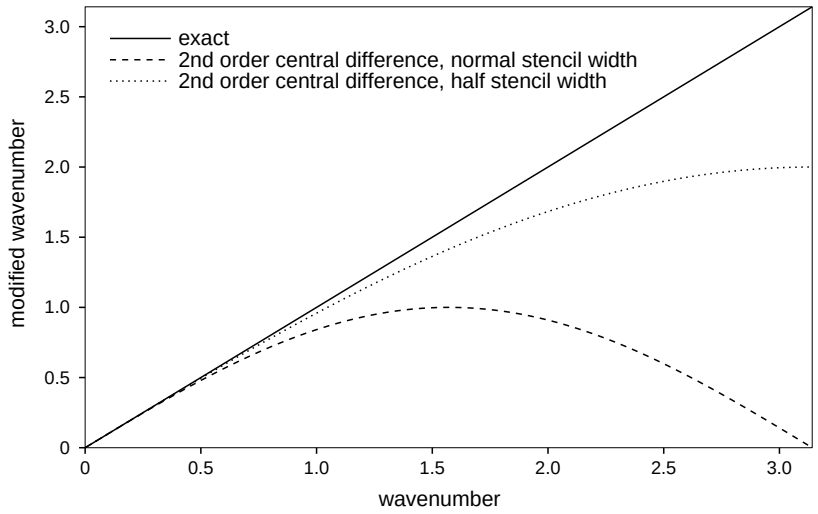

Fig. 4.2 Modified wavenumber diagram for second order central differences based on stencil widths of 2Δ and Δ.

However, staggered grids do not improve the accuracy of the first derivatives in convection terms, such as those in the momentum and scalar transport equations, because of the extra interpolation required to compute a derivative at the same location as the variable. For a linear first derivative term, this amounts to

$$\overline{\delta_x(u)}^x\Big|_i = \delta_x(\overline{u}^x)\Big|_i = \frac{u_{i+1} - u_{i-1}}{2\Delta x} \ ,$$

which is the standard second-order central difference expression. Thus, the velocity and scalars are still susceptible to the formation of "wiggles" due to the extreme

dispersion error at high-wavenumbers (Fig. 4.2). However, because of the constraining effect of the continuity equation, staggered-grid velocity solutions are typically less susceptible to the wiggle problem than scalars.

Second derivatives on a staggered grid can be accurately expressed in terms of repeated application of the first derivative operator,

$$\delta_x[\delta_x(p)]\Big|_i = \frac{p_{i+1} - 2p_i + p_{i-1}}{(\Delta x)^2} \ .$$

This allows, for example, a discretely consistent Poisson equation for pressure to be derived by applying the discrete divergence operator to the discrete momentum equation. Attempts to perform the same operation on non-staggered grids lead to the well-known even-odd decoupling problem.

4.1.5 Discrete Conservation Properties

Using the identities, (4.7–4.10), the discrete equations can be manipulated to show their conservation properties. Using the discrete product rules (4.7) and (4.8), the left-hand sides of (4.13) and (4.14) can be expanded to the following equivalent forms:

$$\overline{\overline{\rho}^{x_i}}^t \delta_t(u_i) + \overline{\overline{g_j}^{x_i}}^t \delta_{x_j}(\overline{u_i}^t)^{x_j} + \overline{u_i}^t \left[\delta_t(\overline{\rho}^{x_i}{}^t) + \delta_{x_j}(\overline{g_j}^{x_i}{}^t)\right] = \cdots \ , \tag{4.16}$$

$$\overline{\rho}^t \delta_t(\phi) + \overline{g_j \delta_{x_j}(\overline{\phi}^t)}^{x_j} + \overline{\phi}^t \left[\delta_t(\rho) + \delta_{x_j}(g_j)\right] = \cdots \ . \tag{4.17}$$

The right most group of terms in brackets in each equation will be zero if the continuity equation (4.12) is satisfied. What remains is the "advective form" of the left-hand sides of the momentum and scalar transport equations. Multiplying (4.17) by $\overline{\phi}^t$ and rearranging with help from the identities, one can derive a discrete equation for the "scalar energy":

$$\begin{aligned} &\delta_t(\tfrac{1}{2}\rho\phi^2) + \delta_{x_j}\left(g_j \tfrac{1}{2} \widetilde{\overline{\phi}^t \overline{\phi}^t}^{x_j}\right) \\ &\quad + \tfrac{1}{2}\overline{\phi}^t\overline{\phi}^t \left[\delta_t(\rho) + \delta_{x_j}(g_j)\right] + \tfrac{1}{2}\left(\overline{\phi}^t\overline{\phi}^t - \overline{\phi^2}^t\right)\delta_t(\rho) = \cdots \ . \end{aligned} \tag{4.18}$$

A similar equation can be derived for each component of the kinetic energy (there is no implied summation over the index i):

$$\begin{aligned}\delta_t(\tfrac{1}{2}\overline{\overline{\rho}^{x_i}}^t u_i^2) + \delta_{x_j}\left(\overline{\overline{g_j}^{x_i}}^t \tfrac{1}{2}\,\widetilde{\overline{u_i}^t \overline{u_i}^t}^{x_j}\right) \\ + \tfrac{1}{2}\,\overline{u_i}^t \overline{u_i}^t\left[\delta_t(\overline{\overline{\rho}^{x_i}}^t) + \delta_{x_j}(\overline{\overline{g_j}^{x_i}}^t)\right] + \tfrac{1}{2}\left(\overline{u_i}^t \overline{u_i}^t - \overline{u_i^2}^t\right)\delta_t(\rho) = \cdots\ .\end{aligned} \tag{4.19}$$

Exact secondary conservation cannot be achieved with the present scheme due to the presence of the last term involving $\delta_t(\rho)$ in the above equations. However, it is easy to show that this term is $O(\Delta t^{\,2})$ and numerical experiments have shown that it is not cummulative in time. Unfortunately, a discretization that obtains exact secondary conservation without giving up exact primary conservation could not be found. Note, however, that secondary conservation is exact when $\delta_t(\rho) = 0$, or equivalently $\delta_{x_j}(g_j) = 0$. This is the case for steady flows and constant density flows.

4.1.6 Spurious Heat Release

A conservative scheme for variable density flows should conserve not only total energy, but also internal and kinetic energies in the absence of energy transfers, due to pressure-dilatation work and viscous dissipation, between the two forms. Also, a consistent accounting of energy transfers is required when they do occur. However, even if numerical conservation is achieved in this regard, numerical stability is still not guaranteed because spurious conversion from internal to kinetic energy can occur, in violation of the second law of thermodynamics. Such a violation can be characterized as a *spurious heat release*. The practical consequence of this unphysical energy transfer is the unbounded growth of the kinetic energy due to the pressure-dilatation work term.

Spurious heat release is typically caused by dispersion errors in the convection terms of the scalar transport and continuity equations. Over time, these errors can cause inconsistencies to develop between changes in density due to scalar transport (via the equation of state) and changes in density due to simple convection in the continuity equation. As an example, consider the pure convection of a variable-density scalar in a divergence-free velocity field. The density determined by the

equation of state and scalar transport equations,

$$\rho = \rho(\phi) \ , \qquad \frac{D\phi}{Dt} = 0 \ ,$$

is not numerically equivalent to the density determined by the continuity equation,

$$\frac{D\rho}{Dt} = 0 \ ,$$

because of errors in the numerical approximation of the material derivative operators. Since in the low Mach number approximation, density is derived from the equation of state while the continuity equation acts as a constraint on the velocity, the inconsistency manifests itself as a spurious divergence of the velocity field.

Some numerical schemes that deal with this problem were investigated by Nicoud (2000). A physically based remedy would be to restore some of the compressibility effects to the low Mach number equations, so that a spurious divergence of the velicity field causes a decrease in internal energy that feeds back to the equation of state, thereby increasing the density and halting the divergence. This idea was not explored further in the present study; instead, the time derivative of density in the continuity equation was spatially filtered using the test-filter operator of the dynamic model (§3.2.1), *i.e.*,

$$\frac{\partial \rho}{\partial t} \longrightarrow \widehat{\delta_t(\rho)} = \frac{\widehat{\rho^{n+1} - \rho^n}}{\Delta t} \ . \tag{4.20}$$

This was found to greatly improve, but not completely guarantee, the stability of the algorithm.

4.2 Iterative Semi-Implicit Scheme

The fully discrete equations as expressed by (4.12–4.14) are fully implicit in time. While this implicitness provides much of the schemes's stability and robustness, it is preferable to adopt a semi-implicit, iterative solution procedure that is much more economical but also retains most of the stability and accuracy properties of the fully implicit scheme.

The time discretization in (4.12–4.14) is similar to the popular Crank-Nicolson or trapezoidal time-advancement scheme, but the "right-hand-sides" are evaluated using variables that have been interpolated in time to the midpoint between the solution at times t^n and t^{n+1}. In terms of a single ordinary differential equation,

$$\frac{du}{dt} = f(u) \ ,$$

the time discretization may be written as,

$$\frac{u^{n+1} - u^n}{\Delta t} = f\left[\tfrac{1}{2}(u^n + u^{n+1})\right] \ ,$$

or using the compact notation as,

$$\delta_t(u) = f(\overline{u}^t) \ . \tag{4.21}$$

Note that for linear $f(u)$, this is identical to the trapezoidal scheme. For nonlinear $f(u)$ the above implicit equation could be solved using Newton-Raphson iterations, which require the solution of systems of algebraic equations when u and f are vectors. Let u_k^{n+1} be the k^{th} iterative approximation to u^{n+1}. Then, applying Newton-Raphson to (4.21), one obtains,

$$u_{k+1}^{n+1} = u^n + \Delta t\, f\left[\tfrac{1}{2}(u^n + u_k^{n+1})\right] + \tfrac{1}{2}\,\Delta t\, \left[\frac{\partial f}{\partial u}\right](u_{k+1}^{n+1} - u_k^{n+1}) \ ,$$

with initial guess

$$u_0^{n+1} = u^n \ .$$

This can also be expressed in "delta" or residual form,

$$\left[1 - \tfrac{1}{2}\,\Delta t\, \frac{\partial f}{\partial u}\right](u_{k+1}^{n+1} - u_k^{n+1}) = u^n + \Delta t\, f\left[\tfrac{1}{2}(u^n + u_k^{n+1})\right] - u_k^{n+1} \ . \tag{4.22}$$

An explicit iterative scheme results if the Jacobian, $\partial f/\partial u$, in (4.22) is set to zero. This scheme has some interesting stability properties that depend on the number of iterations performed each time step. The linear stability properties of the explicit scheme using the linear model problem, $du/dt = \lambda u$, are shown in Fig. 4.3 for 1, 2, and 3 iterations. A minimum of two iterations are required for second order

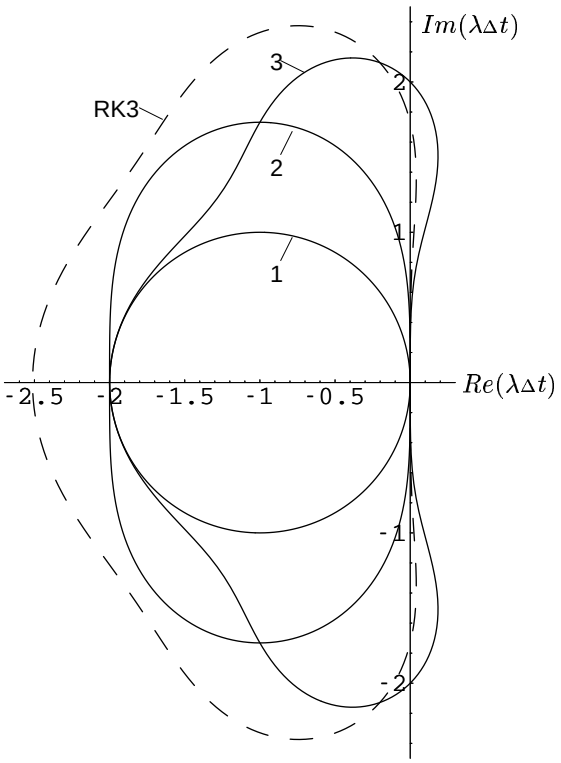

Fig. 4.3 Linear stability regions for 1, 2, and 3 iterations. Third-order Runge-Kutta is also shown for comparison.

accuracy. Additional iterations may improve stability but do not increase the order of accuracy. When three iterations are used, the method has similar imaginary-axis stability limits and comparable computational cost to the third-order Runge-Kutta method. The explicit iterations only converge for sufficiently small time steps, Δt. As the number of iterations approaches infinity, the explicit scheme converges to (4.21) inside the circle of radius $|\lambda\,\Delta t\,| = 2$ and diverges outside it. Thus, linear stability limits are not significantly increased beyond three iterations. Note that the main objective of the present iterative scheme is not to increase linear stability limits but rather, to obtain *nonlinear stability* and the conservation properties of the fully discrete equations.

Semi-implicit schemes result if the Jacobian in (4.22) is simplified (*e.g.* approximate factorization). The economy of the semi-implicit scheme derives from a judicious choice of which terms to treat implicity and which to treat explicity. Usually only the stiffest terms in each equation are treated implicity, such as derivatives

in a coordinate direction that has a much greater variation in grid spacing than the other directions. For example, where grid refinement occurs near a wall, only derivatives in the wall-normal direction would be treated implicitly. In the present study, the following terms are treated implicitly: (1) advection and diffusion in the radial direction, (2) advection and diffusion in the azimuthal direction, and (3) the pressure in all directions via a Poisson equation.

The iteration procedure employed in the present study is summarized below. In the following, the superscript n refers to solution values that are known from the previous time level, the superscript k refers to the iteration cycle between the solutions at time step n and $n+1$, the superscript 0 indicates the initial guess for the first iteration when $k = 0$, and a hat placed above a symbol is used for a provisional value of some quantity.

Step 1: Choose predictors (initial guesses) for the values of the variables at the next time level. The simplest choice is to use the solution values at the current time level:

$$u_i^0 = u_i^n \ , \qquad \phi^0 = \phi^n \ , \qquad \text{etc.}$$

This choice corresponds to using explicit Euler (or first-order Runge-Kutta) for the first iteration. Predictors are not essential to the present algorithm in that they do not affect the final converged solution, but good predictors can speed convergence of the iterations, and they can affect accuracy and stability when only a small number of iterations are used. The density predictor is particularly important because it is related to the conservation properties described in §4.1. Experience has shown that it is best to ensure that the predictors for density and velocity satisfy the continuity equation. That is, the predicted rate-of-change of density should correspond to the predicted mass flux divergence. We therefore choose:

$$\rho^0 = \rho^n - \Delta t \, \delta_{x_j}(g_j^0) \ .$$

With the predictor $g_j^0 = g_j^n$, this is equivalent to linear extrapolation in time:

$$\rho^0 = \rho^n + (\rho^n - \rho^{n-1}) = 2\rho^n - \rho^{n-1} \ .$$

Step 2: We first advance the scalar equation(s) so that a better estimate for the density can be obtained early in the iteration process. In the present work, each scalar equation is updated separately, and semi-implicit penta-diagonal equations (for the QUICK scheme discussed in §4.3) are solved for advection and diffusion in the radial and azimuthal directions (using approximate factorization) so that grid refinements in the radial direction near walls or in the azimuthal direction near the centerline do not limit the time step. Any source terms are treated explicitly. Time advancing (4.14) yields $(\rho\phi)^{k+1}$, from which a provisonal estimate for ϕ^{k+1} is obtained using the current density predictor:

$$\widehat{\phi} = (\rho\phi)^{k+1} / \rho^{k} \ .$$

Boundary conditions are enforced on $\widehat{\phi}$.

Step 3: The density is updated from the equation of state, using the provisonal scalar values:

$$\rho^{k+1} = f(\widehat{\phi}) \ .$$

Note that it may be possible in some cases to obtain ρ^{k+1} directly as a function of $(\rho\phi)^{k+1}$. However, this was found to be less accurate because $(\rho\phi)^{k+1}$ implicitly contains ρ^{k}, which is based on information from the previous iteration.

Step 4: Re-update the scalar(s) based on the new density:

$$\phi^{k+1} = (\rho\phi)^{k+1} / \rho^{k+1} \ .$$

This is required to preserve primary scalar conservation. Boundary conditions are applied to ϕ^{k+1}.

Step 5: Time advance the momentum equations (4.13) to yield provisional estimates for the mass flux components, $\widehat{g}_i$. In the present work, semi-implicit tri-diagonal equations are solved separately for each velocity component for advection and diffusion in the radial and azimuthal directions using approximate factorization. The current best estimate for pressure is included on the right-hand-side.

Provisional velocity components are computing using:

$$\widehat{u}_i = \widehat{g}_i \,/\, (\overline{\overline{\rho}^{x_i}}^t)^{k+1} \ .$$

Boundary conditions are applied to $\widehat{u}_i$.

Step 6: A Poisson equation is solved to determine the adjustment to the pressure field required to ensure that the continuity equation is satisfied. We first consider additive corrections, δg_i and δp, to the mass flux and pressure such that,

$$g_i^{k+1} = \widehat{g}_i + \delta g_i \ , \qquad p^{k+1} = p^k + \delta p \ .$$

We then substitute these expression into the momentum equations. To focus on the pressure, we group all other terms into a generic right-hand-side term, R_i,

$$\frac{\widehat{g}_i + \delta g_i - g_i^n}{\Delta t} = -\delta_{x_i}(p^k + \delta p) + R_i \ .$$

Next, we "time split" this equation into a predictor part and a corrector part:

$$\frac{\widehat{g}_i - g_i^n}{\Delta t} = -\delta_{x_i}(p^k) + R_i \ , \tag{4.23}$$

$$\delta g_i = -\,\Delta t\, \delta_{x_i}(\delta p) \ . \tag{4.24}$$

Equation (4.23) is the same as the equation that was solved in Step 5. Taking the divergence of (4.24) leads to a Poisson equation:

$$\begin{aligned} \delta_{x_k}[\delta_{x_k}(\delta p)] &= -\delta_{x_j}(\delta g_j)/\,\Delta t \\ &= -\delta_{x_j}(g_j^{k+1} - \widehat{g}_j)/\,\Delta t \\ &= \frac{1}{\Delta t}\left[\delta_{x_j}(\widehat{g}_j) + \frac{\rho^{k+1} - \rho^n}{\Delta t}\right] , \end{aligned} \tag{4.25}$$

where the continuity equation was used to substitute for $\delta_{x_j}(g_j^{k+1})$. The mass flux correction, δg_i, is assumed to be zero on the boundaries so that the boundary-normal component of (4.24) implies that the appropriate boundary condition for the Poisson equation is the Neumann condition, $\delta_n(\delta p) = 0$. Note that the source for this Poisson equation is simply the residual of the continuity equation for the next time step, which approaches zero as the iterations converge. Thus, errors associated with classical time splitting or fractional steps disappear with the present iterative approach.

Step 7: The velocity and pressure are updated:

$$g_i^{k+1} = \widehat{g}_i - \Delta t\, \delta_{x_i}(\delta p) \ ,$$

$$u_i^{k+1} = g_i^{k+1} \,/\, (\overline{\overline{\rho}^{x_i}}^{t})^{k+1} \ ,$$

$$p^{k+1} = p^k + \delta p \ .$$

The continuity equation based on the density determined in Step 3 is now satisfied exactly. This completes one full cycle of the iterative process. If more iterations are desired the process would continue with Step 2.

While only two iterations are required to ensure second-order accuracy in time, in practice more iterations may be needed to ensure stability, particularly in reacting flows with high heat release. Experience has shown that flows with weak density variations require only 2 or 3 iterations, while reacting flows with large density ratios may require 4 or 5 iterations.

4.3 Scalar Advection

It is well known that linear advection of a scalar with central difference schemes is vulnerable to the formation of spatial oscillations or "wiggles" due to dispersion errors. Though the discretization of §4.1.3 is conservative and leads to numerically stable solutions even in the absense of diffusion, problematic oscillations can still arrise. While some tolerance for such oscillations can be built into the algorithm, central differences can cause scalars to disperse in disastrously unphysical ways, such as the propagation of oscillations into regions where the scalar is supposed to be uniform.

Figure 4.4 illustrates the problem for linear advection of a Gaussian bump, which is governing by the equation,

$$\frac{\partial \phi}{\partial t} + c\frac{\partial \phi}{\partial x} = 0 \ ,$$

with constant advection velocity, c. The exact dispersion relation for this equation is $\omega(k) = ck$, where ω is the angular frequency of a Fourier mode and k is

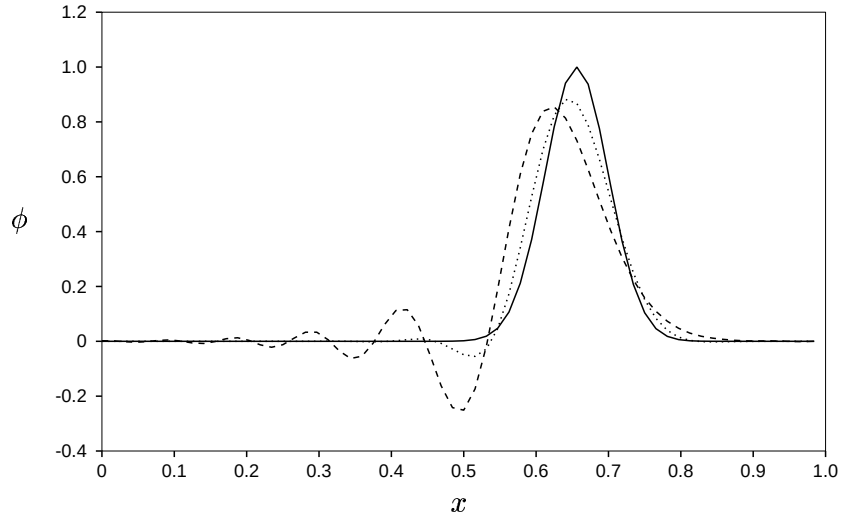

Fig. 4.4 Numerical dispersion of a Gaussian bump after being advected to the right a distance of one unit. – – – : second-order central difference; ····· : QUICK scheme; —— : exact. Periodic boundary conditions and 64 grid points were used.

the wavenumber. If we use a finite-difference scheme to approximate the spatial derivative and assume that time integration remains exact, the numerical dispersion relation becomes $\omega(k) = ck'(k)$, where $k'(k)$ is the modified wavenumber of the finite-difference scheme (see Fig. 4.2). Thus, the modified wavenumber can be interpreted as a numerical dispersion relation for linear advection. For wavenumbers higher than the peak in the modified wavenumber diagram, the group velocity, $d\omega/dk$, is actually negative, so that wiggles can, in fact, propagate upstream.

To combat the severe problems that can arise due to dispersion error in finite-difference schemes, an upwind biased scheme was adopted for scalar advection only. It can be argued that, while upwind schemes are detrimental when used for computation of turbulent velocity fields due to their damping effect on turbulence spectra (Mittal and Moin 1997), their deleterious effects on scalar advection are relatively minor, because scalar transport is linear (no scale interaction), and thus, the damping of small scales does not affect the dynamics of the large scales. While many schemes have been developed for the scalar advection problem (SUPG, TVD, *etc.*), for simplicity, the present study uses the QUICK scheme (Leonard 1979), which replaces

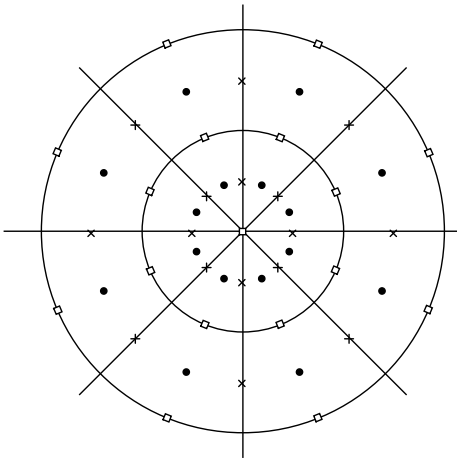

Fig. 4.5 Staggered grid with cylindrical coordinates. Only the u_r velocity component is located at the centerline. $\bullet$: ρ, p, ϕ, u_x; $\times$: u_θ; $\square$: u_r.

the two-point interpolation of §4.1.3 with an upwinded, three-point interpolation to the cell face when computing scalar advective fluxes, resulting in a five-point stencil overall. Accordingly, when scalar advection is treated implicitly, penta-diagonal algebraic equations must be solved. For further details, see Akselvoll and Moin (1995). The effect of the QUICK scheme on the linear advection problem is also shown in Fig. 4.4, where it can be seen that the QUICK scheme reduces but does not eliminate the appearance of wiggles.

4.4 Cylindrical Coordinates

The governing equations are solved in cylindrical coordinates in order to take advantage of symmetries in the coaxial jet combustor of §5.1. The coordinates x, r, and θ correspond to the axial, radial, and azimuthal directions respectively.

4.4.1 Discrete Equations in Cylindrical Coordinates

The fully discrete equations of §4.1.3, when expressed in cylindrical coordinates, take the following form. A schematic of the grid is shown in Fig. 4.5 for reference.

Mass Fluxes:

$$g_x = \overline{\overline{\rho}^x}^t u_x \ , \qquad g_r = \overline{\overline{\rho}^r}^t u_r \ , \qquad g_\theta = \overline{\overline{\rho}^\theta}^t u_\theta$$

Velocity Divergence:

$$\Theta = \delta_x(u_x) + \frac{1}{r}\delta_r(ru_r) + \frac{1}{r}\delta_\theta(u_\theta)$$

Continuity:

$$\delta_t(\rho) + \delta_x(g_x) + \frac{1}{r}\delta_r(rg_r) + \frac{1}{r}\delta_\theta(g_\theta) = 0$$

Momentum:

$$\delta_t(g_x) = \delta_x(f_{xx}) + \frac{1}{r}\delta_r(rf_{xr}) + \frac{1}{r}\delta_\theta(f_{x\theta})$$

$$\delta_t(g_r) = \delta_x(f_{rx}) + \frac{1}{r}\delta_r(rf_{rr}) + \frac{1}{r}\delta_\theta(f_{r\theta}) - \frac{\overline{f_{\theta\theta}}^r}{r}$$

$$\delta_t(g_\theta) = \delta_x(f_{\theta x}) + \frac{1}{r}\delta_r(rf_{\theta r}) + \frac{1}{r}\delta_\theta(f_{\theta\theta}) + \frac{\overline{f_{\theta r}}^r}{r}$$

$$f_{xx} = 2\mu[\delta_x(\overline{u_x}^t) - \tfrac{1}{3}\overline{\Theta}^t] - \overline{\overline{g_x}^x}^t\overline{\overline{u_x}^x}^t - p$$

$$f_{rr} = 2\mu[\delta_r(\overline{u_r}^t) - \tfrac{1}{3}\overline{\Theta}^t] - \overline{\overline{g_r}^r}^t\overline{\overline{u_r}^r}^t - p$$

$$f_{\theta\theta} = 2\mu\Big[\frac{1}{r}\delta_\theta(\overline{u_\theta}^t) + \frac{\overline{\overline{u_r}^r}^t}{r} - \tfrac{1}{3}\overline{\Theta}^t\Big] - \overline{\overline{g_\theta}^\theta}^t\overline{\overline{u_\theta}^\theta}^t - p$$

$$f_{xr} = \overline{\overline{\mu}^x}^r\Big[\delta_x(\overline{u_r}^t) + \delta_r(\overline{u_x}^t)\Big] - \overline{\overline{g_r}^x}^t\overline{\overline{u_x}^r}^t$$

$$f_{rx} = \overline{\overline{\mu}^x}^r\Big[\delta_x(\overline{u_r}^t) + \delta_r(\overline{u_x}^t)\Big] - \overline{\overline{g_x}^r}^t\overline{\overline{u_r}^x}^t$$

$$f_{r\theta} = \overline{\overline{\mu}^r}^\theta\Big[\delta_r(\overline{u_\theta}^t) + \frac{1}{r}\delta_\theta(\overline{u_r}^t) - \frac{\overline{\overline{u_\theta}^r}^t}{r}\Big] - \overline{\overline{g_\theta}^r}^t\overline{\overline{u_r}^\theta}^t$$

$$f_{\theta r} = \overline{\overline{\mu}^r}^\theta\Big[\delta_r(\overline{u_\theta}^t) + \frac{1}{r}\delta_\theta(\overline{u_r}^t) - \frac{\overline{\overline{u_\theta}^r}^t}{r}\Big] - \overline{\overline{g_r}^\theta}^t\overline{\overline{u_\theta}^r}^t$$

$$f_{x\theta} = \overline{\overline{\mu}^x}^\theta\Big[\delta_x(\overline{u_\theta}^t) + \frac{1}{r}\delta_\theta(\overline{u_x}^t)\Big] - \overline{\overline{g_\theta}^x}^t\overline{\overline{u_x}^\theta}^t$$

$$f_{\theta x} = \overline{\overline{\mu}^x}^\theta\Big[\delta_x(\overline{u_\theta}^t) + \frac{1}{r}\delta_\theta(\overline{u_x}^t)\Big] - \overline{\overline{g_x}^\theta}^t\overline{\overline{u_\theta}^x}^t$$

Scalar Transport:

$$\delta_t(\rho\phi) = \delta_x(q_x) + \frac{1}{r}\delta_r(rq_r) + \frac{1}{r}\delta_\theta(q_\theta) + \rho w$$

$$q_x = \overline{\rho\alpha}^x\delta_x(\overline{\phi}^t) - g_x\overline{\overline{\phi}^x}^t$$

$$q_r = \overline{\rho\alpha}^r\delta_r(\overline{\phi}^t) - g_r\overline{\overline{\phi}^r}^t$$

$$q_\theta = \overline{\rho\alpha}^\theta\frac{1}{r}\delta_\theta(\overline{\phi}^t) - g_\theta\overline{\overline{\phi}^\theta}^t$$

Note that the pressure has been included in the momentum flux tensor, f_{ij}, rather than written as a separate gradient term. In the radial momentum equation, pressure contributes to both the radial flux and curvature terms, which combine to yield an equivalent gradient term:

$$\frac{1}{r}\delta_r(rp) - \frac{\overline{p}^r}{r} = \delta_r(p) \ .$$

4.4.2 Centerline Treatment

The centerline treatment used in this work differs considerably from that used by Akselvoll and Moin (1995). Referring to Fig. 4.5, it is clear that all quantities except u_r are staggered in the radial direction with respect to the centerline (*i.e.*, they are located at $\Delta r/2$ from the centerline), while u_r itself is collocated with the centerline. An analysis of the discrete equations reveals that centerline conditions are actually not needed for any of the variables, except for u_r and $f_{\theta r}$. Derivatives of quantities that are staggered with respect to the centerline can be obtained by differencing opposing values across the centerline, accounting for reversals in the directions of the radial and azimuthal unit vectors through the centerline (Mohseni and Colonius 2000). Centerline boundary conditions for u_r and $f_{\theta r}$ are obtained by averaging corresponding values across the centerline (Akselvoll and Moin 1995):

$$u_r(r=0,\theta) = \tfrac{1}{2}[u_r(\Delta r,\theta) + u_r(\Delta r,\theta+\pi)] \ . \tag{4.26}$$

The approach is designed to allow radial flow communication through the centerline without undue influence to or from points at neighboring θ locations. The angular distribution of u_r at the centerline does not necessarily conform to a single-valued centerline velocity vector.

Grid quality was found to be important near the centerline in order to maintain solution stability. Although derivatives in radial direction are treated implicitly, the scheme is in fact explicit in the radial direction at the centerline itself because tri-diagonal equations are not coupled through the centerline. Thus, excessive refinement of the radial grid at the centerline can create stiffness. Also, excessive

grid stretching at the centerline was found to promote the formation of unstable "wiggles" in the radial velocity component near the centerline.

4.4.3 Exact Representation of Uniform Flow

A uniform velocity field is represented in Cartesian coordinates as a vector with constant components:

$$\boldsymbol{u} = (U,\ V,\ W)\ .$$

However, in cylindrical coordinates the components are not constant but vary with θ:

$$\boldsymbol{u} = (U,\ V\cos\theta + W\sin\theta,\ -V\sin\theta + W\cos\theta)\ .$$

When derivatives in the r and θ momentum equations are calculated using finite differences, the discrete equations are not necessarily statisfied by the above uniform flow solution. The discrepancies are particularly noticeable near the centerline, where errors can be magnified by the $1/r$ factor.

It is usually desireable that a discrete representation of the governing equations satisfy exactly certain trivial flow situations, the case of uniform flow being the simplest. This was achieved in the present formulation by "tweaking" certain differencing and interpolation operators in the discrete momentum equations with multiplicative correction factors, so that a uniform flow satisfies the equations exactly, while second-order accuracy is maintained. Specifically, derivatives and interpolations in the θ direction are modified according to

$$\delta_\theta(u) \longrightarrow \frac{\sin(\Delta\theta/2)}{\Delta\theta/2}\delta_\theta(u)\ , \qquad \overline{u}^\theta \longrightarrow \cos(\Delta\theta/2)\overline{u}^\theta\ . \tag{4.27}$$

The above modifications can be thought of as accounting for the finite angular spacing of the computational grid. Note that as $\Delta\theta \to 0$, the correction factors approach unity.

4.5 Boundary Conditions

Staggered grids can be problematic when boundary conditions need to be applied, because some of the variables may not be properly located with respect to the

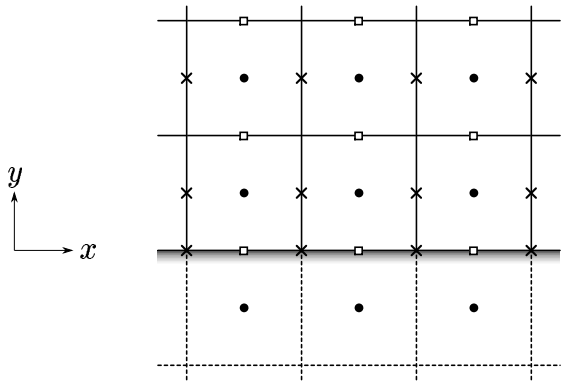

Fig. 4.6 Staggered grid at a wall boundary. When Dirichlet conditions need to be applied, staggered variables are relocated to the wall. • : ρ, p, ϕ; × : u_x; □ : u_y.

boundary. Figure 4.6 depicts a typical boundary in two dimensions, to illustrate some of the issues encountered when applying boundary conditions on staggered grids. For Dirichlet conditions, it is desirable for a variable to be located on the boundary itself, while for Neumann conditions, the more natural arrangement would be to have the variables staggered with respect to the boundary. Wall boundaries can be difficult because they require the enforcement of boundary conditions at specific physical locations, while inflow, outflow, and "open" boundaries are not subject to this problem because boundary conditions can be applied to variables at their staggered locations.

4.5.1 Wall Boundaries

The wall boundary conditions used in the present study are Neumann conditions for all scalars and pressure, and no-slip Dirichlet conditions for velocity. As discussed above, the Neumann conditions are easy to apply because pressure and scalars are naturally staggered with respect to the boundary. Likewise, Dirichlet conditions are easy to apply to the normal component of velocity because it is collocated with the wall. However, the no-slip condition for wall-tangential components of velocity is more difficult to enforce. One solution to the problem is to "de-stagger" the tangential velocity components in order to locate them at the wall (Fig. 4.6), so that the no-slip condition can be directly applied. However, an undesirable side effect of

this grid redefinition is to create a discontinuity in the wall-normal grid spacing at the boundary, which causes the wall-normal difference operator to become only first order accurate. This has led other investigators (Caruso 1985; Akselvoll and Moin 1995) to consider three-point, one-sided difference operators for computing the wall stress. However, giving special treatment to the numerical method on boundaries was considered undesireable for code generality, and for simplicity, the wall stress was computed using the standard two-point difference operator even though the accuracy is degraded to first order.

4.5.2 Inflow Conditions

Turbulent inflow conditions for LES must reflect the three-dimensional, unsteady nature of turbulence. In principle, the computational domain should be extended to include all the upstream geometry and flow conditioning devices (such as swirl vanes) that may influence flow properties farther downstream. But because this is usually not practical, approximate inflow conditions must be considered. In many cases, the inflow condition is a developing turbulent duct flow that can be approximated as fully developed. The unsteady inflow conditions can then be generated by simulating a spatially periodic section of the duct. Generalization of this approach to generate swirling inflow conditions is discussed by Pierce and Moin (1998b).

In the present study, a separate inflow generation code was used to create an "inflow database". The inflow generator simulates a spatially periodic, fully developed, parallel duct flow. Every few time steps, a cross section of velocity data is saved to the inflow database, until sufficient inflow data have been accumulated to provide converged turbulence statistics. In the main simulation, planes of velocity data are read from the inflow database in succession and applied to the inflow boundary. Linear interpolation in both space and time is performed when the inflow database grid and time step do not exactly match the grid and time step of the main simulation. If the end of the database is reached before the simulation is completed, inflow sampling returns to the beginning of the database, thereby recycling turbulent inflow conditions when necessary. This is not expected to cause

any problems when the database contains sufficient samples to produce converged statistics and when the main simulation contains flow time scales longer than the inflow recyling interval.

When the inflow conditions cannot be approximated as fully developed, their specification becomes significantly more difficult. Usually, some specified mean velocity or turbulence statistics profiles are known from an experiment or a Reynolds-average calculation, and it is desired to have the same statistics profiles applied to the inflow boundary of the LES. However, as stated in the beginning of this section, LES requires instantaneous turbulence data, not merely their statistical properties. Previous approaches to this problem (Le and Moin 1994; Akselvoll and Moin 1995) involved the specification of statistically constrained random numbers at the inflow boundary, which was followed by a development section that allowed the random numbers to develop into realistic turbulence. Although random numbers are easy to synthesize, they do not make a very attractive boundary condition because of the need for a costly development section and because of the fact that initial random numbers that are constrained to have the proper statistics do not necessarily develop into turbulence having the desired statistics. In fact, extreme changes in the flow are observed to occur within the first few grid points downstream of the imposed boundary condition.

A more attractive approach is to generalize the "fully developed" approximation described above to include the larger class of parallel flows having arbitrarily specified velocity statistics profiles. This type of flow is created by simulating a spatially periodic, parallel duct flow and constraining it using a corrective "forcing" technique. The resulting flow has the desired statistical properties, and it provides realistic turbulence data that are in "equilibrium" with the specified mean statistics. In the following, x is the streamwise coordinate direction, y and z are cross-stream directions, and $u(x, y, z, t)$ is the instantaneous streamwise velocity component. Assume that a desired mean velocity profile, $U(y, z)$, and fluctuation intensity profile, $U'(y, z)$ are given. The forcing technique then proceeds as follows. At each time step, the streamwise-averaged velocity, $\overline{u}(y, z, t)$, and fluctuation vari-

ance, $\overline{u'^2}(y,z,t)$, are computed:

$$\overline{u}(y,z,t) = \langle u(x,y,z,t) \rangle_x \ ,$$

$$\overline{u'^2}(y,z,t) = \left\langle u(x,y,z,t)^2 \right\rangle_x - \overline{u}(y,z,t)^2 \ .$$

Then, the instantaneous velocity field is rescaled and shifted so that is has the specified mean and fluctuating velocity profiles:

$$u(x,y,z,t) \longrightarrow \frac{U'(y,z)}{\sqrt{\overline{u'^2}(y,z,t)}} \left[u(x,y,z,t) - \overline{u}(y,z,t) \right] + U(y,z) \ . \tag{4.28}$$

This would be equivalent to adding an appropriately defined body force to the u-component momentum equation. If only the mean velocity profile is constrained, then (4.28) would be replaced by the simpler procedure,

$$u(x,y,z,t) \longrightarrow u(x,y,z,t) - \overline{u}(y,z,t) + U(y,z) \ . \tag{4.29}$$

The above approach appears to be an attractive alternative for generating realistic turbulent inflow conditions having specified mean statistical properties and was considered in this study when fully developed conditions were deemed to be inadequate.

4.5.3 Outflow Conditions

The convective condition is used for all "outflow" boundaries, which may also include "open" boundaries where the flow may actually enter the domain, as occurs for example, when ambient fluid is entrained into a free jet. Mathematically, this condition is written,

$$\frac{\partial \phi}{\partial t} + c \frac{\partial \phi}{\partial n} = 0 \ , \tag{4.30}$$

where ϕ is any scalar variable or velocity component, c is the convection velocity, and n is the coordinate in the direction of the outward normal at the boundary. In non-Cartesian coordinates, the normal component of velocity satisfies a slightly modifed form of the convective condition to account for changes in flow area in

the direction normal to the boundary. Instead of $\partial u_n/\partial n$, the corresponding term from the continuity equation is used. For example, in cylindrical coordinates, the convective condition for the radial component of velocity at a radially oriented outflow boundary satisfies,

$$\frac{\partial u_r}{\partial t} + c\frac{1}{r}\frac{\partial r u_r}{\partial r} = 0 \ . \tag{4.31}$$

This ensures that the time-average of the ouflow mass flux is the same as the mass flux at the first interior point away from the boundary.

Normal derivatives at the outflow boundary are evaluated using one-sided, first-order differences, and the convection velocity is taken to be constant over the outflow boundary. Flow structures that approach the boundary at speeds higher than c are forced to slow and compress in a manner similar to a stagnation point, often with the formation of unphysical "wiggles" that can propagate upstream (§4.3), while structures that move slower than c will be stretched and "pulled" out of the domain without wiggle formation. If c is too large, however, the CFL restriction may limit the time step, and in the limit $c \to \infty$, the convective condition approaches a Neumann condition. Based on these observations, a good choice for c will be just large enough to prevent structures from stagnating at the boundary. Thus, c is changed at each time step to equal the maximum outflow velocity over the outflow boundary, $c = \max(u_n)$.

Global mass conservation is satisfied if the total outflow mass flux balances the total inflow mass flux plus the net change in mass storage in the interior of the domain. This is enforced at each time step by adding a corrective constant to the outflow velocity (except at the walls in the boundary plane), to mimic the physical response to a uniform pressure gradient at the outflow boundary. Thus, changes in the inflow mass flow rate, as well as heat release fluctuations in the interior domain, are balanced by adjustments to the outflow mass flow rate.

Chapter 5

APPLICATION TO A COAXIAL JET COMBUSTOR

The models and numerical methods described in previous chapters were tested against experimental data for a methane fueled coaxial jet combustor. Simulations were performed using all three chemistry models presented in §3.3 under otherwise identical conditions and were compared with each other and with experimental data. In addition, the importance of accounting for differential diffusion effects with the progress-variable approach was examined. The results show that only the progress-variable approach predicts a lifted flame and gives satisfactory agreement with experimental data in the region close to the inlet. If unity Lewis numbers are assumed and differential diffusion is neglected, the results for the progress-variable approach are significantly worse when compared to experimental data in the region close to the inlet, where the interaction between chemical kinetics and mixing is important.

5.1 Experimental Configuration

The experimental study used for the validation of the simulation methodology was the coaxial jet combustor configuration of Owen *et al.* (1976). This experiment was chosen for its relatively simple geometry and boundary conditions yet complex flow patterns resembling those in a gas turbine combustor, and for the availability of detailed measurements that map the species, temperature, and velocity fields within the combustor. The experimental study consisted of eight test cases conducted under various operating conditions and geometric modifications. The particular case used for the present validation, referred to as "Test 1" in the laboratory report (Spadaccini *et al.* 1976), is depicted in Fig. 5.1.

The configuration had a relatively large diameter, low velocity central fuel port, with higher velocity, nonswirling air in a surrounding annulus. The air was preheated to 750K, and the combustor was pressurized to 3.8 atm. Porous-metal discs were installed in the fuel injector and air entry section to provide uniform inlet

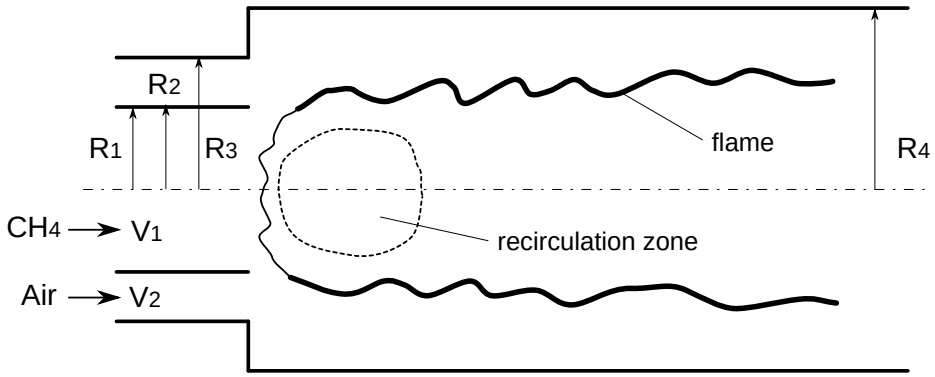

Fig. 5.1 Schematic of the coaxial jet combustor experiment.

flows. The walls of the combustor were water-cooled to maintain a constant wall temperature of roughly 500K. The dimensions and flow conditions specified in the experiment are summarized below:

central pipe radius (R_1):	3.157 cm
annular inner radius (R_2):	3.175 cm
annular wall thickness ($R_2 - R_1$):	0.018 cm
annular outer radius (R_3):	4.685 cm $\equiv R$
combustor radius (R_4):	6.115 cm
combustor length:	100.0 cm
mass flow rate of fuel:	0.00720 kg/s
mass flow rate of air:	0.137 kg/s
bulk velocity of fuel (V_1):	0.9287 m/s
bulk velocity of air (V_2):	20.63 m/s $\equiv U$
overall equivalence ratio:	0.9
temperature of fuel:	300 K
temperature of air:	750 K
combustor pressure:	3.8 atm

The fuel used in the experiment was natural gas but for the present investigation was assumed to be pure methane. Also, dry air was assumed. The experimental data include radial profiles taken at usually four axial stations, of selected species concen-

trations (measured using a traversing gas sampling probe), temperature (measured by a traversing thermocouple), and axial velocity (measured by laser Doppler velocimetry).

Figure 5.1 also shows a schematic of the flame configuration observed in the experiment. Because of the high air/fuel velocity ratio, a strong central recirculation zone is formed directly in front of the fuel port, which appears to the surrounding air stream almost as a bluff body. The recirculating combustion products provide a continuous ignition source for the relatively cold incoming reactants, thereby stabilizing the flame. The flame location, shown as a thick convoluted line in Fig. 5.1, was observed in the experiment to lift off from the burner and reattach intermittently, in a highly unsteady manner. The length of the flame extended beyond the experimental test section, as well as the computational domain used for the simulations.

The experimentally reported species concentrations were post-processed in order to facilitate comparison with the simulation results. The mole fractions reported in the laboratory report were converted to mass fractions, and mixture fraction and product mass fraction were computed. The following procedure was used: Data were reported for the mole fractions of O_2, CH_4, CO_2, CO, and NO. Mole fractions for the species H_2O and H_2 were assumed to follow stoichiometric relationships: $x_{H_2O} = 2x_{CO_2}$ and $x_{H_2} = 2x_{CO}$. An estimate of the nitrogen mole fraction was obtained from the total oxygen atom mole fraction: $x_{N_2} = 1.88(2x_{O_2} + 2x_{CO_2} + x_{H_2O} + x_{CO})$. Then, mass fractions were computed by neglecting NO and all other species. Mixture fraction was computed based on the total carbon and hydrogen atom mass fractions, and product mass fraction was computed from $y_P = y_{CO_2} + y_{H_2O}$. The six data points for the CH_4 mole fraction in the fuel-rich region at the first measurement station were not provided because the concentrations were higher than the maximum calibration range of the gas analyzer. These missing data were filled in using the above assumptions and the requirement that mole fractions should sum to unity.

5.2 Computational Setup

A picture of the grid used for all of the simulations is shown in Fig. 5.2. The distribution of grid points was not determined by any systematic rules, but rather by experience and trial-and-error, although general requirements are that the grid be smooth and be refined near solid boundaries and in particular in the axial direction at the jet orifice. The thinness of the annular wall separating fuel and air required that especially fine radial resolution be used there. The size of the grid was $256 \times 150 \times 64$ points in the axial, radial, and azimuthal directions, respectively, and was determined by cost considerations as the largest grid on which the simulations could be completed in a reasonable amount of time.

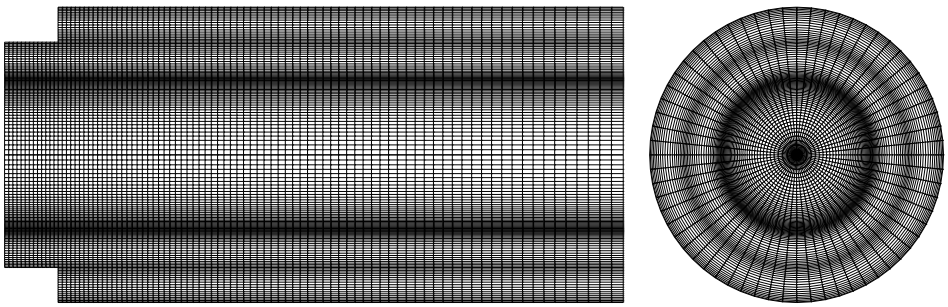

Fig. 5.2 Schematic of the grid used for the simulations. Only half of the points in the axial and radial directions are shown for clarity.

The simulations were computed using length (R), velocity (U), and time (R/U) scales normalized by the injector radius ($R \equiv R_3$) and the inlet bulk velocity of the air ($U \equiv V_2$). All simulation results are presented and compared with the experimental data using these units. The computational domain started at a distance of $1R$ upstream of the combustor, where fully developed turbulent inflow conditions were specified using the method of §4.5.2, even though the experimental inflow conditions were probably not fully developed. The computational domain continued until a combustor length of $8R$ was reached, at which point convective outflow boundary conditions (§4.5.3) were specified. All of the solid boundaries were assumed to be adiabatic and impermeable, including the annular splitter plate, even though the combustor walls in the experiment were isothermal.

To initialize a new simulation, the velocity and scalar fields are initially set to zero everywhere. Pressure impulsively starts the flow as inlet conditions are applied, initially producing a potential flow. The Reynolds number is temporarily reduced for the first few time steps to avoid problems with initial sharp gradients. A starting vortex forms at the jet orifice, convects downstream, and eventually leaves the domain. Turbulence from the inlet gradually fills the domain, eventually becoming fully developed. All future simulations of the same configuration, for example after adjusting the grid or changing the chemistry model, are initialized by interpolating previous fully-developed solutions. Fully developed incompressible velocity and mixing fields are obtained before the chemistry model is turned on. For the progress-variable approach (§3.3.4), the initial progress scalar field is set to its maximum allowed value determined from fast chemistry, so that initially the flame is fully ignited.

Solutions to the flamelet equations (3.35) were computed using GRI-MECH 3.0 and multicomponent mass diffusion, including Soret and Dufour effects for completeness. The parameter L_0 in (3.39) was chosen to be 2 cm. Additional flamelet libraries were computed using other mass diffusion models for the results of §5.3.2. For the progress-variable approach, product mass fraction ($y_{\mathrm{P}} = y_{\mathrm{CO_2}} + y_{\mathrm{H_2O}}$) was chosen to serve as the progress variable. The log-normal distribution for dissipation rate was used with the steady flamelet model. When the steady flamelet model was used in the simulation, a type of feedback instability was observed: A sudden increase in the dissipation rate can cause a sudden increase in density, which during the following time step can cause the dissipation rate to increase even further. Likewise, a sudden decrease in dissipation rate can cause the density to decrease, further decreasing the dissipation rate at the next time level. In order to avoid the instability, a time filtering was applied, in which the computed dissipation rate, $\widetilde{\chi}$, was averaged with the dissipation rate computed at the previous time step (not the previous average) before it was used to determine a new density field.

The computational time step was was selected by computing a generalized CFL number,

$$\mathrm{CFL} = \frac{u\,\Delta t}{\Delta x} + \frac{\nu\,\Delta t}{\Delta x^2} \ , \tag{5.1}$$

based only on axial convection and diffusion. Radial and azimuthal convection and diffusion are not included in the CFL estimate because these terms are treated implicitly. A time step of 0.005 R/U was used for all of the simulations and corresponded to a CFL number that varied within a range of about 0.5 – 1.0. For the progress-variable approach, the maximum progress-variable reaction rate in the flamelet library was sufficiently small that no stiffness was caused by the chemical source term.

All of the statistical results obtained from the simulations are based on simple averages of the resolved fields in time and in the azimuthal direction. No attempt was made to account for subgrid contributions to the statistics or to account for any effects due to the implicit Favre filtering described in §3.1. Because of the long time scales present in the combustor, a large number of time steps was required to integrate the flow long enough to obtain reasonably converged statistics. The total time needed for initial flow development as well as statistical sampling was about 500 R/U time units or 100,000 time steps for each simulation. The simulations were run on the ASCI Red platform (Sandia National Laboratory, Albuquerque, New Mexico) using 512 processors, yielding a sustained aggregate performance of 10 Gflops, or about 3.7 seconds per time step. Thus, about 50,000 processor-hours were used per simulation.

5.3 Results

A total of four large eddy simulations of the coaxial jet combustor described in §5.1 were performed, each configured with exactly the same computational parameters, but using a different chemistry model: (1) fast chemistry, (2) steady flamelets, (3) progress-variable approach, and (4) progress-variable approach with unity Lewis numbers. The first three simulations are compared in §5.3.1, where it is found that both the fast chemistry and steady flamelet models fail to account for extinction

and flame lift-off close to the burner, while the progress-variable approach predicts a lifted flame and obtains favorable agreement with the experimental data. The third and fourth simulations are compared in §5.3.2 to demonstrate that inclusion of differential diffusion effects is necessary to obtain good agreement with the experimental data.

5.3.1 Chemistry Model Comparison

In this section, results for the three chemistry models described in §3.3 are examined and compared to each other and to experimental data. The most important question to be answered is whether the simulation methodology is capable of accurately capturing the gross characteristics and behavior of the flame, such as the rate of product formation and heat release, flame lift-off, ignition, and extinction. Characteristics that depend on the details of the combustion process, such as pollutant formation, are not a target of the present effort. The primary quantities that are used to examine the characteristics of each simulation are the mixture fraction (Z) and product mass fraction ($y_{\mathrm{P}} = y_{\mathrm{CO_2}} + y_{\mathrm{H_2O}}$).

Figure 5.3 compares instantaneous, planar snapshots of mixture fraction for each of the chemistry models: (a) fast chemistry, (b) steady flamelet, and (c) progress variable approach. Since the three simulations are configured identically except for the chemistry model, and since mixture fraction is a conserved scalar, which does not participate in chemical reactions, one might expect the mixture fraction results for the three cases to be very similar. But scalar mixing can be strongly influenced by heat release, which depends directly on the chemistry model. This is because heat release causes flow dilatation to occur within the thin mixing layers between fuel and oxidizer, thereby pushing apart fuel and oxidizer when they try to mix. In general, the rate of mixing is found to decrease with higher rates of chemical heat release, so that mixture fraction can be used as an indicator of whether the location and rate of chemical reactions are accurately predicted by the chemistry model. The effect of heat release on mixing is clearly visible when comparing the mixing characteristics in the initial thin mixing layers just after the annular splitter

plate in Fig. 5.3(a,b), where mixing appears weak, and in Fig. 5.3(c), where small rollers are visible. The general conclusion to be drawn from Fig. 5.3 is that, of the three chemistry models tested, the fast chemistry model has the lowest rate of mixing, the progress-variable approach has the highest, and the rate of mixing with the steady flamelet model lies somewhere between the other two, all due to the resulting heat release rate.

Corresponding pictures of product mass fraction are shown in Fig. 5.4. Flame location is identified by the regions of highest product concentration, typically appearing as thin corrugated white lines. Both the fast chemistry and steady flamelet models clearly have attached flames, while the progress variable approach shows a much more complicated and asymmetric pattern: At the particular instant shown, the flame is lifted on the upper side of the injector and is intermittently attached on the lower side. This behavior is highly unsteady and must be viewed as an animation to be fully appreciated. Because of the extinction occurring on the upper side, unburned reactants are able to penetrate into the interior of the flame as indicated by the darker areas in the center of Fig. 5.4(c). The small amounts of product visible in the inlet region of the fuel port are due to occasional recirculation of hot products inside the inlet. In Fig. 5.4(a), the fast chemistry model always predicts the theoretical maximum product mass fraction for the given mixture fraction. The highest product mass fraction possible is approximately $y_{\mathrm{P}} = 0.275$ and occurs at the stoichiometric mixture fraction, $Z_{\mathrm{st}} = 0.0552$, when all fuel and oxidizer have been converted into product. In Fig. 5.4(b), the steady flamelet model predicts significantly lower product mass fractions than the theoretical maximum. This is due to the "quenching" effect that scalar dissipation rate has on diffusion flame structure. The steady flamelet model also shows numerous small-scale, wavy structures throughout the central region. These variations should be considered unphysical and a defect of the steady flamelet model, because they are due solely to local fluctuations in dissipation rate in a region where there is mixing between product and fuel but little or no reaction. In flamelet theory, it is the dissipation rate occurring at the flame surface (the "stoichiometric" dissipation rate) that controls the flame

structure. Accordingly, the description of chemical states in regions away from the flame is not well defined because the steady flamelet model has no way of creating a nonlocal connection between a given physical location of arbitrary mixture fraction and a particular physical location of stiochiometric mixture fraction. In the progress variable approach, this type of nonlocal interaction is mediated by the progress-variable transport equation.

Mixture Fraction

Figure 5.5 shows quantitatively what is observed qualitatively in Fig. 5.3, that the fast chemistry and steady flamelet models lead to lower mixing rates because of faster heat release, especially in the thin mixing layers close to the annular splitter plate. The steady flamelet model clearly offers substantial improvement over the fast chemistry model, but because it is also incapable of properly accounting for flame lift-off, the mixing profiles remain far above the experimental data. Note that all the profiles tend toward agreement as the profile station is moved farther downstream, due to the fact that they all must reach the same uniform profile once mixing is complete. Since most chemical quantities are correlated with mixture fraction, it is usually important to accurately predict mixture fraction profiles in order to accurately predict other chemical quantities. The scatter of the experimental data points in this and the following figures is due to the reflection about the centerline of data points taken on the opposite side of the combustor.

Product Mass Fraction

The quantitative picture corresponding to Fig. 5.4 is shown in Fig. 5.6. The first station clearly shows the similarity between the fast chemistry and steady flamelet models and their essential difference with the progress variable approach. Both the fast chemistry and steady flamelet models predict large product formation in the thin mixing layers near the annular splitter plate, what would be expected from an attached flame, while the progress variable approach has no such spike: The product concentration found at this station is due mainly to recirculation of products from reactions occurring farther downstream. At the remaining stations, the

fast chemistry model consistently overpredicts the levels of product concentration, while the steady flamelet model and progress variable approach both achieve good agreement with the experimental data, though it is difficult to say whether one is more accurate than the other because of the scatter in the experimental data.

Temperature

Comparison of predicted temperature profiles with experimental data is shown in Fig. 5.7. Temperature is a quantity that is derived from the mixture fraction and progress variable (mixture fraction alone in the fast chemistry and steady flamelet models) by assuming adiabatic walls and neglecting thermal radiation. Where these assumptions are valid, the temperature can be expected to behave very similarly to product mass fraction, but where the assumptions break down, an overprediction of temperature is expected. Therefore, if product mass fraction predictions are in good agreement with experimental data, discrepancies between predicted and measured temperature profiles must be due to the breakdown of these assumptions or to experimental error, which owing to differences in measurement technique between species concentrations and temperature can be significant. One of the investigators involved with the experiment has stated that the temperature data, having been measured using a rather large, invasive, and dynamically unresponsive thermocouple probe, are in fact subject to considerable experimental uncertainty, especially in regions with large temperature fluctuations (C. T. Bowman, private communication, 2001). It could also be the case that thermal radiation is nonnegligible in some regions of the flow, particularly in fuel-rich, slow moving regions where soot formation is likely and residence times are long enough for radiative effects to accumulate. It is also important to note that the axial measurement stations used for temperature are different from those used for species concentrations. In particular, the first two temperature stations are located between the first and second species measurement stations. Thus, the discrepancy between the progress variable approach and experimental data in the first two temperature stations may in fact reflect an underlying overprediction of product concentration as well, but since

species data are not available in this region, it is difficult to draw any definitive conclusions.

Another source of uncertainty is the effect of the assumption of adiabatic walls in the simulations. Since the experiment had isothermal, water-cooled walls at roughly 500K, thermal boundary layers would be expected to develop, affecting the temperature close to the wall. However, note that in Fig. 5.4, the annular air stream (at 750K) tends to create an insulating sheath between the hot combustion products and the wall, although it appears that the flame in Fig. 5.4(c) does occasionally brush up against the wall. These factors should account for the good agreement of the fast chemistry and steady flamelet models, and the overprediction of the progress variable approach near the wall at the last two stations in Fig. 5.7.

Velocity

Time-averaged axial velocity and axial fluctuation intensity results are shown in Fig. 5.8. While scalar mixing was found to be sensitive to the heat release characteristics of the chemistry model, surprisingly the time-averaged velocity field data are rather insensitive. In fact, the velocity data for the fast chemistry and steady flamelet models were found to be nearly indistinguishable. As the effects of heat release on the velocity field tend to be cumulative, velocity field differences between the three models can be expected to increase with axial distance. Indeed, the only significant difference between the fast chemistry, steady flamelet, and progress variable velocity fields appears at the final measurement station, where the progress-variable approach achieves significantly better agreement with the experiment.

The general level of agreement between simulation and experiment is satisfactory but not quite as good as what has been achieved with LES of incompressible turbulent flows. A significant part of the disagreement may be due to the fact that fully developed pipe and annular inflow conditions were assumed in the simulations, whereas in the experiment, flow conditioning devices were located only a short distance upstream of the jet orifice.

Finally, it should be noted that the axial location of the third measurement

station was reported to be "0.187 X/D" (0.49 x/R), where "D" is the diameter of the combustor. But based on the plausible rate of change of the flow patterns in the axial direction and other information contained in the report, this value was suspected of being a typographical error and was corrected to its most probable value of "0.487 X/D" (1.27 x/R).

Carbon Monoxide

Figure 5.9 presents the CO results for the steady flamelet model and progress variable approach. Note that the fast chemistry model with the major products assumption predicts zero carbon monoxide concentrations. The results clearly show that the progress variable approach has room for improvement, and that in this case, the steady flamelet model significantly outperforms the progress variable approach at the last station. Carbon monoxide is a significant species in the fuel-rich interior region of the flame. Because dissipation rates are low in this region, the steady flamelet model picks out near-equilibrium flamelet solutions, which have low temperatures and high concentrations of CO in fuel-rich mixtures. But this part of the flamelet library is not uniquely mapped by the progress variable, so that such high-CO chemical states cannot be accessed. One possible improvement is to consider using entropy as the progress variable, as entropy always increases monotonically as reactions progress towards equilibrium.

5.3.2 Importance of Differential Diffusion

One of the advantages of flamelet models is their ability to easily incorporate the effects of complex mass diffusion as well as complex chemical kinetics. Since the flamelet model provides a spatial variation to the flame structure, the effects of differential transport of species can be combined with the effects of differential reaction rates to compute a detailed, complex flame structure. Surprisingly, differential diffusion effects have often been ignored in classical flamelet models.

To demonstrate the strong effects that mass diffusion can have on flamelet models, flamelet libraries were computed using four different mass diffusion models and compared. The four flamelet libraries were computed with: full multicompo-

nent mass diffusion (2.7), approximate mixture diffusivities (2.10), the unity Lewis numbers assumption, and a constant and equal diffusivity for all species (independent of temperature and mixture fraction). The results (Fig. 5.10) show a dramatic difference in peak dissipation rate (and therefore maximum reaction rate) between the two differential diffusion models and the two equal diffusion models. This result can be understood by noting that the global reaction rate is set by the concentrations of radicals in the reaction zone, and radicals such as H, O, and OH can have significantly higher diffusivities than larger species such as CH_4 and CO_2. The conclusion to be inferred is that accurate treatment of differential diffusion can be just as important as accurate modeling of chemical kinetics.

An additional simulation of the coaxial jet combustor was performed using the progress variable approach with the unity Lewis numbers flamelet library. The effect of differential diffusion is not quite as dramatic in most regions, because much of the flow is governed by large-scale mixing instead of chemical kinetics and small-scale mixing. However, in the region close to the inlet, where flame lift-off and ignition are occurring, the effects are more pronounced. In Fig. 5.10, the peak dissipation rate in the unity Lewis numbers flamelet library is about 2.5 times the peak dissipation rate in the differential diffusion flamelet library, so that one should expect the maximum reaction rate of the unity Lewis numbers flame to be about 2.5 times that of the differential diffusion flame. Therefore, the unity Lewis numbers flame has a greater tendency to stay attached to the lip of the burner. This is clearly seen in the results in Fig. 5.11 and Fig. 5.12. With faster kinetics, the flame becomes more attached to the burner, and thus more heat release occurs in the initial thin mixing layers, causing reduced fuel/air mixing.

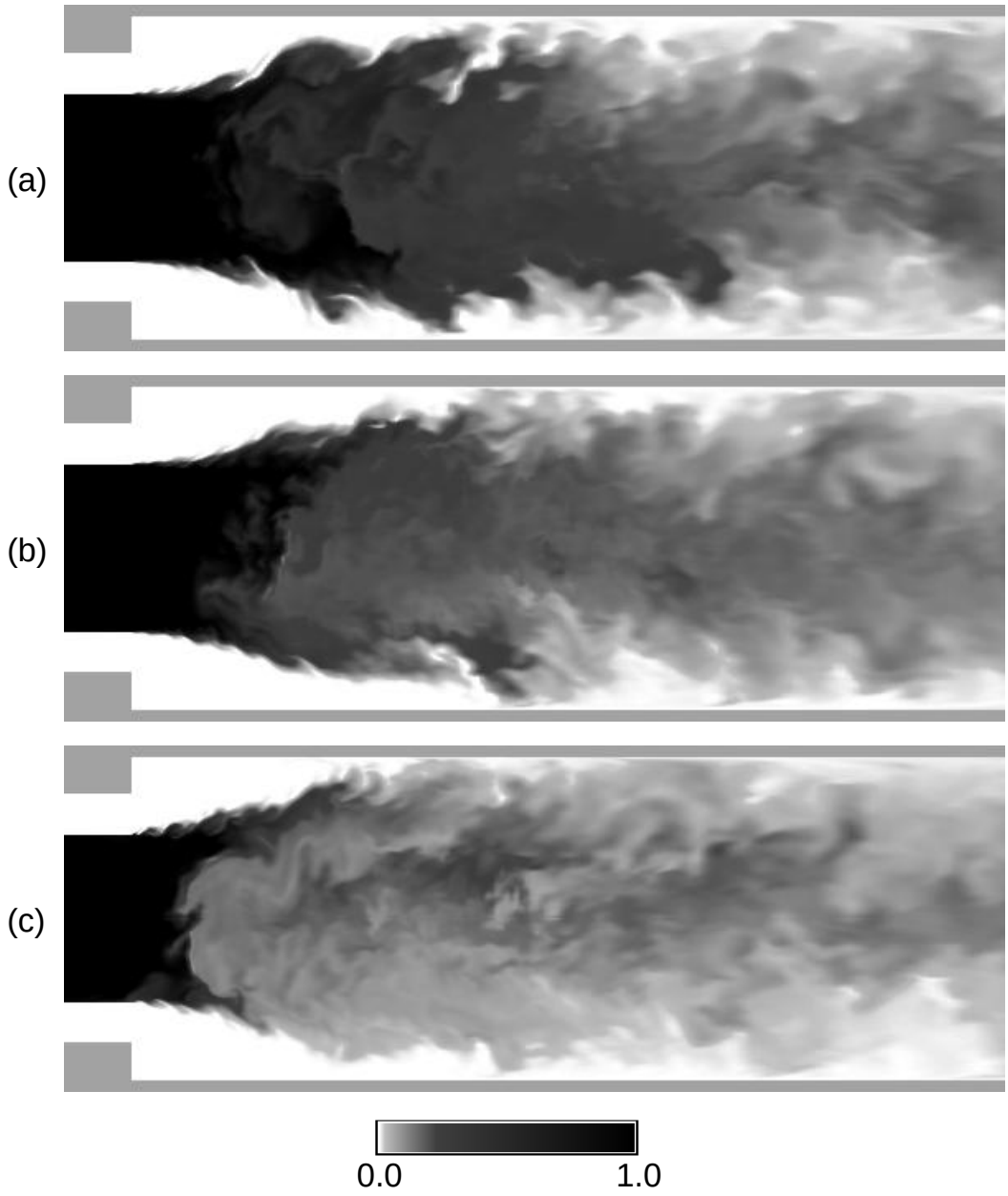

Fig. 5.3 Snapshot of mixture fraction in a meridional plane. (a) fast chemistry; (b) steady flamelets; (c) progress variable approach.

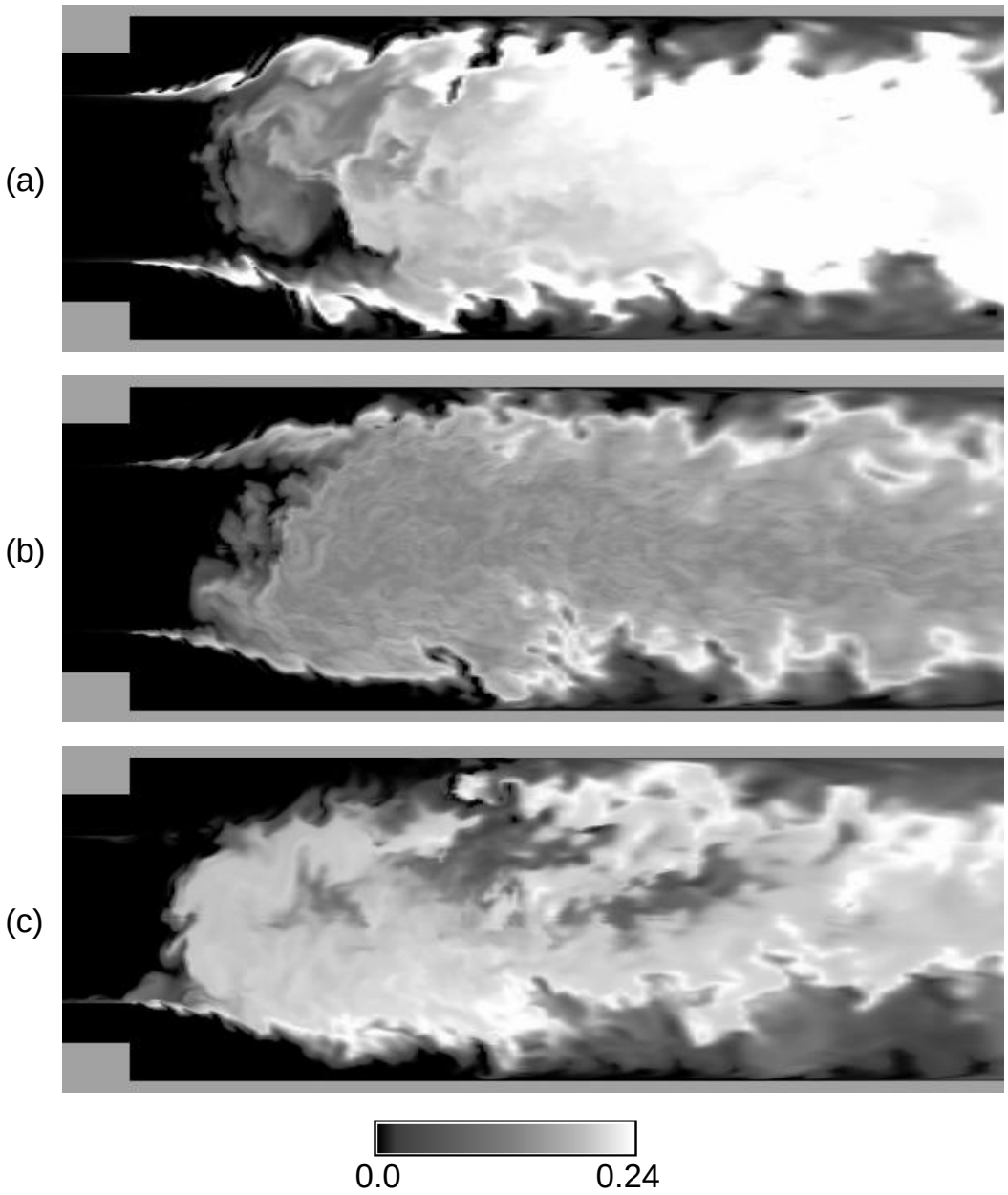

Fig. 5.4 Snapshot of product mass fraction in a meridional plane. (a) fast chemistry; (b) steady flamelets; (c) progress variable approach.

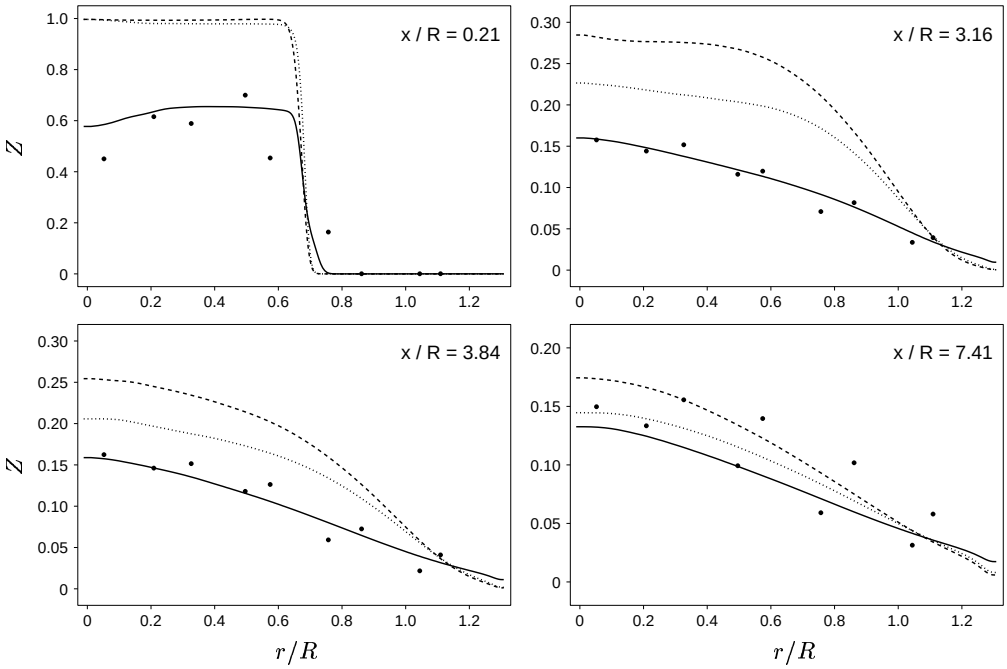

Fig. 5.5 Radial profiles of time-averaged mixture fraction. – – – : fast chemistry; ····· : steady flamelets; —— : progress variable approach; • : experiment.

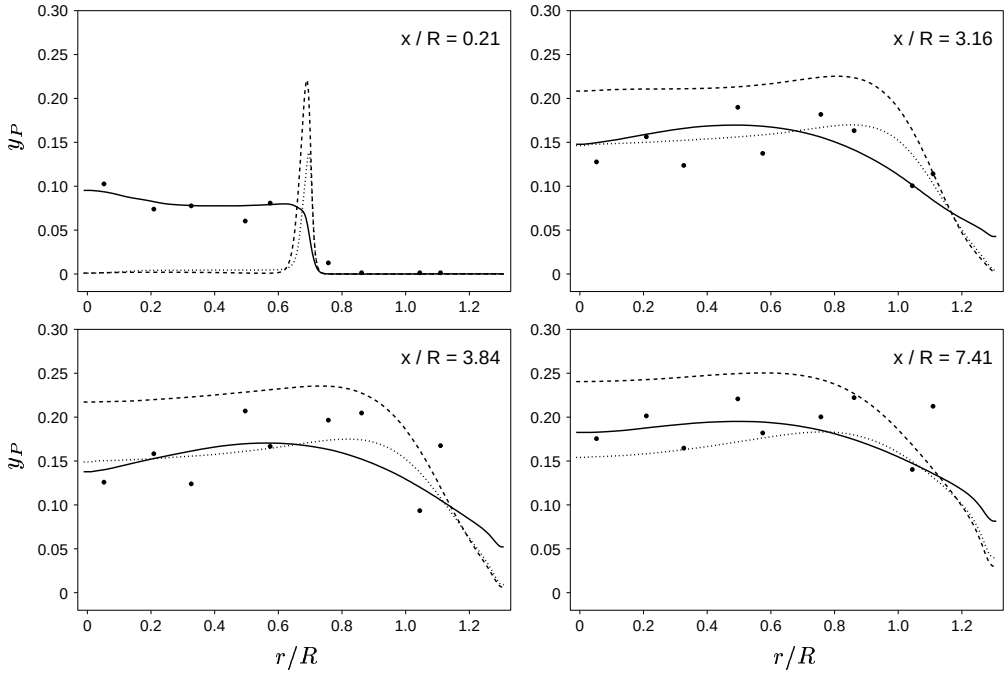

Fig. 5.6 Radial profiles of time-averaged product mass fraction. – – – : fast chemistry; ····· : steady flamelets; —— : progress variable approach; • : experiment.

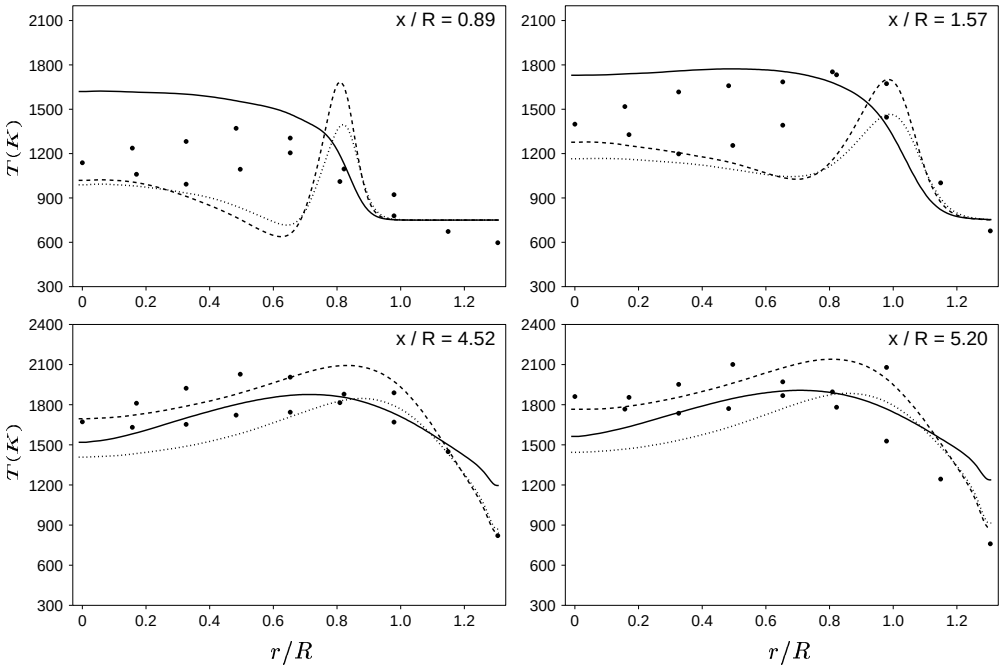

Fig. 5.7 Radial profiles of time-averaged temperature. – – – : fast chemistry; ····· : steady flamelets; —— : progress variable approach; • : experiment.

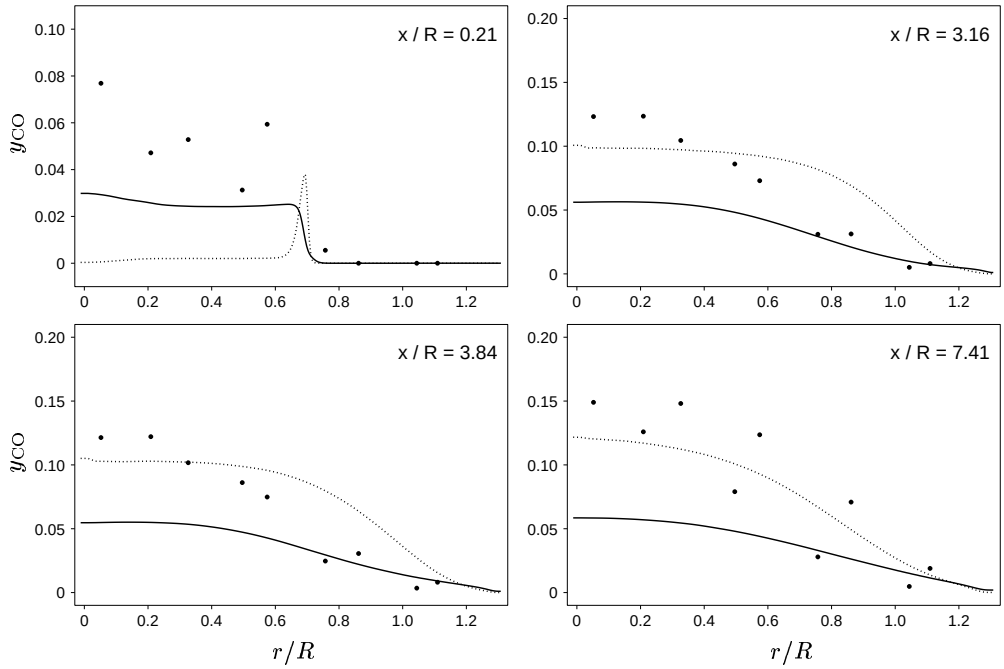

Fig. 5.9 Radial profiles of time-averaged CO mass fraction. ····· : steady flamelets; —— : progress variable approach; • : experiment.

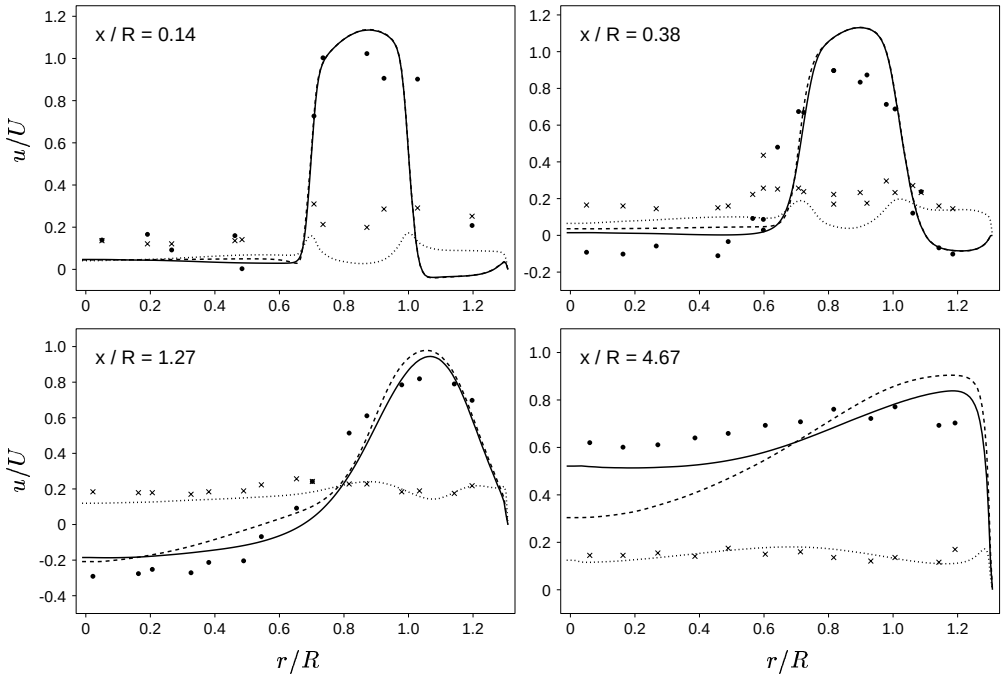

Fig. 5.8 Radial profiles of time-averaged axial velocity and axial fluctuation intensity. – – – : $\bar{u}$, both fast chemistry and steady flamelet models; —— : $\bar{u}$, progress variable approach; ····· : $\sqrt{\overline{u'^2}}$, progress variable approach; • : $\bar{u}$, experiment; × : $\sqrt{\overline{u'^2}}$, experiment.

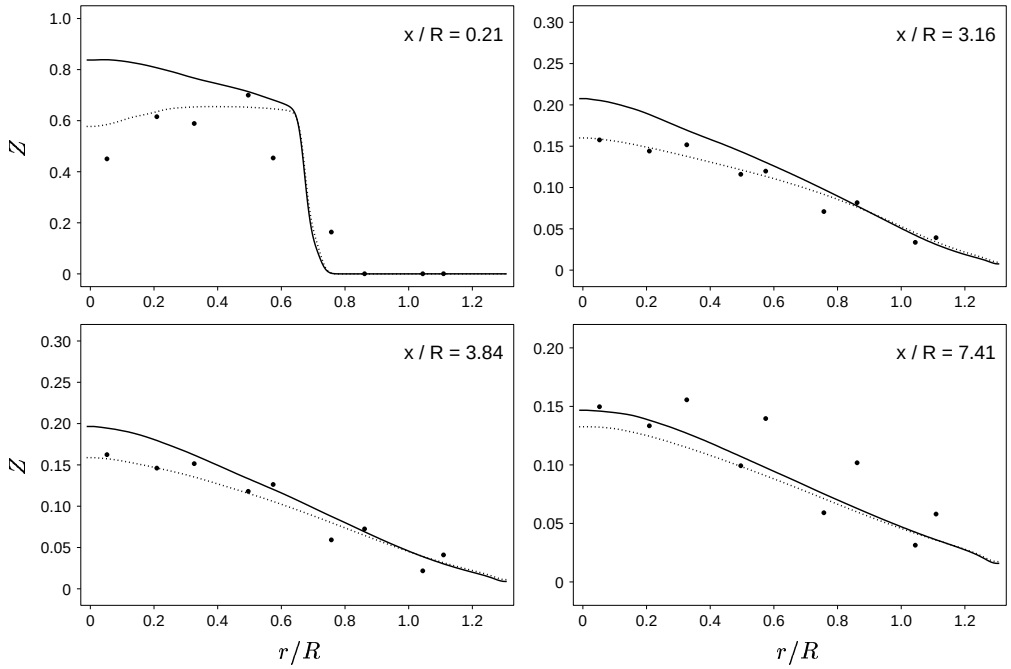

Fig. 5.11 Radial profiles of time-averaged mixture fraction. ——: progress variable approach with the unity Lewis numbers flamelet library; ------ : full multicomponent flamelet library; • : experiment.

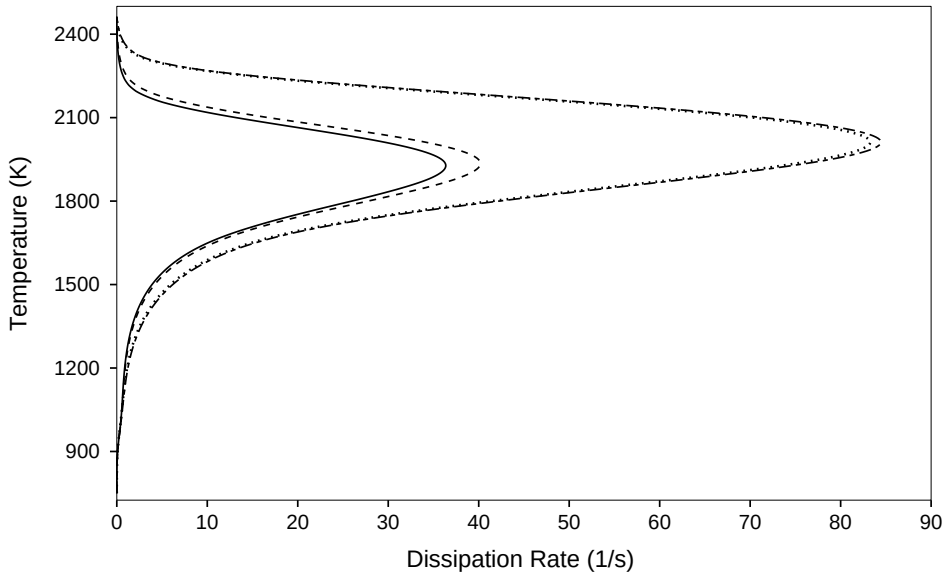

Fig. 5.10 Effect of mass diffusion model on the flamelet library. ——: full multicomponent (2.7); – – –: mixture diffusivities (2.10); ------ : unity Lewis numbers; —– – —: constant diffusivity.

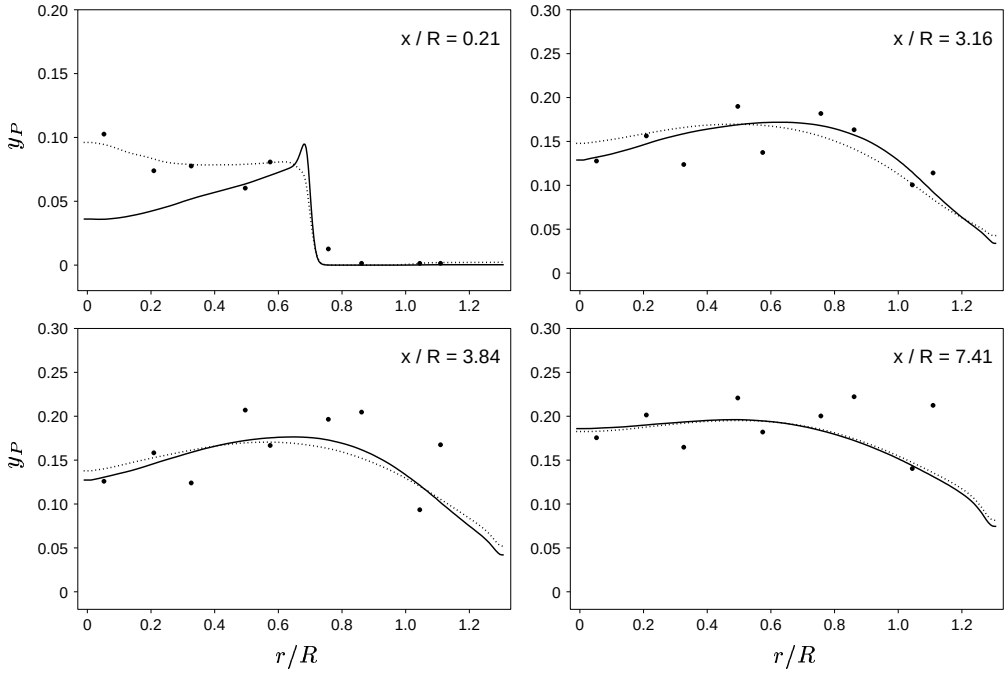

Fig. 5.12 Radial profiles of time-averaged product mass fraction. —— : progress variable approach with the unity Lewis numbers flamelet library; ------ : full multicomponent flamelet library; • : experiment.

Chapter 6

CONCLUSIONS AND FUTURE DIRECTIONS

6.1 Conclusions

Large eddy simulation was shown to be a promising technique for prediction of complex turbulent reacting flows. In the present work, a new algorithm was developed for large eddy simulation of variable density reacting flows in simple combustor configurations. Particular attention was given to both the primary conservation (mass, momentum, scalar) and secondary conservation (kinetic energy, scalar "energy") properties of the method. The algorithm uses the primitive variables, which are staggered in both space and time.

Motivated by the inability of existing chemistry models to predict lifted diffusion flames, such as those occurring in gas turbine combustors, a new two-scalar approach involving mixture fraction and a reaction progress variable was developed. This is combined with a steady flamelet model that incorporates detailed chemical kinetics and multicomponent mass diffusion.

The calculations were compared with detailed experimental data from the United Technologies Research Center. Excellent agreement was obtained between computations and the experiment in both the mean and fluctuating velocity profiles, mean mixture fraction profiles, and mean product concentration. This agreement is particularly significant because no adjustable parameters were available for tuning, owing to the use of the dynamic procedure in the parameterization of turbulence.

Three chemistry models were tested in the present study: fast chemistry, steady flamelet, and the progress-variable approach. The results show that the progress-variable approach significantly outperforms both the fast chemistry and steady

flamelet models with only a marginal increase in computational cost. The progress-variable approach appears to be an effective method for capturing basic realistic flame behavior such as flame lift-off. However, the present formulation cannot accurately predict details of the combustion process such as pollutant formation and thermal radiation, and thus, future improvements will be necessary.

The present study has also shown that the inclusion of differential diffusion effects is crucial, at least at the subgrid-scale level, for the prediction of the dynamics of the near-field, where chemical kinetics and transport of radicals, which have a broad range of diffusivities, are important.

6.2 Recommendations for Future Work

While the progress-variable approach presented in this study adds much capability to the steady flamelet model, it is by no means a complete combustion model, but rather a first step towards a more general approach. In its present form, the progress-variable approach cannot account for convective heat transfer to boundaries, effects of radiation, premixed flame fronts, slow chemical processes such as those involved in pollutant formation, and instabilities due to acoustic interactions.

The progress-variable approach can be extended to account for heat transfer to boundaries by solving an additional transport equation for the total enthalpy, along with the mixture fraction and progress variable. Total enthalpy would then become an additional parameter in the flamelet chemistry tables. In this way, the effects of the isothermal wall boundary conditions that were present in the experiment of Owen *et al.* could be accounted for. A first step to account for radiation and soot formation is to incorporate them directly into the calculation of the flamelet library. A radiative loss term could also be added to the enthalpy transport equation.

An improvement in the choice of progress variable should also be considered. The best candidate would be the entropy, because it is guaranteed to vary monotonically with reaction progress and it should provide a better parameterization of slowly evolving, near-equilibrium chemical states. However, entropy is governed by a significantly more complicated equation than product mass fraction and includes

source terms for both mixing and chemical reaction.

To better model the formation of pollutants, the addition of secondary progress variables, having significantly slower time scales than the primary progress variable, should be considered. This may require further development of the chemical tabulation procedures for the efficient calculation, storage, and retrieval of chemical states.

The assumed PDF for the progress variable used in the present study does not account for the effects of subgrid fluctuations is scalar dissipation rate or for reaction front propagation in premixed and partially premixed combustion. Future improvements to the this model should include both the effects of dissipation rate and the chemical source term on the assumed shape of the PDF.

The numerical scheme for variable-density flows presented here can be extended to include compressibility effects to account for low Mach number acoustics using a Helmholtz equation for pressure. The special feature of this extension is that acoustic waves relevant to combustion instabilities can be accounted for at a considerable savings in computer resources.

REFERENCES

Akselvoll, K. & Moin, P. (1995) "Large-eddy simulation of turbulent confined coannular jets and turbulent flow over a backward facing step" Mech. Eng. Dept. Report TF-63, Stanford University.

Akselvoll, K. & Moin, P. (1996) "Large-eddy simulation of turbulent confined coannular jets" *J. Fluid Mech.* **315**, 387–411.

Bird, R. B., Stewart, W. E., & Lightfoot, E. N (1960) *Transport Phenomena*, John Wiley and Sons, New York.

Bushe, W. K. & Steiner, H. (1999) "Conditional moment closure for large eddy simulation of nonpremixed turbulent reacting flows" *Phys. Fluids* **11**, 1896–1906.

Calhoon, W. H. & Menon, S. (1996) "Subgrid Modeling for Reacting Large Eddy Simulations" AIAA Paper 96-0516.

Carati, D. & Eijnden, E. V. (1997) "On the self-similarity assumption in dynamic models for large eddy simulations" *Phys. Fluids* **9**, 2165–2167.

Caruso, S. C. (1985) "Adaptive grid techniques for elliptic fluid-flow problems" Ph.D. Thesis, Mech. Eng. Dept., Stanford University.

Colucci, P. J., Jaberi, F. A., Givi, P. & Pope, S. B. (1998) "Filtered density function for large eddy simulation of turbulent reacting flows" *Phys. Fluids* **10**, 499–515.

Cook, A. W. (1997) "Determination of the constant coefficient in scale similarity models of turbulence" *Phys. Fluids* **9**, 1485–1487.

Cook, A. W. & Riley, J. J. (1994) "A subgrid model for equilibrium chemistry in turbulent flows" *Phys. Fluids* **6**, 2868–2870.

Cook, A. W., Riley, J. J. & Kosály, G. (1997) "A Laminar Flamelet Approach to Subgrid-Scale Chemistry in Turbulent Flows" *Combust. Flame* **109**, 332–341.

Cuenot, B., Egolfopoulos, F. N. & Poinsot, T. (2000) "An unsteady laminar flamelet model for non-premixed combustion" *Combust. Theory Modelling* **4**,

77–97.

DesJardin, P. E. & Frankel, S. H. (1998) "Large eddy simulation of a turbulent nonpremixed reacting jet: Application and assessment of subgrid-scale combustion models" *Phys. Fluids* **10**, 2298–2314.

Frankel, S. H., Adumitroaie, V., Madnia, C. K. & Givi, P. (1993) "Large eddy simulation of turbulent reacting flows by assumed PDF methods" in *Engineering Applications of Large Eddy Simulations*, S. A. Ragab & U. Piomelli (eds.), 81–101, ASME.

Gao, F. & O'Brien, E. E. (1993) "A large-eddy simulation scheme for turbulent reacting flows" *Phys. Fluids A* **5**, 1282–1284.

Germano, M., Piomelli, U., Moin, P. & Cabot, W. H. (1991) "A dynamic subgrid-scale eddy viscosity model" *Phys. Fluids A* **3**, 1760–1765.

Ghosal, S., Lund, T. S., Moin, P. & Akselvoll, K. (1995) "A dynamic localization model for large-eddy simulation of turbulent flows" *J. Fluid Mech.* **286**, 229–255.

Ghosal, S. & Moin, P. (1995) "The Basic Equations for the Large Eddy Simulation of Turbulent Flows in Complex Geometry" *J. Comput. Phys.* **118**, 24–37.

Girimaji, S. S. & Zhou Y. (1996) "Analysis and modeling of subgrid scalar mixing using numerical data" *Phys. Fluids* **8**, 1224–1236.

Harlow, F. H. & Welch, J. E. (1965) "Numerial Calculation of Time-Dependent Viscous Incompressible Flow of Fluid with Free Surface" *Phys. Fluids* **8**, 2182–2189.

Jaberi, F. A. & James, S. (1998) "A dynamic similarity model for large eddy simulation of turbulent combustion" *Phys. Fluids* **10**, 1775–1777.

Jaberi, F. A., Colucci, P. J., James, S., Givi, P. & Pope, S. B. (1999) "Filtered mass density function for large-eddy simulation of turbulent reacting flows" *J. Fluid Mech.* **401**, 85–121.

Jiménez, J., Liñán, A., Rogers, M. M. & Higuera, F. J. (1997) "*A priori* testing of subgrid models for chemically reacting non-premixed turbulent shear flows" *J. Fluid Mech.* **349**, 149–171.

Johnson, B. V. & Bennett, J. C. (1981) "Mass and Momentum Turbulent Transport Experiments with Confined Coaxial Jets" NASA CR-165574.

Johnson, B. V. and Bennett J. C. (1984) "Statistical Characteristics of Velocity, Concentration, Mass Transport, and Momentum Transport for Coaxial Jet Mixing in a Confined Duct" *J. of Eng. for Gas Turbines and Power* **106**, 121–127.

Kerstein, A. R. (1992a) "Linear-eddy modeling of turbulent transport. Part 4. Structure of diffusion flames" *Combust. Sci. Tech.* **81**, 75–96.

Kerstein, A. R. (1992b) "Linear-eddy modeling of turbulent transport. Part 7. Finite-rate chemistry and multi-stream mixing" *J. Fluid Mech.* **240**, 289–313.

Klimenko, A. Y. & Bilger, R. W. (1999) "Conditional moment closure for turbulent combustion" *Prog. Energy Combust. Sci.* **25**, 595.

Le, H. & Moin, P. (1994) "Direct numerical simulation of turbulent flow over a backward-facing step" Mech. Eng. Dept. Report TF-58, Stanford University.

Legier, J. P., Poinsot, T. & Veynante, D. (2000) "Dynamically thickened flame LES model for premixed and non-premixed turbulent combustion" *Proceedings of the 2000 CTR Summer Program*, 157–168, Center for Turbulence Research, NASA-Ames/Stanford University.

Leonard, B. P. (1979) "A stable and accurate convective modelling procedure based on quadratic upstream interpolation" *Comput. Meth. in Applied Mech. and Eng.* **19**, 59–98.

Lesieur, M. & Métais, O. (1996) "New trends in large-eddy simulations of turbulence" *Ann. Rev. Fluid Mech.* **28**, 45–82.

Lilly, D. K. (1992) "A proposed modification of the Germano subgrid-scale closure method" *Phys. Fluids A* **4**, 633–635.

McMurtry, P. A., Menon, S. & Kerstein, A. R. (1993) "Linear eddy modeling of turbulent combustion" *Energy Fuels* **7**, 817–826.

Mittal, R. & Moin, P. (1997) "Suitability of upwind-biased finite difference schemes for large-eddy simulation of turbulent flows" *AIAA J.* **35**, 1415–1417.

Moin, P., Squires, K., Cabot, W. & Lee, S. (1991) "A dynamic subgrid-scale

model for compressible turbulence and scalar transport" *Phys. Fluids A* **3**, 2746–2757.

Moin, P. (1997) "Progress in Large Eddy Simulation of Turbulent Flows" AIAA Paper 97-0749.

Moin, P. (2001) *Fundamentals of Engineering Numerical Analysis*, Cambridge University Press.

Morinishi, Y., Lund, T. S., Vasilyev, O. V. & Moin, P. (1998) "Fully Conservative Higher Order Finite Difference Schemes for Incompressible Flow" *J. Comput. Phys.* **143**, 90–124.

Mohseni, K. & Colonius, T. (2000) "Numerical treatment of polar coordinate singularities" *J. Comput. Phys.* **157**, 787–795.

Müller, C. M., Breitbach, H. & Peters, N. (1994) "Partially premixed turbulent flame propagation in jet flames" *Proc. Combust. Inst.* **25**, 1099–1106.

Nicoud, F. (2000) "Conservative high-order finite-difference schemes for low-Mach number flows" *J. Comput. Phys.* **158**, 71–97.

Owen, F. K., Spadaccini, L. J. & Bowman, C. T. (1976) "Pollutant formation and energy release in confined turbulent diffusion flames" *Proc. Combust. Inst.* **16**, 105–117.

Peters, N. (1983) "Local Quenching Due to Flame Stretch and Non-Premixed Turbulent Combustion" *Combust. Sci. Tech.* **30**, 1–17.

Peters, N. (1984) "Laminar diffusion flamelet models in non-premixed turbulent combustion" *Prog. Energy Combust. Sci.* **10**, 319–339.

Peters, N. (1986) "Laminar flamelet concepts in turbulent combustion" *Proc. Combust. Inst.* **21**, 1231–1250.

Peters, N. (2000) *Turbulent Combustion*, Cambridge University Press.

Piacsek, S. A. & Williams, G. P. (1970) "Conservation Properties of Convection Difference Schemes" *J. Comput. Phys.* **6**, 392–405.

Pierce, C. D. & Moin, P. (1998a) "Large Eddy Simulation of a Confined Coaxial Jet with Swirl and Heat Release" AIAA Paper 98-2892.

Pierce, C. D. & Moin, P. (1998b) "Method for Generating Equilibrium Swirling

Inflow Conditions" *AIAA J.* **36**, 1325–1327.

Pierce, C. D. & Moin, P. (1998c) "A dynamic model for subgrid-scale variance and dissipation rate of a conserved scalar" *Phys. Fluids* **10**, 3041–3044.

Pitsch, H. & Peters, N. (1998) "A Consistent Flamelet Formulation for Non-Premixed Combustion Considering Differential Diffusion Effects" *Combust. Flame* **114**, 26–40.

Pitsch, H. (2000) "Unsteady Flamelet Modeling of Differential Diffusion in Turbulent Jet Diffusion Flames" *Combust. Flame* **123**, 358–374.

Pitsch, H. & Steiner, H. (2000) "Large-eddy simulation of a turbulent piloted methane/air diffusion flame (Sandia flame D)" *Phys. Fluids* **12**, 2541–2554.

Pope, S. B. (1985) "PDF Methods for Turbulent Reactive Flows" *Prog. Energy Combust. Sci.* **11**, 119–192.

Pope, S. B. (1990) "Computations of turbulent combustion: Progress and challenges" *Proc. Combust. Inst.* **23**, 591–612.

Réveillon, J. & Vervisch, L. (1998) "Subgrid-Scale Turbulent Micromixing: Dynamic Approach" *AIAA J.* **36**, 336–341.

Reynolds, W. C. (1986) "The element potential method for chemical equilibrium analysis: implementation in the interactive program STANJAN" Mech. Eng. Dept. Report, Stanford University.

Roback, R. & Johnson, B. V. (1983) "Mass and Momentum Turbulent Transport Experiments with Confined Swirling Coaxial Jets" NASA CR-168252.

Sipperley, C. M., Huh, J. Y., Edwards, C. F. & Bowman, C. T. (1999) "Experimental validation studies for large-eddy simulation of a gas turbine main burner" *CTR Annual Research Briefs*, Center for Turbulence Research, NASA Ames/Stanford University.

Spadaccini, L. J., Owen, F. K. & Bowman, C. T. (1976) "Influence of Aerodynamic Phenomena on Pollutant Formation in Combustion (Phase I. Gaseous Fuels)" U.S. Environmental Protection Agency Report EPA-600/2-76-247a.

Steiner, H. & Bushe, W. K. (2001) "Large eddy simulation of a turbulent reacting jet with conditional source-term estimation" *Phys. Fluids* **13**, 754–769.

Vasilyev, O. V., Lund, T. S. & Moin, P. (1998) "A General Class of Commutative Filters for LES in Complex Geometries" *J. Comput. Phys.* **146**, 82–104.

Vervisch, L. & Trouvé, A. (1998) "LES modeling for lifted turbulent jet flames" *Proceedings of the 2000 CTR Summer Program*, 83–100, Center for Turbulence Research, NASA-Ames/Stanford University.

Wall, C., Boersma, B. J. & Moin, P. (2000) "An evaluation of the assumed beta probability density function subgrid-scale model for large eddy simulation of nonpremixed, turbulent combustion with heat release" *Phys. Fluids* **12**, 2522–2529.

Williams, F. A. (1985) *Combustion Theory, 2nd ed.*, Addison-Wesley.